University of Crete

Multiscale Study of the Structure of Molecular Clouds: Connecting Theory and Observations

Aris Evangelos Tritsis

Submitted in partial fulfillment
of the requirements for the
degree of Doctor of Philosophy

June 30, 2017

Multiscale Study of the Structure of Molecular Clouds: Connecting Theory with Observations

Aris Evangelos Tritsis
Department of Physics
University of Crete, 2017
Thesis supervised by Prof. Konstantinos Tassis

Abstract: This thesis is a multilateral and multiscale study of the structure of molecular clouds and the importance of magnetic fields in shaping them. First, we concentrate in the translucent parts of molecular clouds where elongated, quasi-periodic, magnetic-field aligned structures, termed "striations", have been recently discovered. We perform a series of numerical experiments and we find that striations are formed due to compressible fast magnetosonic waves. Using the properties of these magnetohydrodynamic waves revealed by the presence of striations in an isolated molecular cloud we reconstruct its 3D shape through a normal-mode analysis.

Turning our attention to the smallest, densest parts of molecular clouds we study the relation between the magnetic field and gas density in contracting prestellar cores. We find that previous studies severely underestimated the observational uncertainties in gas density. By properly accounting for these uncertainties and performing an independent analysis of the projected shapes of cores, we show that the data are in agreement with the predictions of the ambipolar diffusion theory of star formation. Driven by the need for accurate density estimates we have also performed numerical simulations of collapsing prestellar cores coupled with non-equilibrium chemical modelling and we have developed a method for probing the 3-dimensional shapes of cores using two-dimensional molecular column density maps. Finally, in order to directly compare our numerical models to observations we have developed a state-of-the-art, non local thermodynamic equilibrium (non-LTE) line radiative transfer code.

Μελέτη της Δομής των Διαστρικών Μοριακών Νεφών σε Διαφορετικές Χωρικές Κλίμακες: Σύγκριση Θεωρίας και Παρατηρήσεων

Άρης Ευάγγελος Τρίτσης
Τμήμα Φυσικής
Πανεπιστήμιο Κρήτης, 2017
Υπεύθυνος καθηγητής: Κωνσταντίνος Τάσσης

Περίληψη: Η παρούσα διατριβή είναι μία πολύπλευρη και σε πολλές διαφορετικές χωρικές κλίμακες, μελέτη των δομών των μοριακών νεφών και της σημασίας του μαγνητικού πεδίου στο σχηματισμό τους. Αρχικά μελετούμε τη δημιουργία νεοανακαλυφθέντων, νηματοειδών, ημιπεριοδικών δομών, ονόματι "striations", οι οποίες απατούνται στις περιοχές των μοριακών νεφών με χαμηλή πυκνότητα και είναι παράλληλες με το μαγνητικό πεδίο. Μέσω δισδιάστατων και τρισδιάστατων προσομοιώσεων μαγνητοϋδροδυναμικής, εξετάσαμε όλα τα πιθανά ενδεχόμενα για τη δημιουργία των "striations" και βρήκαμε ότι η μόνη δόκιμη εξήγηση για το σχηματισμό τους, προκύπτει μέσω της διέγερσης γρήγορων μαγνητοακουστικών κυμάτων. Στη συνέχεια, αξιοποιώντας το αποτελεσμά μας και δια μέσου της πρώτης στα χρονικά ανακάλυψης μας μιας περιοχής συντονισμού κυμάτων και των αρμονικών της συχνοτήτων σε ένα μοριακό σύννεφο, αναπαράγουμε την τρισδιάστατη δομή του.

Κατόπιν, στρέφουμε την προσοχή μας στην δυναμική εξέλιξη των πιο πυκνών σημείων των μοριακών νεφών και τη σχέση ανάμεσα στο μαγνητικό πεδίο και στην πυκνότητα του αερίου σε καταρρέοντες προαστρικούς πυρήνες. Βρίσκουμε ότι οι παρατηρησιακές αβεβαιότητες στην πυκνότητα του αερίου είχαν υποτίμηθεί σε προηγούμενες μελέτες. Λαμβάνουμε υπόψη τις αβεβαιότητες σε αυτές τις μετρήσεις και αναλύοντας ανεξάρτητα τις δισδιάστατες προβολές των προαστρικών πυρήνων, βρίσκουμε ότι τα τα δεδομένα συμφωνούν με τις προβλέψεις της θεωρίας της αμφιπολικής διάχυσης. Με αφορμή την ανάγκη για ακριβείς εκτιμήσεις της πυκνότητας, προσομοιώνουμε επίσης την κατάρρευσης προαστρικών πυρήνων σε συνδυασμό με μοντελοποίηση της χημείας που τους συνοδεύει και αναπτύσουμε μία μέθοδο ανέυρεσης των τρισδιάστατων σχημάτων τους, χρησιμοποιώντας χάρτες πυκνότητας στήλης συγκεκριμένων μορίων. Τέλος, για να μπορούμε να συγκρίνουμε άμεσα τα αριθμητικά μας μοντέλα με τις παρατηρήσεις, αναπτύσσουμε έναν σύγχρονο κώδικα μεταφοράς διάδοσης της ακτινοβολίας μοριακών και ατομικών γραμμών σε συνθήκες μη-τοπικής θερμοδυναμικής ισορροπίας.

Acknowledgments

First and foremost I wish to thank my advisor K. Tassis from whom I have learned a lot during my years as a PhD student. Most importantly he, and V. Pavlidou, have taught me how to fish when doing science, and for that I am forever in their debt. I am also grateful to N. D. Kylafis, A. Zezas, V. Charmandaris, I. Papadakis, T. Ch. Mouschovias, H. Yorke and P. F. Goldsmith. Interacting with all of them has been an invaluable experience. I also wish to thank G. P. Tsironis for letting me abuse the HPC facilities of QCN for so long. Without the Metropolis Cluster this work could not have been possible.

Most of this work was supported by FP7 through the Marie Curie Career Integration Grant PCIG-GA-2011-293531 "SFOnset" and from the EU FP7 Grant PIRSES-GA-2012-31578 "EuroCal". I also acknowledge funding from the European Research Council under the European Union's Seventh Framework Programme (FP/2007-2013)/ERC Grant Agreement n. 617001. This work was based (in part) on observations made with *Herschel*. *Herschel* is an ESA space observatory with science instruments provided by European-led Principal Investigator consortia and with important participation from NASA.

I also wish to thank the rest of the faculty members and all of my fellow graduate students for making my stay at University of Crete an unforgettable experience. Special thanks goes to G. V. Panopoulou, J. Liodakis, I. Psaradaki and I. Komis. Finally, I wish to express my gratitude to my parents Vasso & Dionysi. Without their love and support, I would not be where I am today.

Contents

Chapter 1

Introduction

Stars, the building blocks of the cosmos, and planets, the hosts of life, are born inside molecular clouds. How stars are formed is an important question not only for the interstellar medium community but also for galaxy evolution astrophysics and cosmology. However, due to the complicated nature of molecular clouds conclusive answers to this question remain elusive.

The temperature of molecular clouds is T $\sim$ 10 K (see Juvela et al. 2012 for a recent survey). They mainly consist of molecular hydrogen H_2 which however we cannot observed since electronic, vibrational and rotational excitations all require temperatures $\geq$ 100 K. Thus, in order to observe molecular clouds, we either rely on other molecules, such as CO, which have rotational transitions with lower excitation temperatures, or on thermal radiation from dust particles. The translucent parts of molecular clouds have number densities $n_{H_2} \sim 100\,\mathrm{cm}^{-3}$ and exhibit supersonic linewidths whereas dense prestellar cores have densities $n_{H_2} \sim 10^6 - 10^7\,\mathrm{cm}^{-3}$ and the gas appears to have subsonic velocities (Goodman et al. 1998).

The Herschel Space Observatory has provided dust emission maps of unprecedented detail of all nearby star forming regions. These maps have highlighted anew the fact that morphologically, molecular clouds consist of filamentary structures which often lie parallel to each other (Myers 2009; for a review see André et al. 2010). Usually, the term filament is reserved for dense ($n_{H_2} = 10^4 - 10^6\,\mathrm{cm}^{-3}$) elongated (aspect ratios = 1:3 - 1:10) structures although it is more loosely used throughout the literature. The common assumption about these structures is that they can be approximated by isothermal cylinders. Statistical studies have shown that prestellar cores lie within filaments (Men'shchikov et al. 2010; Konyves et al. 2015). Thus, filaments have attracted a lot of attention during the last decade.

Molecular clouds are highly non-linear systems with many physical processes (gravity, magnetic fields, thermal pressure, turbulence, interstellar radiation field) involved, none of which is negligible. During the early stages of star formation, the energy density associated with the related forces is approximately in equipartition (Draine 2011). Projection effects on the plane-of-the-sky complicate the picture. Overall, the complications that enter into the study of molecular clouds have led to a large number of questions being unanswered the most important of which are summarized bellow:

- why is the star formation efficiency so low?
- how do molecular clouds lose angular momentum?
- what is the origin of the initial mass function?

The low star formation efficiency: the total mass of molecular clouds in the Milky Way is estimated to be $\sim 10^9 M_\odot$ (McKee & Williams 1997, Bronfman et al. 2000). If gravity and thermal motions were the only relevant forces, stars would form in the free-fall time of molecular clouds and the star formation rate would be of the order 200 $M_\odot \mathrm{yr}^{-1}$. However, the most recent observational estimates place its value at only $\sim$1.3 $M_\odot \mathrm{yr}^{-1}$ (Murray & Rahman 2010). These values results in a star formation efficiency of the order of $\sim$ 1% (Mooney & Solomon 1988; Gao & Solomon 2004; Krumholz & Tan 2007). Thus, additional forces that oppose gravity and support the clouds from collapsing have to be present.

The angular momentum problem: it was also recognized early on (Spitzer 1968) that a mechanism that reduces the angular momentum of clouds by several orders of magnitude has to be in operation. From the theoretical perspective it can be shown that the centrifugal forces would shred a molecular cloud apart if the angular momentum was conserved from the initial galactic rotation (Mouschovias 1991). Observationally, the rotation of molecular clouds and that of dense cores within them is almost never measured to be greater than that of the background medium (Goldsmith & Arquilla 1985). Furthermore, the angular momentum is observed to be inversely proportional to the size of the cloud in the different phases of star formation. The angular momentum per mass of the Sun and that of protostellar disks is reduced by 7 and 5 order of magnitude respectively compared to the angular momentum of dense cores (Goodman et al. 1993; Chen et al. 2007; Pinto et al. 2011).

The initial mass function: observations have shown that the initial distribution of masses of young stars, known as the initial stellar mass function (IMF), can be approximated by a power law as $dN/dm \propto m^{\alpha}$ where N is the number of stars and m is the mass (for a review on different methods of the determination of the IMF see Krumholz 2014). The IMF has a peak at masses of $\sim 0.5 \cdot \mathrm{M}_{\odot}$ and the value of the exponent from the turnover up to the high-mass end is approximately constant and equal to $\alpha = 2.3$ (Salpeter 1955). What determines the slope of the IMF, why is there a peak and what is its relation with its progenitor, the distribution of masses of prestellar cores (i.e. the initial core mass function) are still hotly debated subjects.

Like in many other phenomena in astrophysics, progress in the field of star formation has been achieved following the reasoning bellow:

> "one observed certain phenomena, and one investigated what part of the phenomena could be explained; then the unexplained part was taken to show the effects of the magnetic field. It is clear in this case that, the larger one's ignorance, the stronger the magnetic field." (Woltjer 1967)

1.1 Magnetic fields in molecular clouds

Zeeman observations towards molecular clouds have shown that magnetic fields have values ranging from a few μG to mG (see Crutcher et al. 2010 for a summary of Zeeman measurements). Furthermore, ultraviolet radiation and cosmic rays penetrating the clouds ionize the translucent and dense gas with typical ionization fractions values of the order of 10^{-4} and 10^{-7} respectively (Caselli et al. 1998; Goicoechea et al. 2009). The neutral, bulk molecular gas then indirectly experiences the Lorentz force through collisions with the ions. Recent observational studies have also shown that the turbulent to order component of the magnetic field is less than unity (Planck Collaboration et al. 2016a; Panopoulou et al. 2016). These results indicate that the magnetic field is dynamical important compared to supersonic motions (i.e. turbulence).

Magnetic fields provide a solution to the problem of low star formation efficiency. Magnetic pressure and tension forces can provide support against the cloud's self-gravity. The fate of the cloud is then determined by the mass-to-magnetic flux ratio which quantifies the importance of magnetic fields compared to gravity (Mouschovias & Spitzer 1976). If the mass-to-flux ratio of a cloud is above a critical value (i.e. supercritical), gravity dominates, overcomes the support provided by the magnetic field and the cloud collapses. Vice versa, if the value of the mass-to-flux ratio is bellow this critical value (i.e. subcritical) the cloud is supported against its self-gravity.

However, there are two shortcomings with this simplified picture. The first problem is how are fragments and cores with supercritical mass-to-flux ratios formed when the parent cloud is subcritical. The second is that the magnetic flux of a prestellar core exceeds that of young stars by several order of magnitude (Babcock & Cowling 1953). For example, if magnetic field lines are frozen-in the gas (i.e. ideal MHD), a prestellar core with radius 0.1 parsecs threaded by a magnetic field of 5 μG should result in a young star with a magnetic field of the order of 10^8G. This value is 4 orders of magnitude greater than the largest magnetic field value ever detected in a star (Wade et al. 2012).

Both these problems are solved by the ambipolar-diffusion theory of star formation: low ionization fractions inside molecular clouds lead to infrequent collisions and imperfect coupling between the ions

and the neutrals, i.e. the two species are advected with different velocities. Neutral species "slip past" magnetic field lines and fall towards the centre of gravity faster than the magnetic flux which is advected with the velocity of the charged species (Ciolek & Mouschovias 1993; Tassis & Mouschovias 2007). This leads to redistribution of magnetic flux and an initially subcritical cloud can become supercritical while its envelope remains supported.

Molecular clouds are surrounded by atomic gas (Wannier et al.1983; van der Werf & Goss 1989; Andersson & Wannier 1993; Boulanger et al. 1998) with the two media being linked by magnetic field lines. Since the two media are connected, rotation of a molecular cloud will result in the external medium also being set into motion through the propagation of torsional Alfvén waves (Mouschovias & Paleologou 1979; Mouschovias & Paleologou 1980). This mechanism, referred to as "magnetic braking", has been shown analytically to efficiently transport angular momentum from the molecular to the HI cloud in short timescales of much less than 1 Myr. Numerical calculations by Basu & Mouschovias (1994) and Mellon & Li (2008) have also confirmed that magnetic braking reduces centrifugal forces early on in a cloud's life.

A number of observational evidence suggest that the initial stellar mass function and the core mass function share similarities both in the shape of the distribution and the value of the exponent at the high mass end (Motte et al. 1998; Testi & Sargent 1998; Johnstone et al. 2000; Alves et al. 2007; Nutter & Ward-Thompson 2007; Sadavoy et al. 2010). Thus, the IMF should be a natural consequence of any successful star formation theory. Mouschovias (1991) introduced three natural length scales in molecular clouds:

- the Alfvén length scale: the length scale bellow which ambipolar diffusion prevents Alfvén waves from being transmitted to the neutrals
- the critical thermal length scale: the length scale above which thermal-pressure forces are not transmitted fast enough to prevent gravitational collapse
- the critical magnetic length scale: the length scale above which gravitational forces dominate over magnetic forces and the cloud collapses (in absence of any other forces)

These length scales have as a result the formation of fragments with masses preferentially ≤ 3 $M_{\odot}$ but in the range 1 - 30 $M_{\odot}$. If the thermal length scale was the only relevant one in the selection of the mass spectrum then a very narrow IMF would emerge since the initial stages of star formation are isothermal. Kunz & Mouschovias (2009) included the effects of ambipolar diffusion and by assuming a flat distribution for the initial mass-to-flux ratio they showed that the resulting probability density function of the core mass function was in excellent quantitative agreement with observations. Bailey & Basu (2013) performed Monte Carlo simulations considering various cases (magnetic, non-magnetic, flux-freezing and non-ideal MHD models) and different distributions for the initial mass-to-flux and column density and also showed that the inclusion of the magnetic field broadens the core mass function.

1.2 Magnetic field orientations

Radio emission observations by Goldsmith et al. (2008) have revealed the presence of yet another type of filamentary structures in the low-column density parts of molecular clouds. These elongated, quasi-periodic structures, termed striations, are either seen to be associated with denser structures (Hennemann et al. 2012; Palmeirim et al. 2013; Alves de Oliveira et al. 2014; Cox et al. 2016) or as standalone features (Goldsmith et al. 2008; Miville-Deschenes et al. 2010). Observations of ^{12}CO and ^{13}CO of the J =1 - 0 and J = 2 - 1 transitions by Heyer et al. (2016) also seem to suggest velocity variations along the long axis of striations. Although striations are not cites of star formation, they encode invaluable information about the initial and boundary conditions of molecular clouds.

All-sky maps of polarized emission from Planck satellite have also revealed an interesting finding about the orientation of the magnetic field with respect to both filaments and striations (Planck Collaboration et al. 2016b). Magnetic field lines are consistently found to be parallel to the low-column density elongations whereas dense filaments lie perpendicularly to the magnetic field. This

findings are confirmed by additional studies with higher spatial resolution than that of Planck (Koch et al. 2015; Malinen et al. 2015; Panopoulou et al. 2016). At the same time, polarization observations from Planck have shown that magnetic fields are ordered (Planck Collaboration et al. 2016c). This further strengthens the case that they are dynamically important, since in the opposite case flows would drag along magnetic field lines which would then appear tangled (Ostriker et al. 2001).

The observational fact that magnetic fields lie perpendicularly to filaments is in contradiction with the view that filaments are formed due to compressions from shocks from super-Alfvénic turbulence (e.g. Padoan et al. 2001). Li et al. (2013) proposed a new scenario in which dense filaments form from the gravitational contraction along field lines while strong magnetic fields also act as the guiding channels of sub-Alfvénic flows which in turn result in striations. Based on the transport equations of MHD turbulence Soler and Hennebelle (2017) showed that $\phi = \pm 90$ and $\phi = 0$ where ϕ is the angle between density gradients and the magnetic field constituted attractors. Thus, the magnetic field evolves either perpendicularly or parallel to elongated structures.

1.3 Outline

In this work we extend the range of physical phenomena that can be explained by the magnetic field. In chapter 2 we concentrate on the formation mechanism of striations. We have performed 2D and 3D ideal magnetohydrodynamic (MHD) simulations testing all possible formation mechanisms. We have found that the only viable explanation for the appearance of striations is their formation by fast magnetosonic waves.

In the presence of boundaries fast magnetosonic waves can be trapped and set up normal modes. By identifying these normal modes the intrinsic dimensions of clouds, including their previously inaccessible by any means line-of-sight dimension, can be found. We report the first-ever discovery of these normal modes and find the intrinsic dimensions of Musca molecular cloud in chapter 3.

In chapter 4 we revisit the relation between the magnetic field strength and gas density in collapsing prestellar cores. We find that the data are consistent with the ambipolar diffusion theory of star formation and that previous studies severely underestimated the observational uncertainties in gas density.

In chapter 5 we develop a method for probing the intrinsic shape of prestellar cores based on a metric that quantifies whether molecular column density profiles are centrally peaked, depressed or flat, or by a simple comparison of 2D emission maps of specific molecules. Finally in chapter 6 we present a non-LTE line radiative transfer code which we plan to use in order to improve and extend our method for accessing the shapes of cores.

Chapter 2

The structure of the translucent parts of molecular clouds

In the work presented bellow, we have carried out numerical experiments testing possible mechanisms for the formation of striations. Simulation results from each model were then compared against observations of the striations region in Taurus molecular cloud (Goldsmith et al. 2008) based on four criteria: a) whether the model could reproduce the observed contrast between adjacent striations b) whether the model could account for the observed spatial power spectrum in velocity slices and velocity integrated emission c) whether the observed velocity range could be reproduced from the model and d) whether CO abundance followed the total density. In contrast to the commonly accepted premise in which striations are gas flows along field lines, we have singled out a model which involves the excitation of compressible fast magnetosonic waves as the only one able to reproduce the observed properties of striations.

Mon. Not. R. Astron. Soc. **000**, 000–000 (0000) Printed 1 August 2016 (MN LATEX style file v2.2)

Striations in molecular clouds: Streamers or MHD waves?

Aris Tritsis[1] and Konstantinos Tassis[1,2]
[1] *Department of Physics and ITCP *, University of Crete, PO Box 2208, 71003 Heraklion, Greece*
[2] *IESL, Foundation for Research and Technology-Hellas, PO Box 1527, 71110 Heraklion, Crete, Greece*

1 August 2016

ABSTRACT

Dust continuum and molecular observations of the low column density parts of molecular clouds have revealed the presence of elongated structures which appear to be well aligned with the magnetic field. These so-called striations are usually assumed to be streams that flow towards or away from denser regions. We perform ideal magnetohydrodynamic (MHD) simulations adopting four models that could account for the formation of such structures. In the first two models striations are created by velocity gradients between ambient, parallel streamlines along magnetic field lines. In the third model striations are formed as a result of a Kelvin-Helmholtz instability perpendicular to field lines. Finally, in the fourth model striations are formed from the nonlinear coupling of MHD waves due to density inhomogeneities. We assess the validity of each scenario by comparing the results from our simulations with previous observational studies and results obtained from the analysis of CO (J = 1 - 0) observations from the Taurus molecular cloud. We find that the first three models cannot reproduce the density contrast and the properties of the spatial power spectrum of a perpendicular cut to the long axes of striations. We conclude that the nonlinear coupling of MHD waves is the most probable formation mechanism of striations.

Key words: ISM: clouds – ISM: molecules – ISM: magnetic fields – methods: numerical –methods: observational

1 INTRODUCTION

Star formation occurs in condensations located within the dense elongated structures of molecular clouds. These structures, referred to as filaments, have been extensively studied both observationally and theoretically (see review of André et al. 2014). Although the role of the magnetic field in the evolution of filaments is still a topic of debate, its topology with respect to these filaments is well established. Polarimetric studies (Moneti et al. 1984; Pereyra & Magalhães 2004; Alves et al. 2008; Chapman et al. 2011; Sugitani et al. 2011; Palmeirim et al. 2013; Planck Collaboration et al. 2014) have revealed that the magnetic field is well ordered near dense filaments and perpendicular to their long axis.

Elongated structures, called striations, are also seen in the low column density parts of molecular clouds. Despite the fact that striations are not sites of star formation they are of high importance for interstellar medium (ISM) studies since they can reveal the dynamics of molecular clouds, and the early stages of star formation. However, there is yet no theoretically established physical mechanism explaining their formation. Understanding how striations form, whether they are long-lived or transient features and their role in star formation are important open questions.

Striations were first observed in ^{12}CO and ^{13}CO by Goldsmith et al. (2008) at the northwest part of the Taurus molecular cloud where they appear as autonomous structures. Striations were also observed by *Herschel* in dust emission. One of the most representative examples is the Polaris flare where well ordered, low density elongations are seen throughout the cloud (Miville-Deschênes et al. 2010). Like in Taurus, striations in the Polaris flare do not appear to be associated with the denser parts of the cloud. However, in certain clouds, striations are connected to denser filaments. Hennemann et al. (2012), Palmeirim et al. (2013) and Alves de Oliveira et al. (2014) analysed *Herschel* dust emission maps from DR21, Taurus and Chamaeleon molecular clouds respectively. In all of these studies, striations were interpreted as streamlines in which material flows into or out from more dense filaments and/or clumps.

Malinen et al. (2015) compared *Herschel* dust emission maps and Plank polarization data from the cloud L1642 in order to quantify the relative angle between the plane-of-the-sky component of the magnetic field and the long axes of striations. Using the Rolling Hough Transform (RHT) algo-

* Institute for Theoretical and Computational Physics, formerly Institute for Plasma Physics

rithm (Clark et al. 2014) they concluded that striations were in excellent alignment with the magnetic field. Panopoulou et al. (2016b) also used RHT to compare the orientation of the plane-of-the-sky (POS) magnetic field with linear structures in the Polaris flare and reported that the majority of striations were aligned with the projected magnetic field. The alignment between these structures and the magnetic field has also been pointed out in all clouds by all relevant studies in the literature (Goldsmith et al. 2008; Chapman et al. 2011; Hennemann et al. 2012; Palmeirim et al. 2013; Alves de Oliveira et al. 2014).

Li et al. (2013) considered the overall morphology of the magnetic field with respect to both filaments and striations. They concluded that besides the formation of dense filaments from the gravitational contraction along field lines, strong magnetic fields could also act as the guiding channels of sub-Alfvénic flows, thus forming striations. In this mass-accretion/flows-along-field-lines paradigm, which is currently the most common interpretation of such structures, density fluctuations are presumably caused by pressure differences which are in turn caused by fluctuations of the streaming speed as expected by Bernoulli's principle.

A shear velocity between ambient streamlines would normally lead to a Kelvin-Helmholtz instability. However, the presence of the magnetic field can stabilize the flow as long as the velocity difference between ambient streamlines is less than two times the Alfvén speed (Frank et al. 1996). In an early theoretical work, Frank et al. (1996) performed 2D simulations in ideal magnetohydrodynamics (MHD) assuming super-Alfvénic velocities with opposite signs on either side of a shear layer and an initially ordered magnetic field. They showed that although a Kelvin-Helmholtz instability occurred early on, a stable, laminar flow was quickly developed due to the presence of the magnetic field. The final density configuration in their simulations was parallel elongated structures aligned with the magnetic field.

Supersonic motions and other kinematic properties of molecular clouds have often been interpreted in terms of the presence of hydromagnetic waves (Arons & Max 1975; Zweibel & Josafatsson 1983). Specifically, the linewidth-size relation is attributed to Alfvén waves with long wavelengths and large amplitude (Mouschovias & Psaltis 1995). These findings suggest that striations may also be connected to MHD waves.

In the present paper we explore four possible physical mechanisms that could create striations. Since flows along magnetic field lines have been proposed by previous observational studies and are currently considered to be the most plausible mechanism for the formation of striations, we explore two models involving such flows. In the first model, we assume a sub-Alfvénic bulk flow and sub-Alfvénic velocity gradients between ambient streamlines. In the second scenario, we repeat the super-Alfvénic simulations performed by Frank et al. (1996) by adopting values for the parameters involved appropriate for molecular cloud conditions. In the third model, sub-Alfvénic flows perpendicular to the magnetic field cause a Kelvin-Helmholtz instability which in turn produces striations. Finally, we consider an entirely different scenario in which striations are formed from the excitation of compressional magnetosonic waves. In this model, fluctuations of magnetic pressure create striations. Magnetosonic waves are naturally excited from Alfvén waves due to density inhomogeneities. The values adopted in our models are driven from observational results from the literature and analysis of observational data presented here. We find that in the first three models the density contrast between the linear structures that are formed is so low that essentially flows along or perpendicular to magnetic field lines fail to create striations. In contrast, the model including coupling of MHD waves successfully reproduces most of the observational properties of striations.

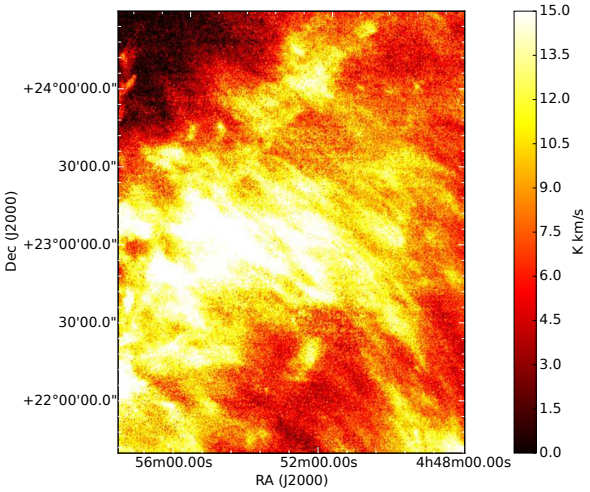

Figure 1. CO integrated intensity map of the striations observed in Taurus molecular cloud. The integration was performed only in the velocity range where the striations appear (4.76 $\sim$ 7.55 km/s).

In section § 2 we quantify the observed properties of striations to facilitate a quantitative comparison to simulations. Numerical simulations of models involving streamers and corresponding results are described in § 3.1, § 3.2 and § 3.3. In § 4 we provide some theoretical background for our fourth physical model (MHD waves) and describe our results. We summarize and discuss our conclusions in § 5.

2 OBSERVATIONS

In order to observationally quantify the properties of the striations we use ^{12}CO (J = 1 - 0) line emission data of the Taurus molecular cloud from the FCRAO survey (Goldsmith et al. 2008). The velocity resolution in the CO data cube is δv_{ch}= 0.266 km/s. FCRAO's telescope beam size at ^{12}CO (J = 1 - 0) emission frequency (115 GHz) is 45" which at the distance of the Taurus cloud (140 pc) yields a spatial resolution of 0.013 pc. An integrated intensity map of the region of interest is shown in Figure 1.

In the observational data we define a cartesian coordinate system where the x and y axes are respectively perpendicular and parallel to the largest dimension of the striations as projected on the plane of the sky. Thus, the z axis is parallel to the line-of-sight (LOS). In the left panel of Figure 2 we show an averaged perpendicular cut of the integrated intensity of the striations (solid black line) to which we have applied a low pass filter (smooth dashed red line). In order to increase the signal to noise ratio in our analysis we first

Table 1. Parameters used in each run.

Model	density (cm^{-3})	B_{y0} (μG)	δ (%)	Chemistry	z dimension (pc)	resolution
sub-Alfvénic streamers	200	15	10	✗	✗	128×128
	200	15	100	✗	✗	128×128
	200	15	100	✗	✗	256×256
super-Alfvénic streamers	200	15	✗	✗	✗	128×128
	200	15	✗	✗	0.5	128×128×64
	200	15	✗	✗	✗	256×256
sub-Alfvénic flows $\perp$ to $\vec{B}$	200	15	✗	✗	0.5	128×128×64††
MHD waves coupling	200	15	15	✓	✗	256×256
	100	15	15	✗	✗	256×256
	400	15	15	✗	✗	256×256
	200	30	15	✗	✗	256×256
	200	7.5	15	✗	✗	256×256
	200	15	30/15	✗	✗	256×256†
	200	15	30/15	✗	✗	256×256‡
	100	30	15	✗	0.125	256×256×64
	100	30	15	✗	0.25	256×256×64
	200	15	15	✗	✗	512×512

† The perturbation amplitude (δ) is 30% for the magnetic field and 15% for the density and thermal pressure.
‡ Same as in † but with a spectrum of Alfvén waves initially present in the system.
†† The value for the magnetic field strength refers to its z component. In this model, $B_{y0} = B_{x0} = 0$.

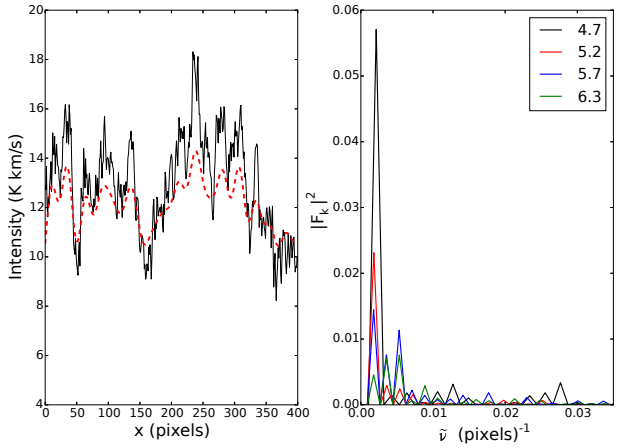

Figure 2. Left panel: A cut perpendicular to the long axis of the striations (black line) and a low pass noise filter (smooth dashed red line). Right panel: The power spectrum in 4 velocity channels (given in km/s in the legend). All velocity channels exhibit the same dominant frequency with other wavelengths also present, thus suggesting a creation mechanism involving superposition of waves.

consider three adjacent cuts along the x direction and then average the intensity of their corresponding y pixel values. In the right panel of Figure 2 we show the spatial power spectra in 4 velocity channels. In the power spectrum there is unambiguously a dominant frequency with other wavelengths also present. To compute the power spectrum in each velocity slice we have again averaged pixel values from three adjacent cuts. The full velocity range where striations are visible is $\sim$ 2.5-3.0 km/s. Observations also suggest multiple velocity components along the LOS (Heyer & Brunt 2012). From Figure 2 it is clear that both the integrated intensity cut and intensity cuts in velocity slices are quasi-periodic.

Due to the quasi-periodicity of the integrated intensity cut there is no unique contrast between maxima and minima. We thus need a method to robustly and systematically compute the contrast. To do so, we first consider all perpendicular cuts to the long axis of the striations and identify where each intensity cut has extrema. We compute the contrast between successive extrema and take the mean of all contrast values. To avoid confusion caused by point to point variations, extrema were identified from the low pass filter rather than the actual cut. However, the contrast was properly computed from the values of the actual intensity cut. The mean contrast, adopting a low pass filter such as the one shown in the left panel of Figure 2 (red dashed line) which reasonably follows the intensity profile, is $\sim$ 25%. For direct comparison with observations we will use the same method of computing the contrast throughout this paper.

3 STREAMERS

We performed 2D and 3D numerical simulations in cartesian coordinates using the astrophysical code FLASH 4.0.1 (Fryxell et al. 2000; Dubey et al. 2008). We used the unsplit staggered mesh algorithm (Lee 2013) to solve the equations of ideal MHD without gravity. For the Riemann problem we used Roe's solver which accounts for all waves that can arise in the MHD equations. We used van Leer's flux limiter and third order interpolation to reduce numerical diffusion as much as possible.

In the simulations we adopted magnetic field and den-

sity values driven from observational estimates from the same region in Taurus. Chapman et al. (2011) used polarization data to map the POS component of the magnetic field at the northwest part of Taurus molecular cloud where striations were first observed. Using the Chandrasekhar & Fermi (1953) method they found a value of $B_{pos} = 17 \pm 1$ μG whereas using Hildebrand's et al. (2009) method they found $B_{pos} = 31 \pm 4$ μG. Despite the fact that the intrinsic magnetic field value would be even higher than these observational limits, we adopted a conservative reference value of 15 μG. Chapman et al. (2011) also used CO data from the FCRAO survey (Goldsmith et al. 2008) to constrain the number density. They reported a value of $\rho = 200 \pm 10$ cm^{-3}. This was the value used for the background number density in our reference runs. A constant temperature of 15 K was adopted for all of our models. Thus, the sound speed is $\sim$ 0.35 km/s, the Alfvén speed ($v_a = B/\sqrt{4\pi\rho}$) is $\sim$ 1.58 km/s and the plasma β parameter ($\beta = 8\pi P_{th}/B^2$ where P_{th} is the thermal pressure) is $\sim$ 0.1.

In our simulations, we define a cartesian coordinate system such that the direction of the magnetic field is along the y axis and the z axis represents the LOS dimension. The physical dimensions of the computational area in our 2D simulations are 1 pc in each direction. Driven from recent observational results (Qian et al. 2015), in 3D simulations, the LOS dimension is taken to be smaller than the other two. We terminate each simulation after 5 Myrs. A list of all runs is given in Table 1.

3.1 sub-Alfvénic flow along field lines

In this model we test the premise that sub-Alfvénic velocity differences between ambient streamlines can form striations. In principle, velocity differences cause a pressure gradient in the perpendicular to the magnetic field direction which is in turn expected to create compressions and rarefactions in density. These shear flows are stabilized against Kelvin-Helmholtz instabilities due to the presence of the magnetic field. The stability condition for the Kelvin-Helmholtz instability assuming an inviscid, incompressible magnetized plasma is:

$$\frac{1}{4\pi}[(\vec{k}\cdot\vec{B_1})^2 + (\vec{k}\cdot\vec{B_2})^2] > \frac{\rho_1\rho_2}{\rho_1+\rho_2}[\vec{k}\cdot(\vec{v_1}-\vec{v_2})]^2 \quad (1)$$

(Chandrasekhar 1961) where $\vec{k}$ is the wavenumber, $\vec{B_i}$ is the magnetic field value and $\vec{v_i}$ (i=1, 2) is the velocity on either side of the shear layer. In this sub-Alfvénic flow along field lines model, the stability condition of Equation 1 is satisfied at all times.

Initially, we assume a sub-Alfvénic, constant flow along the direction of the magnetic field. We then introduce perturbations in the velocity field along the x direction. Thus, at the beginning of the simulation, the only non-zero component of the velocity is along the y axis and is given by:

$$v_y(x) = v_{y0} + \delta v_y(x) \quad (2)$$

where $\delta v_y(x)$ is random and positive. We run simulations with two different amplitudes for the velocity perturbation, 10% and 100% of the unperturbed velocity. The unperturbed value of the y velocity component is 0.65 km/s. Thus the bulk velocity of the flow is sub-Alfvénic, yet supersonic. The magnetic field, density and thermal pressure are left unperturbed.

The boundary conditions are periodic in the y axis (i.e. along field lines) and reflective in the x direction. Simulations for this model were performed on a uniform grid with 128×128 grid points. Therefore, our spatial resolution is $\sim 7.8 \times 10^{-3}$ pc. An additional simulation was performed on a 256 × 256 grid to ensure convergence (see Table 1).

In Figure 3 we show density maps for the simulations with 10% (upper row) and 100% (lower row) perturbation amplitudes in the y velocity component. Different columns represent different times. From left to right the time is 0 Myrs (i.e. the initial condition), $\sim$ 1Myr and $\sim$ 5 Myrs. The mean contrast in density between adjacent striations is extremely low. In fact the mean contrast in density for the simulation in which the velocity difference between ambient streamlines can be up to 100% is just $\sim 4 \times 10^{-4}$%. The situation could not have been improved in a column density map if we had performed a 3D simulation. Projection effects from the 3D geometry would not increase the contrast since, due to the small size of the striation region in Taurus we can make the reasonable assumption that the LOS dimension has a constant thickness. As a result, the contrast in column density would roughly be the same as the contrast in density.

In Figure 4 we show perpendicular cuts to the long axis of these streamlines (left column) and the spatial power spectrum (right column). We plot the results for the simulation with 10% perturbation in the upper row and results for the simulation with 100% perturbation in the lower row. The two power spectra have peaks in the same spatial frequencies. Neither the profiles nor the power spectra resemble observations, but instead they are consistent with white noise. The features seen in all panels of Figure 4 originate from the random number generator with which we set up the velocity perturbations.

Despite the fact that the x boundary conditions for this model are reflective no waves are excited. Instead, magnetic field lines are "pushed" until the condition $\Pi_1 = \Pi_2$ is satisfied in every interface between adjacent streamlines. Here, $\Pi = P + \frac{B^2}{8\pi}$ is the total pressure. Furthermore, since the region is magnetically dominated, thermal pressure is not sufficient to cause large gradients in magnetic pressure in the x direction. As a result, $B_1 \approx B_2$, which for an isothermal gas leads to $\rho_1 \approx \rho_2$.

3.2 super-Alfvénic flow along field lines

For the initial conditions in this model we partly follow Frank et al. (1996). The magnetic field is again directed along the y axis and the y component of the velocity is given by:

$$v_y = -v_0 tanh(\frac{x - L_x/2}{a}) \quad (3)$$

where v_0 equals 1.2 times the Alfvén speed, L_x is the size of the computational area in the x direction and a is a parameter that quantifies the width of the shear layer. The value of a is set at 4% of the size of the x dimension. We further introduce a small velocity perturbation on the x component of the velocity with amplitude 10^{-3} the Alfvén speed. We do not perturb the magnetic field, thermal pressure or density.

The boundary conditions are periodic in the y direction

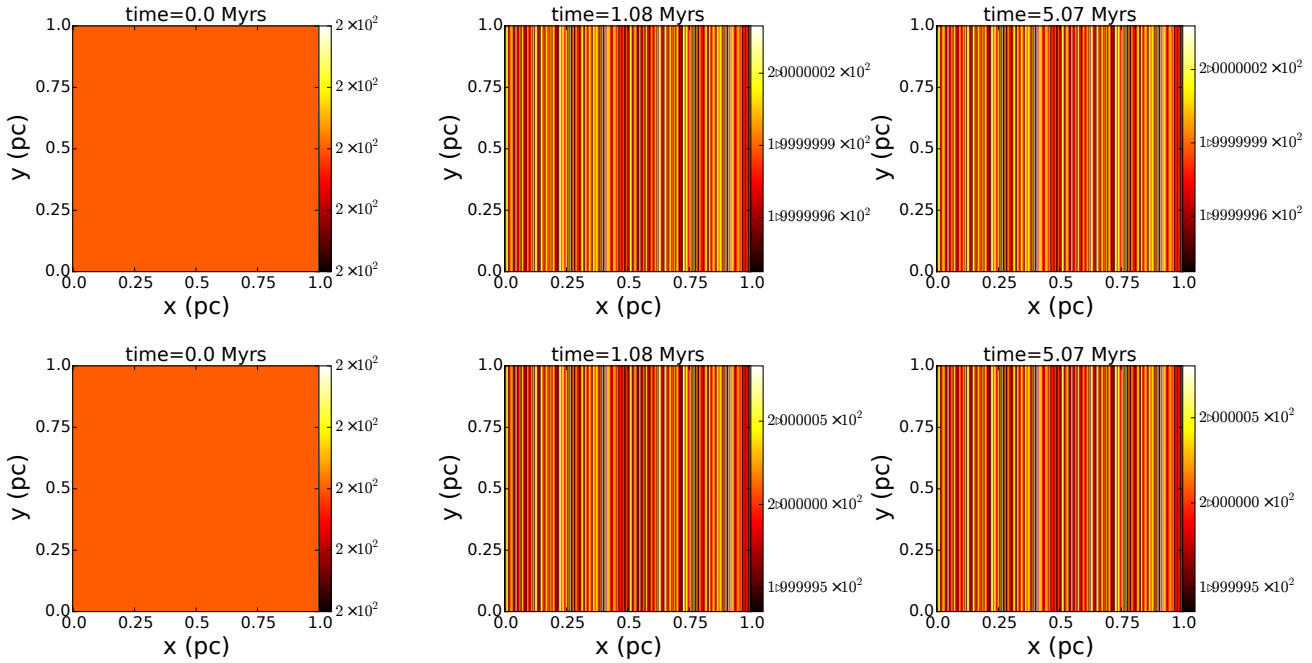

Figure 3. Slice density maps from our 2D simulations for the sub-Alfvénic flow along field lines model. In the upper row we plot our results from the simulation where the amplitude of the perturbation is 10% and in the lower row results where the amplitude of the perturbation is 100%. From left to right column the time is 0 Myrs (i.e. the initial condition), $\sim$ 1 Myr and $\sim$ 5 Myrs. The contrast between adjacent striations is extremely low for both perturbation amplitudes.

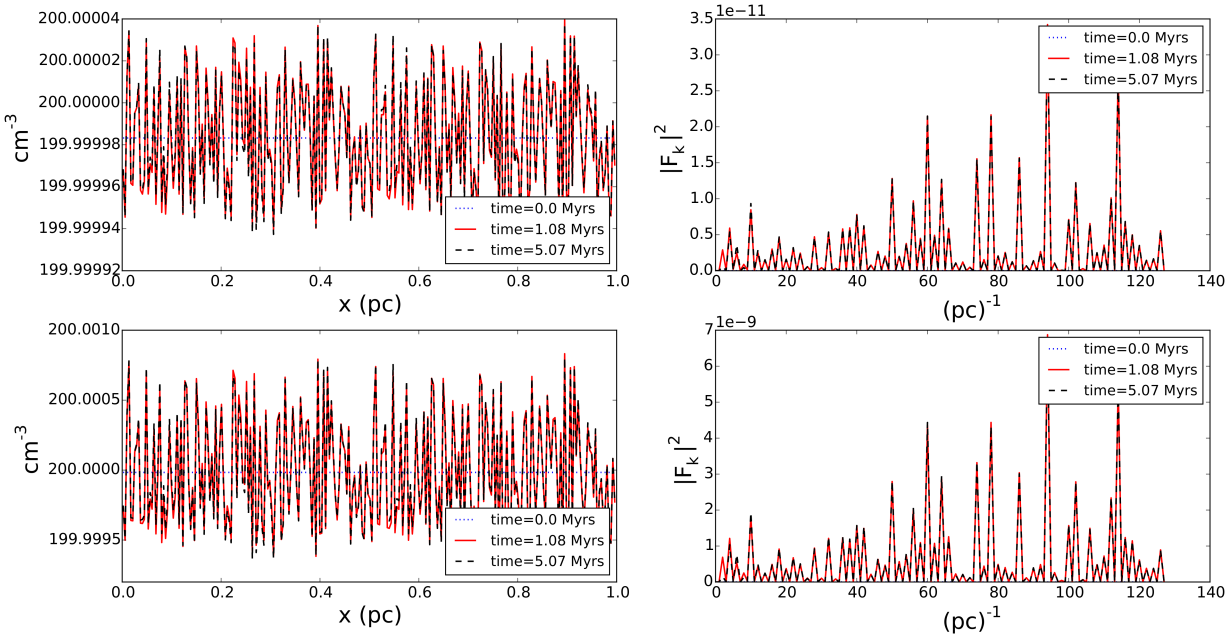

Figure 4. Left column: perpendicular density cuts to the striations for 0 Myrs (blue dotted line), $\sim$ 1 Myr (solid red line) and $\sim$ 5 Myr (dashed black line) for the sub-Alfvénic flow along setup and for the two perturbation amplitudes (upper panel: 10%, lower panel: 100%). Right column: The corresponding spatial power spectra.

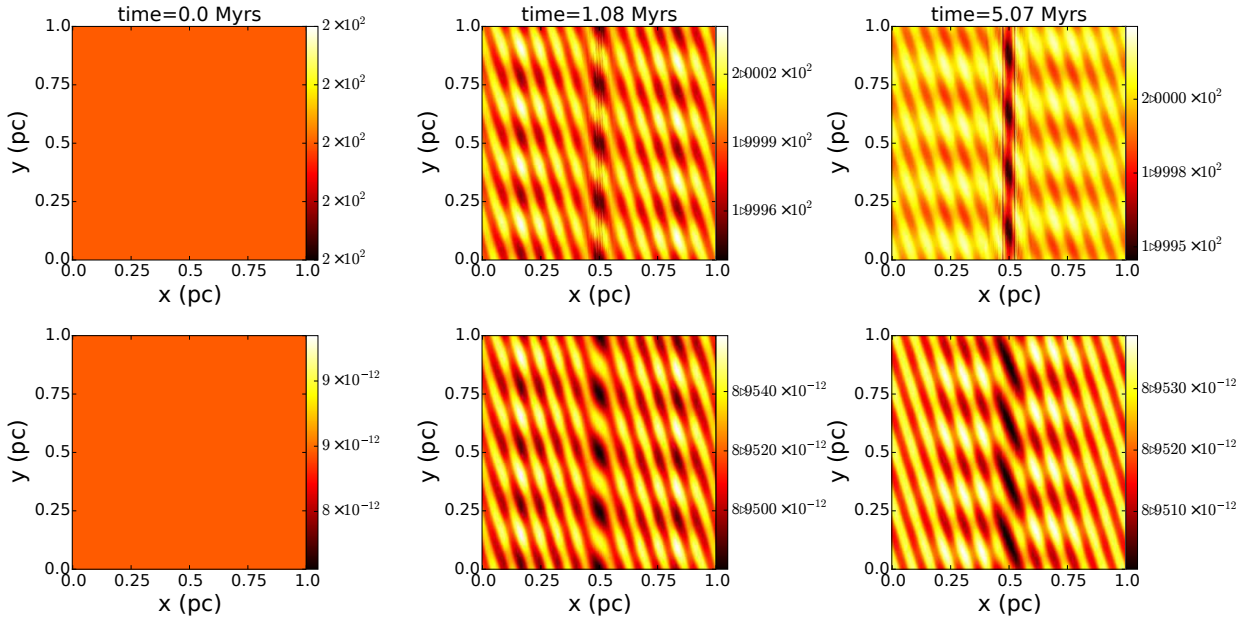

Figure 5. Upper row: density maps for 0 Myrs (left), ~ 1 Myr (middle) and ~ 5 Myr (right) from the simulations with the super-Alfvénic flow along setup. Lower row: magnetic pressure maps for the same time steps.

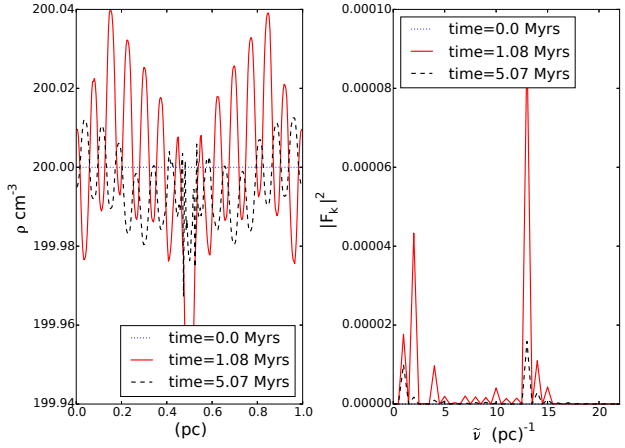

Figure 6. Left panel: perpendicular density cuts to the striations for 0 Myrs (blue dotted line), ~ 1 Myr (solid red line) and ~ 5 Myr (dashed black line) for the super-Alfvénic streamers. Right panel: the power spectrum in the same three time steps.

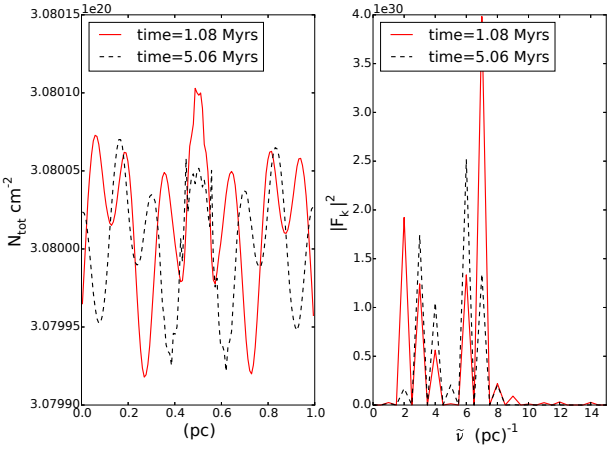

Figure 7. Left panel: perpendicular column density cuts to the striations for ~ 1 Myrs (solid red line) ~ 5 Myrs (dashed black line) as projected along the z axis from our 3D simulation adopting the super-Alfvénic flow along field lines model. Right panel: The corresponding spatial power spectrum for the same two timesteps.

(i.e. along magnetic field lines) and outflow in the x direction. The 2D simulation for this model was performed on a 128×128 uniform grid and an additional simulation with twice that resolution was performed in order to check for convergence.

In Figure 5 we show density maps (upper row) and magnetic pressure maps (lower row) for the same timesteps as in the previous model. As in the simulations by Frank et al.(1996) the flow is ordered due to the magnetic field despite the fact that the Kelvin-Helmholtz stability condition (Equation 1) is not satisfied. Intriguingly, the final configuration is parallel elongated structures which resemble observations. What is more, magnetic pressure fluctuations follow overdensities and rarefactions very well while magnetic field lines have been pivoted with respect to the initial configuration. Consequently, it seems that qualitatively this model may resemble observations. However, as in the case of the sub-Alfvénic streamers, the mean density contrast is very low, just $\sim 7.5 \times 10^{-3}\%$.

In Figure 6 we show perpendicular cuts for each of the timesteps of Figure 5 and the corresponding spatial power spectra. In contrast to sub-Alfvénic streamers, clear structures are created when the flow is super-Alfvénic. However, neither the perpndicular cut nor the power spectrum can re-

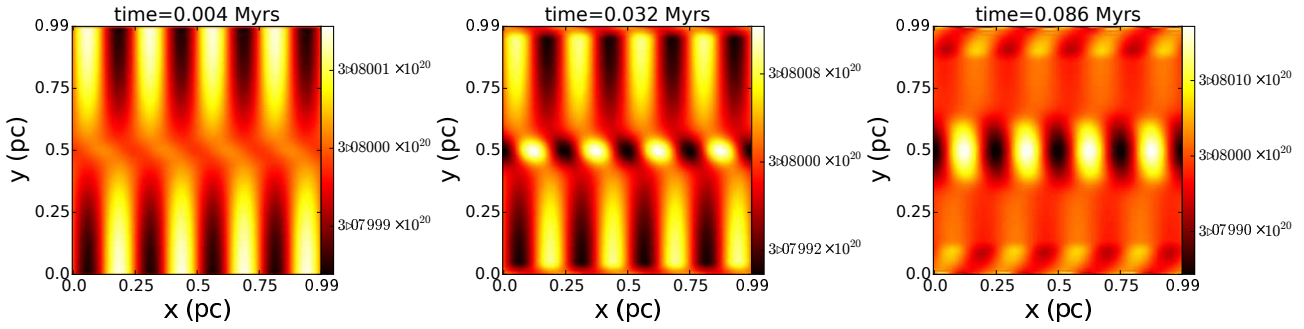

Figure 8. Column density maps from our 3D simulations for the sub-Alfvénic flows perpendicular to the field lines model. From left to right the time is 0.004 Myrs (i.e. the initial condition), ~ 0.03 Myr and ~ 0.09 Myrs. As in the two previous models the contrast between adjacent striations is extremely low.

produce observations. Here, power is distributed differently than observations in the sense that larger spatial frequencies have more power than the small ones. This is because the power is concentrated in the smallest ellipsoidal features seen in the density maps.

Even though the density contrast and power spectrum cannot reproduce observations, no reliable conclusions can yet be drawn from the 2D simulations alone since in three dimensions the magnetic field could affect the flow in a different manner. The possibility also exists that in 3D the magnetic field can no longer stabilize the flow, which would lead to turbulence. We thus run an additional 3D simulation where the shear layer is a sheet-like structure that extends along the LOS. The y component of the velocity is still given by Equation 3, but now, we also perturb v_0 along the z direction, i.e. $v_0(z) = v_0 + \delta v(z)$. In 3D, in the z direction, we choose outflow boundary conditions, the physical length is 1/2 shorter than that of x and y and the resolution of the grid is 128×128×64.

In Figure 7 we show the results from our 3D simulation for ~ 1 Myr and ~ 5 Myrs. In the left panel we plot the profiles across projections along the z axis, and in the right panel the corresponding power spectra. Introducing a velocity profile along the z-axis does not lead to turbulence but instead, the magnetic field can still stabilize the flow. However, as can be seen from the left panel of Figure 7 the contrast is still very low, even in a column density map. The low contrast remains regardless of the projection angle. In fact, when we consider a projection along the z-axis which for the intended purposes of these simulations represents the LOS, the mean contrast is $\sim 7.8 \times 10^{-3}\%$, just barely larger than the mean contrast in density maps.

Column density maps from our 3D simulations resemble the density maps from our 2D simulations shown in Figure 5 quite well. However, there are differences amongst the power spectra in 2D and 3D. These differences originate from two distinct effects. First, since in our 3D simulations the term v_0 in Equation 3 is a function of the LOS, different structures are formed in different density slices along the z direction. Although, in average, these density slices are similar to the ones shown in Figure 5 there are deviations which will appear in the power spectrum. The second reason is due to the integration along the LOS. In a column density map the bulges seen in the upper panel of Figure 5 are enhanced whereas other features are even fainter. Finally, in 3D, magnetic field lines are pivoted to a larger angle with respect to the initial configuration. In our 2D simulations the angle between the magnetic field at later times and the initial magnetic field is $\sim 18^\circ$ whereas the same angle in our 3D simulations is $\sim 40^\circ$.

From the stability condition of Equation 1 when the density and magnetic field values are equal on either side of an interface, a Kelvin-Helmholtz instability occurs only if the velocity difference between the two layers is twice the Alfvén speed. However, no such extreme velocity gradients have ever been observed in molecular clouds. Heyer & Brunt (2012) did a careful analysis of the velocity field in Taurus using the same observational data used here and concluded that in the striations region the motions of the flow were trans-Alfvénic. As a result, such a mechanism of producing striations in the diffuse ISM, requiring so large velocity gradients, would be unphysical even if it could reproduce observations.

3.3 sub-Alfvénic flow perpendicular to field lines

Periodically spaced, elongated structures, referred to as Ripples, have also been observed in the south-west part of Orion molecular cloud (Berné et al. 2010). Berné et al. 2010 attributed the formation of Ripples to a Kelvin-Helmholtz instability. Berné & Matsumoto (2012) and Hendrix et al. (2015) performed 2D and 3D MHD simulations respectively with flows perpendicular to the magnetic field and with the shear layer parallel to the field lines. They found that with this configuration periodically spaced, elongated structures were created. Although the physical conditions in these Ripples are very different from the physical conditions in regions where striations are observed, it is possible that the same formation mechanism is in operation. The possibility that Ripples and striations are created through the same physical process has been recently pointed out by Heyer et al. (2016).

In order to test for this scenario, we performed a 3D simulation adopting the same values for the density and magnetic field strength as in the previous two models. The direction of the magnetic field was taken to be along the LOS

(i.e. along the z axis) and the x component of the velocity was given by:

$$v_x = -v_0 tanh(\frac{y - L_y/2}{a}) \quad (4)$$

where similarly to Equation 3 the width of the shear layer is taken to be 4% the size of the y dimension. In equivalence with our 3D super-Alfvénic simulations v_0 was also perturbed along the z axis. With this configuration, the shear layer extends along the LOS and is thus parallel to the magnetic field.

Super-Alfvénic flows perpendicular to field lines would lead to distortions of the magnetic field. However, the magnetic field in the regions where striations appear is well ordered. Thus, such flows must be sub-Alfvénic and the value of v_0 in Equation 4 was taken to equal 0.45 times the Alfvén speed. Small amplitude perturbations were further introduced in the y velocity component. Apart from the velocity field, all other quantities were left unperturbed. Boundaries were periodic in all directions, the length of the LOS was half that of the other two directions and the resolution of the grid was 128×128×64.

In Figure 8 we plot column density maps for 3 timesteps, early in the simulation before turbulence is developed. Similarly to the two previous models involving flows, the contrast between adjacent striations is extremely small. Applying the same method as in observations in the column density map shown in the right panel of Figure 8 results in a mean contrast of just 0.004%.

In this model, the direction of the magnetic field is perpendicular to the planes shown in Figure 8. As a result, this viewing angle would not result in elongated structures parallel to the magnetic field since the observed polarization intensity would be zero. Moreover, if the magnetic field is at an angle with respect to the z axis the growth of the instability would decrease or even halted for large angles. Thus, there is a limited range of viewing angles for which the depolarization factor due to projection effects is small and these structures appear as elongations. Furthermore, elongations formed via this mechanism are only transient features lasting just a few 10^4 years. At later times, turbulence develops and these structures are no longer recognizable. Consequently there are at least two additional shortcomings in terms of matching the observations.

4 MHD WAVES

The equations of ideal MHD can be linearised by considering small amplitude perturbations. If we then assume that the perturbed quantities vary as $e^{i(\vec{k}\cdot\vec{r}-\omega t)}$ and substitute the expressions that arise for the perturbed quantities in the linearised equation of motion we get:

$$[\omega^2 - \frac{(\vec{k}\cdot\vec{B_0})^2}{4\pi\rho_0}]\vec{v} = \quad (5)$$
$$\{[c_s^2 + \frac{B_0^2}{4\pi\rho_0}]\vec{k} - \frac{(\vec{k}\cdot\vec{B_0})}{4\pi\rho_0}\vec{B_0}\}(\vec{k}\cdot\vec{v}) - \frac{(\vec{k}\cdot\vec{B_0})(\vec{v}\cdot\vec{B_0})}{4\pi\rho_0}\vec{k}$$

where $\vec{k}$ is the wavenumber, $\vec{B_0}$ is the unperturbed magnetic field, ρ_0 is the unperturbed density, ω is the angular frequency and $\vec{v}$ is the perturbed velocity. When the direction of propagation of the waves is parallel to the magnetic field (i.e. $\vec{k} \parallel \vec{B}$), Equation 5 leads to the dispersion relation of Alfvén waves. In the situation with $\vec{k} \perp \vec{B}$, Equation 5 leads to the dispersion relation of compressive magnetosonic waves which however, in the general case, can propagate at other angles as well.

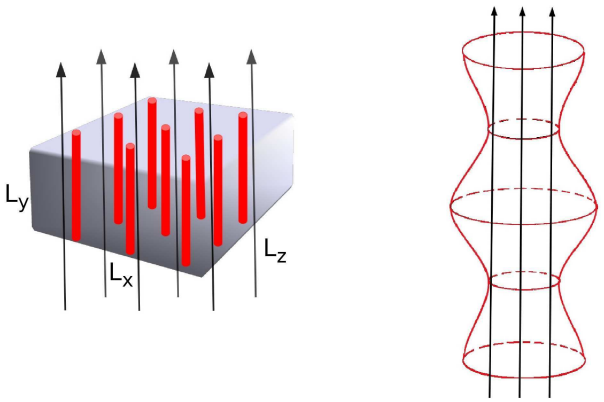

Figure 9. Left panel: cartoon representation of the final configuration from the excitation of magnetosonic waves in both directions perpendicular to the magnetic field. The red cylinders represent density enhancements. Right panel: sausage waves in each cylindrical-like structure of the left panel. Black arrows denote the direction of the ordered magnetic field and the red line represents the morphology of the resulting magnetic flux tube due to perturbations.

In the linear regime Alfvén and fast magnetosonic waves propagate independently. However, when nonlinear terms are non-negligible, plasma density inhomogeneities across the direction of the magnetic field lead to phase mixing of Alfvén waves (Heyvaerts & Priest 1983). As a result, fast magnetosonic waves can be excited even if they are not originally present in the system. Due to density inhomogeneities, there are also regions of varying Alfvén speed where fast magnetosonic waves get refracted and thus, they naturally get trapped inside overdensities or, in other words, in regions of low Alfvén speed.

We now consider an Alfvén wave of the form $Acos\omega(t - y/v_a(x))$, where v_a is the Alfvén speed and A is the amplitude of the wave, travelling along the direction of the unperturbed magnetic field which, as in the previous models, we assume is directed along the y axis. Then, the wave equation for fast magnetosonic waves can be written as:

$$\frac{\partial^2 v_x}{\partial t^2} - v_a^2(x)\Big(\frac{\partial^2 v_x}{\partial x^2} + \frac{\partial^2 v_x}{\partial y^2}\Big) = \frac{\omega A^2}{v_a^2}\frac{dv_a(x)}{dx} \times$$
$$\times\Big[\omega y cos\big(2\omega(t - \frac{y}{v_a(x)})\big) - v_a(x) sin\big(2\omega(t - \frac{y}{v_a(x)})\big)\Big] \quad (6)$$

where we have ignored variations along the z direction. From Equation 6 it can be seen that magnetosonic waves produced due to phase mixing will have twice the wavelength of Alfvén waves. Finally, fast magnetosonic waves travelling across magnetic field lines can get further refracted at the edges of the cloud, at sharp density gradients. For an extensive analytical discussion of the coupling between Alfvén and fast magnetosonic waves we refer the reader to Nakariakov et al. (1997).

When the direction of propagation of the waves is perpendicular to the magnetic field ($\vec{k} \perp \vec{B}$), Equation 5 can be

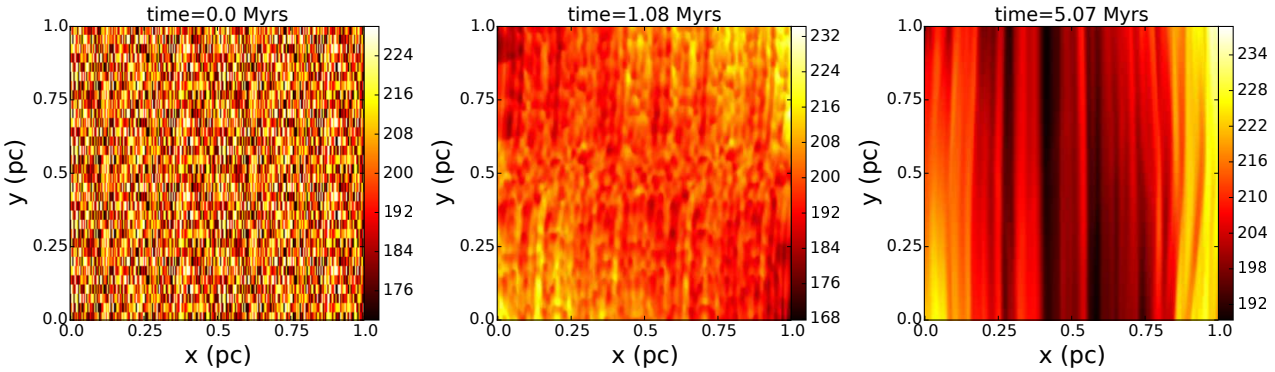

Figure 10. Slice density maps from our 2D simulations for the fourth model. From left to right column the time is 0 Myrs (i.e. the initial condition), $\sim$ 1Myr and $\sim$ 5 Myrs. The contrast is drastically increased compared with the previous three models.

written in component form as:

$$\omega^2 v_x = (c_s^2 + v_a^2)(k_x v_x + k_z v_z)k_x \tag{7}$$

$$\omega^2 v_y = 0 \tag{8}$$

$$\omega^2 v_z = (c_s^2 + v_a^2)(k_x v_x + k_z v_z)k_z \tag{9}$$

where c_s is the sound speed. Consequently, magnetosonic waves travelling in both directions perpendicular to the magnetic field are also coupled to each other. In 3D, the final configuration will be cylindrical-like structures parallel to the magnetic field (left panel of Figure 9).

From the linearized MHD equations in cylindrical coordinates it follows that:

$$B_c = \frac{B_{0c}}{\omega_c}\frac{1}{r_c}\frac{\partial(r_c A(r_c))}{\partial r_c} sin(k_c z - \omega_c t) \tag{10}$$

$$P_c = -\frac{\omega_c \rho_{0c} c_s^2}{(c_s^2 k_c^2 - \omega_c)}\frac{\partial(r_c A(r_c))}{\partial r_c} sin(k_c z - \omega_c t) \tag{11}$$

(Freij et al. 2016). Here, r_c is the radius of each cylindrical-like structure, $A(r_c)$ is the area and P_c, and B_c are the perturbed pressure and magnetic field respectively. As a result, for a cylindrical-like structure, the magnetic pressure and thermal pressure will be out of phase. This excites sausage waves (right panel of Figure 9) along with the other two MHD wave modes.

From the right panel of Figure 9 it can be seen that the cross-sectional area of each flux tube changes. Thus, from Bernoulli's principle, there will be a velocity gradient along the long axis of each streamline. Ignoring gravity and assuming isothermal processes arises:

$$(v_1^2 - v_2^2) = 2c_s^2 ln(\frac{\rho_2}{\rho_1}) \tag{12}$$

where the subscripts denote the velocity and density in different positions along one streamline. Although this is a second order effect, we should expect density and velocity fluctuations along the long axis of the striations.

In order to test if the coupling of Alfvén and fast magnetosonic waves can lead to the formation of striations we perturb the x component of the magnetic field while the ordered component is again towards the y direction. Additionally, we introduce random perturbations in density and thermal pressure in all directions in a self-consistent manner such that isothermality is never violated. All velocity components are initially set to zero. The initial conditions for this model are:

$$v_x = v_y = v_z = 0 \tag{13}$$

$$\rho(x, z) = \rho_0 + \delta\rho(x, y, z) \tag{14}$$

$$P(x, z) = P_0 + \delta P(x, y, z) \tag{15}$$

$$B_y(x, z) = B_0 \tag{16}$$

$$B_x(y) = B_z(y) = \delta B sin(k_y y) \tag{17}$$

where $k_y = \pi/L_y$. This setup implies an Alfvén wave passing through the computational region with wavelength twice the length of the simulated region in the y direction. For these simulations we used a fixed resolution grid with 256×256 cells. Since matter can flow easily along magnetic field lines, the boundary conditions along the direction of the ordered component of the magnetic field are outflow. On the other hand, since magnetosonic waves can get reflected at the edges of the cloud, we use reflective boundaries in the x direction.

Using Hildebrand's et al. (2009) method, a number of authors (e.g. Eswaraiah et al. 2013; Franco & Alves 2015) have found that the ratio of the random component of the magnetic field to the ordered component is of the order of 10% and can be up to 17%. Likewise, using the same method and the results presented in Chapman et al. (2011) it is found that in the northwest part of the Taurus molecular cloud the ratio of the turbulent to the ordered component of the magnetic field is $\sim$ 11%. In general, the ratio of the ordered to turbulent component in molecular clouds can be up to $\sim$ 75% (Houde et al. 2016) and, within uncertainties, it can also be up to 40% in regions where striations appear (Panopoulou et al. 2016b). For the strength of the magnetic field in the striations region in the Polaris flare, Panopoulou et al. (2016b) reported values that ranged up to $\sim$ 80 μG. Since striations appear in regions of well ordered magnetic field our reference value for the amplitude of the perturbation is 15% the background value of each perturbed quantity. However, we further explore how our results depend on this

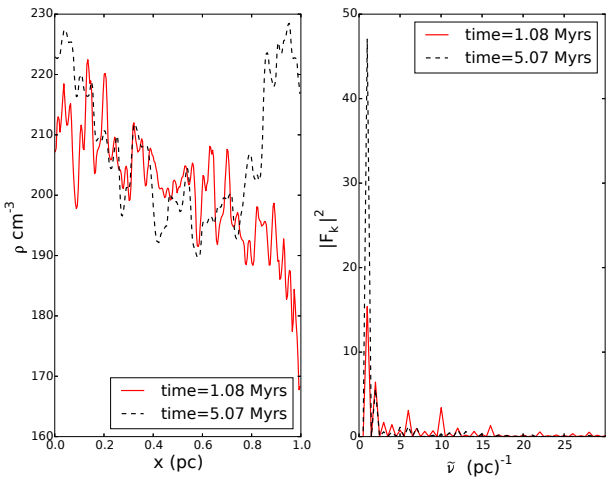

Figure 11. Perpendicular density cuts (left panel) and the spatial power spectrum (right panel) for the timesteps shown in the middle and right panel of Figure 10. The power spectrum resembles observations extremely well.

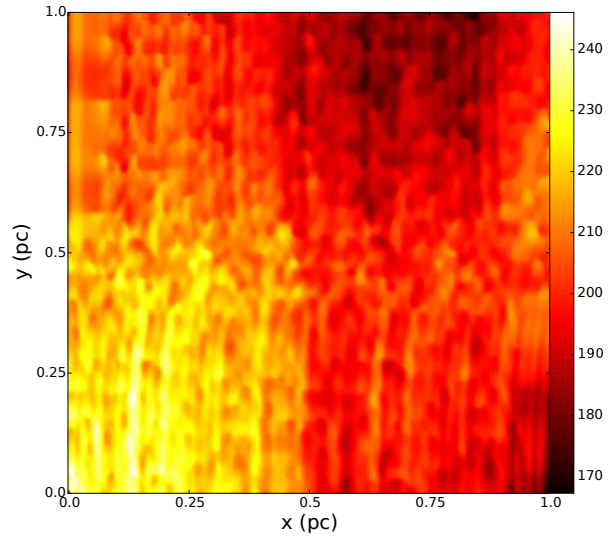

Figure 12. Slice density map from our 2D simulation for the fourth model and for 1 Myr adopting a higher perturbation amplitude of 30%.

parameter by performing a run in which the ratio of the turbulent to ordered component of the magnetic field is 30%. In this run, the amplitude of the perturbation for the density and thermal pressure is still 15% and reference values were adopted for the density and the magnetic field.

Density maps for the fourth model and for our reference run are shown in Figure 10. Not only can this model qualitatively reproduce observations but the contrast is drastically improved compared to the previous models. In fact, following the exact same procedure as in observations where we compute the contrast between adjacent maxima and minima for all perpendicular cuts, the mean contrast is $\sim 4.8\%$. A noticeable feature in the middle panel of Figure 10 is the mirror symmetry between the upper and lower half of

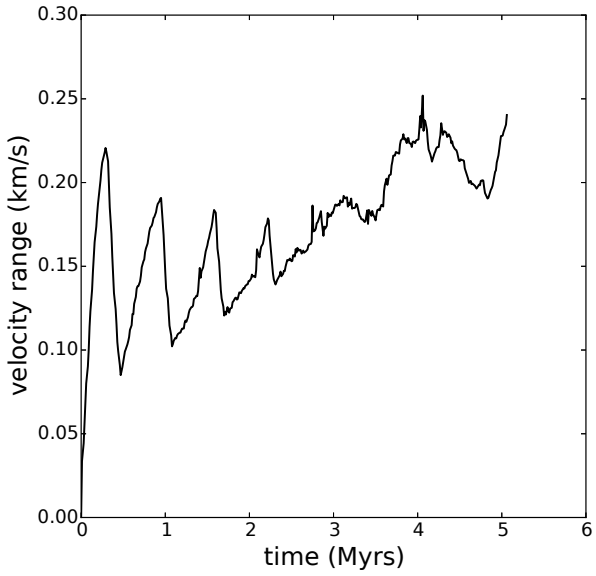

Figure 13. Evolution of the velocity range in the direction perpendicular to the unperturbed magnetic field in the simulation shown in Figure 12. No significant energy decay is seen in this simulation.

the computational region. The reason behind this symmetry is that the derivatives in the nonlinear terms above and bellow the line $y = L_y/2$ appear in opposite signs. Furthermore, the region close to the line $y = L_y/2$ is where phase mixing mainly occurs. Then magnetosonic waves travel towards the lower and upper parts where the Alfvén speed is lower. These features are not so prominent in the right panel due to the outflow boundary conditions. After magnetosonic waves get excited they propagate in all directions, not just perpendicularly to magnetic field lines, and thus escape the computation region. This effect smoothens sharp density gradients and eliminates the mirror symmetry. We find that numerical diffusion does not significantly affect our results (see Apendix A).

In Figure 11 we show perpendicular density cuts (left panel) and the spatial power spectrum (right panel). The solid red and dashed black lines correspond to the middle and right panel of Figure 10 respectively. The power spectrum resembles observations remarkably well. Most of the power is distributed in larger wavelengths and, like observations, there are smaller peaks at larger spatial frequencies. These peaks correspond to the thinner structures seen in the middle and left panels of Figure 10. In agreement with the analytical result from Equation 6, the dominant frequency in the right panel of Figure 11 corresponds to a magnetosonic wave with wavelength two times that of the Alfvén wave initially present in the system.

A density map from our simulation in which the amplitude of the perturbation is 30% is shown in Figure 12. The mean contrast in this simulation is 7.7%. In Figure 13 we show the evolution of the maximum range of the x velocity component for 5 Myrs from the same run. When the amplitude of the Alfvén wave initially present in the system is large compared to the ordered component there is no significant energy decay. Basu & Dapp (2010) were the first

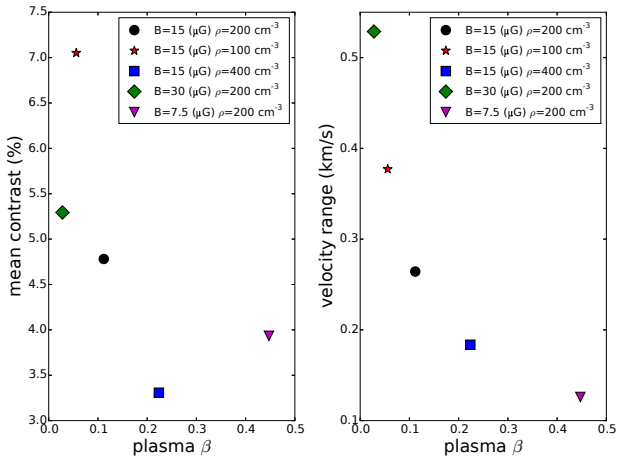

Figure 14. Left panel: mean contrast as a function of plasma β for our fourth model. The time in all parameter runs is ~ 5 Myrs. In the simulations with lower plasma β the contrast is larger. Right panel: Velocity range as a function of plasma β for our fourth model. The lower the plasma β the greater the velocity range reached throughout the simulation.

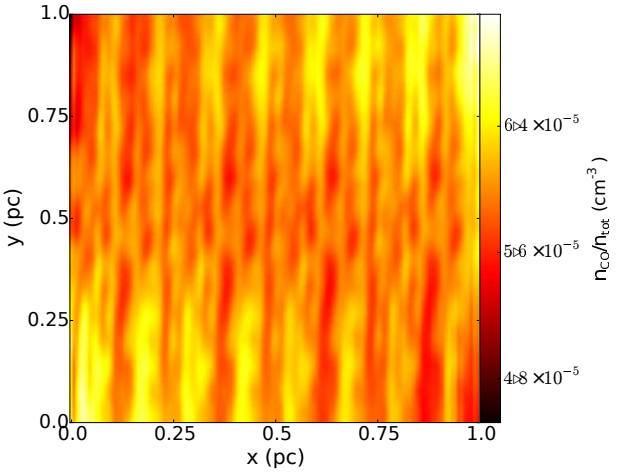

Figure 15. CO abundance map for 1 Myr adopting our fourth model. In comparison to the middle panel of Figure 10 striations are more prominent when seen through the chemical lens.

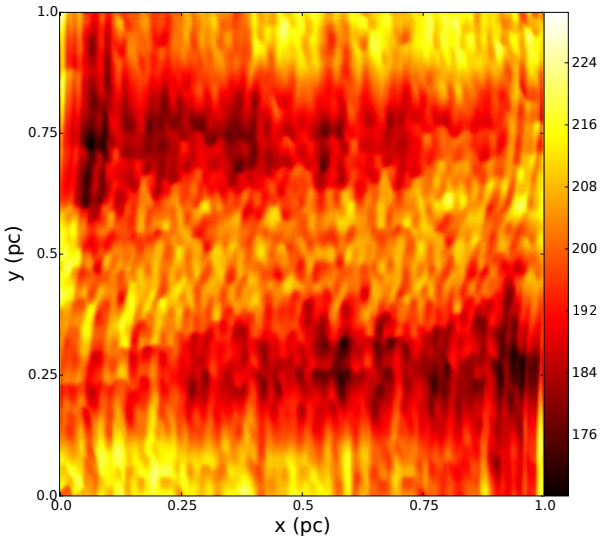

Figure 16. Slice density map from our 2D simulation with 30% perturbation amplitude and a spectrum of Alfvén waves initially present in the system. The time is 1 Myr. The final density configuration is eve more realistic.

to report long-lived MHD modes without any dissipation in their simulations. The evolution of the maximum range of the x velocity component for the simulation with lower perturbation amplitude is given in Appendix A.

Since for this model results adopting reference parameters were in fairly good agreement with observations we additionally explored how the density contrast and velocity range changed by altering the initial density and the magnetic field strength a factor of two above and bellow the reference values. Furthermore, since striations are also observed in CO emission lines we couple one of our 2D runs with a non-equilibrium chemical model and investigated the correlation between CO abundance and the total density. Our chemical network consists of 13967 reactions that govern the evolution of 214 gas-phase species and 82 dust grain species. For the chemical modelling we assume a mean molecular weight of $\sim$ 2.4, a standard value of $\zeta = 1.3 \times 10^{-17}$ s^{-1} for the cosmic-ray ionization rate, the visual extinction is $A_v = 1$ mag and the temperature is constant and equal to 15 K. A list of the species included in the chemical network and values for the initial elemental abundances are given in Tritsis et al. (2016).

In the left panel of Figure 14 we show the mean contrast as a function of the mean plasma β for a time of 5 Myrs. The contrast has again been computed in the exact same manner as in observations. We find that the contrast is affected by both the value of the magnetic field and density independently, although the highest values are obtained for low plasma β. In the right panel of Figure 14 we plot the maximum velocity range reached throughout each simulation in our parameter study as a function of the mean plasma β. The lower the plasma β, the greater the velocity range. The velocity range has a clear relation with plasma β. In fact, it scales as $\sim 1/\sqrt{\beta}$.

In Figure 15 we show a CO abundance map from the 2D simulation in which we have included chemical modelling. The time is 1 Myr and thus it corresponds to the middle panel of Figure 10. Striations seen in the CO abundance map are more prominent than the ones seen in the total density map. The differences seen in the two maps are not just qualitative. The mean contrast that arises from the CO abundance map is 6.3 % in comparison to 4.8 % from the density map. The reason behind this discrepancy is the difference between dynamical and chemical timescales.

In the setup adopted so far for the 2D simulations we only considered one Alfvén wave passing through the computational area with wavelength two times the length of the y direction. In nature, we should expect a spectrum of Alfvén waves. Smaller and sharper distortions of the magnetic field would lead to larger gradients which would in turn make non-linear terms even more significant and lead

to larger velocity ranges. We thus performed an additional 2D simulation where a superposition of three Alfvén waves with random phases was initially present in the system. The total amplitude of the perturbation in this simulation was 30% with the amplitude of each Alfvén wave decreasing with wavelength. Specifically, the ratio of amplitudes of the longest and intermediate wavelengths with respect to the shortest wavelength was three and two respectively. A density map from this simulation is shown in Figure 16. The final configuration is even more realistic and the similarity with dust continuum observations of the striations region in the Polaris flare (Miville-Deschênes et al. 2010) is remarkable. The maximum velocity range along the x direction achieved throughout this simulation was $\sim$0.53 km/s, i.e more than a factor of two larger than in the simulation with the same total perturbation amplitude and just one Alfvén wave.

In order to examine the properties of striations in velocity slices we run additional 3D simulations of the same model considering two different lengths for the LOS dimension, 0.25 pc and 0.125 pc. In these simulations we adopt values for the unperturbed density and magnetic field that best agree with observations as these have arisen from the parameter study in our 2D simulations. The unperturbed magnetic field is 30 μG and the number density is set at 100 cm^{-3}. These values are still well within observational limits. We also perturb the z component of the magnetic field along with the x component. In equivalence to our reference 2D simulation of the same model we only consider one Alfvén wave with wavelength twice the length of the y direction. The boundary conditions along the z axis are reflective and along the other two directions are kept as in our 2D simulations.

The velocity range along the LOS in both our 3D simulations is $\sim$ 0.9 km/s. In the simulation where the LOS dimension is 1/4 that of the other two the maximum velocity range is obtained for $\sim$ 0.95 Myrs whereas when the LOS is even shorter the maximum range is achieved later on during the evolution. We find that the simulation where the length of the z dimension is 0.25 pc can better reproduce observations. In the left panel of Figure 17 we show a perpendicular cut from a column density map. In the right panel we plot the spatial power spectra of two velocity slices which are 0.2 km/s apart. In complete analogy with observations the two slices exhibit the same spatial frequencies with respect to each other.

Secondary effects associated with the excitation of sausage MHD wave modes were also retrieved in our 3D simulations. In the data cube we first identified a continuous elongated structure and then examined the correlation between the velocity and density along that structure. In Figure 18 we plot the volume density (black dashed line) and the velocity (red line) throughout this striation. As expected from Bernoulli's principle the variation of density is in antiphase with the variation in velocity. A noticeable feature seen in Figure 18 is that a spectrum of sausage waves is excited, the superposition of which determines the final velocity and density variations. In this particular striation the effect is small compared to other regions inside the computational box. However, we chose to present results for this structure since it was one of the most clear cases and free of other effects, such as Alfvén waves, that could lead to a more complicated interpretation as to why these density and velocity variations occur.

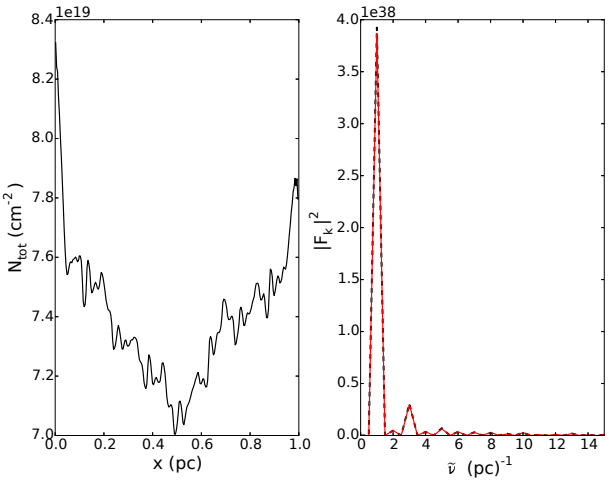

Figure 17. Left panel: A perpendicular cut to the long axis of the striations. The cut has arose from a column density map from the simulation where z=0.25 pc and when the time is 0.95 Myrs. Right panel: spatial power spectra of two velocity slices. The velocity slices are $\sim$ 0.2 km/s apart. In absolute agreement with observations the two velocity slices exhibit the same spatial frequencies.

Even for the example shown in Figure 18 where the change in velocity due to the excitation of sausage MHD waves is marginal, the effect may be observable. The velocity resolution of ALMA at a frequency of 110 GHz is 0.01 km/s. Thus, the velocity resolution from observations of C^{18}O ($J = 1 \rightarrow 0$) emission at 109.78 GHz should be sufficient for the effect to be observed. Volume density variations could be derived by observing an additional C^{18}O transition and examining the line ratio.

The change in the cross sectional area of the striations is also of interest. If variations of the width along a single striation are found to be statistically significant, then the ratio of widths could be used to constrain the turbulent to ordered component of the magnetic field. The ratio of the width variance and the mean width should be proportional to the ratio of the turbulent and ordered component of the magnetic field:

$$\frac{A(r_c)}{A(r_{c0})} = -\frac{B_c}{B_{c0}} \tag{18}$$

(Grand et al. 2015) where $A(r_c)$, $A(r_{c0})$, B_c and B_{c0} are defined as in Equations 10 and 11. Variations of the width along a single striation could be measured with an algorithm such as FilTER (Panopoulou et al. 2016a) although, due to projection effects, this relation should be used with caution.

5 SUMMARY AND DISCUSSION

The current picture for the formation of striations includes streams that flow along magnetic field lines. We performed numerical simulations adopting two models involving such streamers, a model in which elongated structures are created as a result of a Kelvin-Helmholtz instability perpendicular

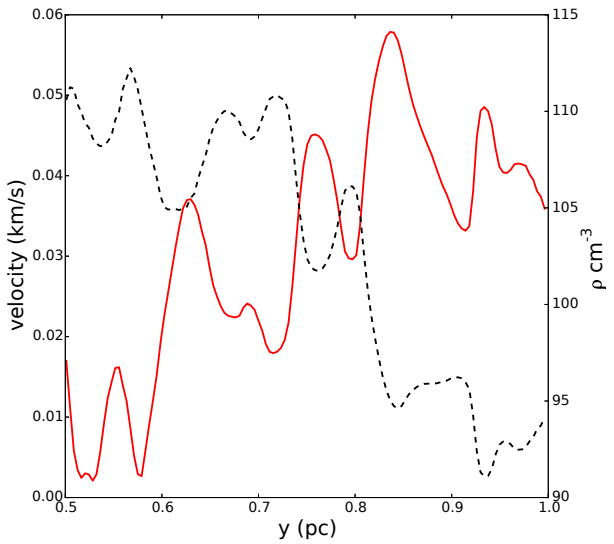

Figure 18. Density (black dashed line) and velocity variation (red line) along one continuous structure from our 3D simulations with z=0.25 pc in our fourth model. In agreement with Equation 12 an increase in velocity results in a decrease in density. These variations can be realized through the excitation of sausage MHD wave modes.

to field lines and a new model in which striations are formed from the excitation of magnetosonic waves. We assessed the validity of each of our models by comparison between simulated and observational results based on four criteria:*a*) the contrast between minima and maxima in density and column density maps *b*) the spatial power spectrum in each velocity slice and in column density *c*) the kinematic properties (i.e. velocity range) *d*) whether the abundance of CO follows the total density and the contrast in abundance is significant for striations to be observed. We proved that flows, either sub-Alfvénic or super-Alfvénic, cannot reproduce the observed contrast even for huge velocity differences between ambient streamlines. The maximum possible contrast in the simulations involving flows is $\sim$ 0.03 %. The mean contrast in observations is $\sim$ 25 %.

In our second model in which super-Alfvénic streamers flow along magnetic field lines, the contrast is low in both the 2D and 3D models. That is because the thickness of the LOS dimension is constant and thus cancelled out when computing the contrast in column density maps. As a result, projection effects are of minor importance and the observed contrast is an intrinsic density contrast rather than a geometrical effect.

Flows perpendicular to field lines is a mechanism that can also qualitatively produce elongated structures. However, due to development of turbulence, these structures are not long-lived. Furthermore, specific projection angles are required so that these structures are seen parallel to the magnetic field. A scenario in which this mechanism can simultaneously produce low density striations parallel to field lines and dense filaments perpendicular to the magnetic field is also difficult to realize. Finally and most importantly, such flows fail to reproduce the observed contrast of striations by more than three orders of magnitude. Overall, this mechanism cannot account for the formation of striations.

In the low column density parts of molecular clouds there is good coupling between matter and magnetic field since the degree of ionization is large. Hence, in a paradigm where magnetic field lines act as flux tubes and striations are formed from flows along field lines there must also be regions of stronger and weaker magnetic field. By definition however, such a configuration is equivalent to a wave travelling perpendicular to the long axis of the striations. The quasi-periodicity seen in perpendicular cuts in observations also suggests a formation mechanism which includes superposition of waves.

In contrast to streamers, a model including coupling of MHD waves is physical and can naturally explain the formation of striations. Furthermore, for a certain set of parameters the contrast can be up to 7 %. Besides the large number of combinations (length of LOS dimension, density and magnetic field values) that can be realized and could alter this value, it would certainly be enhanced due to chemical effects. Radiative transfer effects might also be important in an intensity map. Therefore, we conclude that this model can account for the observed contrast.

However, even in the 3D simulations performed here the total velocity range over which striations appear is a factor of $\sim$3 smaller compared to observations. There is a number of possibilities to explain this shortcoming. First, intrinsic magnetic field and density values in Taurus could be outside the parameter space considered. From the right panel of Figure 14 it can be seen that the lower the plasma β the larger the velocity range. The amplitude of the perturbation is also a key parameter that affects both the maximum range and the evolution of each velocity component. A second possibility is the existence of multiple sheet-like resonant structures along the LOS which move with respect to each other. In such a picture all of these sheet-like structures should have approximately the same boundaries in order for the same dominant frequency to be present in the spatial power spectrum in all velocity slices. We have demonstrated that when we consider a spectrum of Alfvén waves initially present in the system results are even more realistic and the velocity range increases by more than a factor of two compared to the simple case of having one Alfvén wave. Altering the distribution of power could further increase the velocity range. Although numerical dissipation does not significantly affect the velocity range (see Appendix A), the growth of transversal gradients could be affected by the boundary conditions.

In a recent paper Hacar et al. (2016) presented a thorough analysis of the CO data also used in this paper. They concluded that suprathermal CO linewidths could be explained from optical-depth effects and multiple narrow components the superposition of which act as a broadening mechanism. Based on this interpretation of CO linewidths they suggested that intrinsic gas motions were transonic. As a result, the velocities found for the majority of the simulations in the parameter study could be within observational ranges.

Despite the observational features for which our fourth model can account for, the question arises why we considered incompressible Alfvén waves initially present in the system rather than directly setting up compressible magnetosonic waves. Alfvén waves are exact solutions of the equations of ideal MHD and are thus longlived. Zweibel & Josafatsson (1983) studied the damping mechanisms of MHD waves and

naturally found that Alfvén waves were the longest lived mode. Alfvén waves can also act as the energy carriers from remote regions than the ones where striations are formed and are ultimately observed. Hence, in this model, they arise naturally as the source from which magnetosonic waves pump energy. The spectrum of Alfvén waves passing through an inhomogeneous region is of great importance. The energy distribution in the power spectrum will ultimately be a function of the properties of Alfvén waves initially present in the system. Consequently, the power spectrum of striations could be used to study the spectrum of Alfvén waves present in that region. We intend to return to the problem in follow-up publication with more 3D simulations and a larger parameter space. The effect that different dimensions and projection angles have on the power spectrum is also left for future study.

Mouschovias (1987) predicted that torsional Alfvén waves can naturally be generated by the rotation of a clump and can also be trapped between magnetically linked clumps. Just as linear Alfvén waves, in the non-linear regime, torsional Alfvén waves can also excite fast magnetosonic waves (Tirry & Berghmans 1997). As a result, striations connected to denser filaments could also be explained through the same mechanism. Thus, the interplay between Alfvén and magnetosonic waves along with acoustic waves and gravitational contraction along magnetic field lines is a promising scenario for explaining the overall gas-magnetic field morphology. Additional 3D simulation including gravity, will determine if the phase mixing between torsional Alfvén waves and fast magnetosonic waves can reproduce the observed properties of striations associated with denser parts of molecular clouds.

Elongated structures, usually referred to as fibers, have also been observed at high Galactic latitudes in the diffuse interstellar medium (see Clark et al. 2015 and references therein). Similar to striations, the magnetic field in these regions is well ordered and parallel to fibers which again exhibit quasi-periodicity. Thus, it is possible that striations and fibers share a common formation mechanism.

ACKNOWLEDGEMENTS

We thank G.V. Panopoulou, T. Mouschovias, V. Pavlidou and P. Goldsmith for useful comments and discussions. We also thank the anonymous referee for helpful suggestions that improved this paper. The software used in this work was in part developed by the DOE NNSA-ASC OASCR Flash Center at the University of Chicago. For post processing our results we partly used yt analysis toolkit (Turk et al. 2011). K.T. and A.T. acknowledge support by FP7 through Marie Curie Career Integration Grant PCIG- GA-2011-293531 "SFOnset". A.T. and K.T. would like to acknowledge partial support from the EU FP7 Grant PIRSES-GA-2012-31578 "EuroCal". Usage of the Metropolis HPC Facility at the CCQCN of the University of Crete, supported by the European Union Seventh Framework Programme (FP7-REGPOT-2012-2013-1) under grant agreement no. 316165, is also acknowledged.

REFERENCES

Alves, F. O., Franco, G. A. P., & Girart, J. M. 2008, A&A, 486, L13
Alves de Oliveira, C., Schneider, N., Merín, B., et al. 2014, A&A, 568, A98
André, P., Di Francesco, J., Ward-Thompson, D., et al. 2014, Protostars and Planets VI, 27
Arons, J., & Max, C. E. 1975, ApJL, 196, L77
Basu, S., & Dapp, W. B. 2010, ApJ, 716, 427
Berné, O., Marcelino, N., & Cernicharo, J. 2010, Nature, 466, 947
Berné, O., & Matsumoto, Y. 2012, ApJL, 761, L4
Chandrasekhar, S., & Fermi, E. 1953, ApJ, 118, 113
Chandrasekhar, S. 1961, International Series of Monographs on Physics, Oxford: Clarendon, 1961,
Chapman, N. L., Goldsmith, P. F., Pineda, J. L., et al. 2011, ApJ, 741, 21
Clark, S. E., Peek, J. E. G., & Putman, M. E. 2014, ApJ, 789, 82
Clark, S. E., Hill, J. C., Peek, J. E. G., Putman, M. E., & Babler, B. L. 2015, Physical Review Letters, 115, 241302
Dubey, A., Fisher, R., Graziani, C., et al. 2008, Numerical Modeling of Space Plasma Flows, 385, 145
Eswaraiah, C., Maheswar, G., Pandey, A. K., et al. 2013, A&A, 556, A65
Franco, G. A. P., & Alves, F. O. 2015, ApJ, 807, 5
Frank, A., Jones, T. W., Ryu, D., & Gaalaas, J. B. 1996, ApJ, 460, 777
Freij, N., Dorotovič, I., Morton, R. J., et al. 2016, ApJ, 817, 44
Fryxell, B., Olson, K., Ricker, P., et al. 2000, ApJS, 131, 273
Grant, S. D. T., Jess, D. B., Moreels, M. G., et al. 2015, ApJ, 806, 132
Goldsmith, P. F., Heyer, M., Narayanan, G., et al. 2008, ApJ, 680, 428
Hacar, A., Alves, J., Burkert, A., & Goldsmith, P. 2016, arXiv:1603.08521
Hendrix, T., Keppens, R., & Camps, P. 2015, A&A, 575, A110
Hennemann, M., Motte, F., Schneider, N., et al. 2012, A&A, 543, L3
Heyer, M. H., & Brunt, C. M. 2012, MNRAS, 420, 1562
Heyer, M., Goldsmith, P. F., Yildiz, U. A., et al. 2016, arXiv:1606.08858
Heyvaerts, J., & Priest, E. R. 1983, A&A, 117, 220
Hildebrand, R. H., Kirby, L., Dotson, J. L., Houde, M., & Vaillancourt, J. E. 2009, ApJ, 696, 567
Houde, M., Hull, C. L. H., Plambeck, R. L., Vaillancourt, J. E., & Hildebrand, R. H. 2016, ApJ, 820, 38
Lee, D. 2013, Journal of Computational Physics, 243, 269
Li, H.-b., Fang, M., Henning, T., & Kainulainen, J. 2013, MNRAS, 436, 3707
Malinen, J., Montier, L., Montillaud, J., et al. 2015, arXiv:1512.03775
Miville-Deschênes, M.-A., Martin, P. G., Abergel, A., et al. 2010, A&A, 518, L104
Moneti, A., Pipher, J. L., Helfer, H. L., McMillan, R. S., & Perry, M. L. 1984, ApJ, 282, 508
Mouschovias, T. C. 1987, NATO ASIC Proc. 210: Physical Processes in Interstellar Clouds, 491
Mouschovias, T. C., & Psaltis, D. 1995, ApJL, 444, L105
Nakariakov, V. M., Roberts, B., & Murawski, K. 1997, SoPh, 175, 93
Palmeirim, P., André, P., Kirk, J., et al. 2013, A&A, 550, A38
Panopoulou, G. V., Tassis, K., Goldsmith, P. F., & Heyer, M. H. 2016a, Astrophysics Source Code Library, ascl:1602.007
Panopoulou, G. V., Psaradaki, I., & Tassis, K. 2016b, arXiv:1607.00005
Pereyra, A., & Magalhães, A. M. 2004, ApJ, 603, 584
Planck Collaboration, Adam, R., Ade, P. A. R., et al. 2014, arXiv:1409.6728

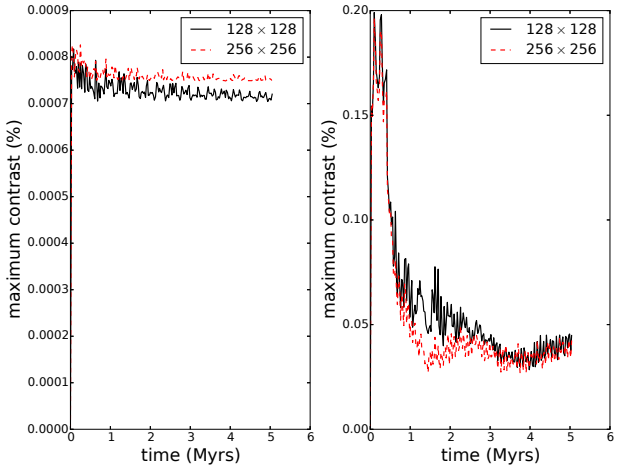

Figure A1. Evolution of the maximum contrast as a function of time for the two streamer models. With the solid black line we plot our result from the simulation with 128×128 grid points and with the dashed red line the results from the simulation with a resolution of 256×256 points.

Qian, L., Li, D., Offner, S., & Pan, Z. 2015, ApJ, 811, 71
Sugitani, K., Nakamura, F., Watanabe, M., et al. 2011, ApJ, 734, 63
Tirry, W. J., & Berghmans, D. 1997, A&A, 325, 329
Tritsis, A., Tassis, K., & Willacy, K. 2016, MNRAS, 458, 789
Turk, M. J., Smith, B. D., Oishi, J. S., et al. 2011, ApJS, 192, 9
Zweibel, E. G., & Josafatsson, K. 1983, ApJ, 270, 511

APPENDIX A: CONVERGENCE TESTS

In Figure A1 we show the contrast as a function of time for both models involving flows along magnetic field lines for two different resolutions. In the left panel we plot our results for the sub-Alfvénic streamers and in the right results for the super-Alfvénic flow along field lines model. Because of the random number generator we used to initialize both problems different velocity values were assigned to grid cells which in turn led to the minor differences seen in both panels. However, in both cases, the lines follow the same trend and our results converge. The contrast has not be computed as described in § 2. Instead, it is the maximum contrast inside the entire computation region.

In principle, numerical dissipation can stop the growth of transversal gradients very fast. If so, magnetosonic waves do not have time to pump enough energy from Alfvén waves for the observed velocities to be reached. However, as can be seen in Figure A2 where we show the evolution of the maximum velocity in the x direction for our fourth model and for two different resolutions, results converge. Therefore, numerical diffusivity does not significantly affect the velocity range. Even so, the growth of transversal gradients may still be affected by the boundary conditions.

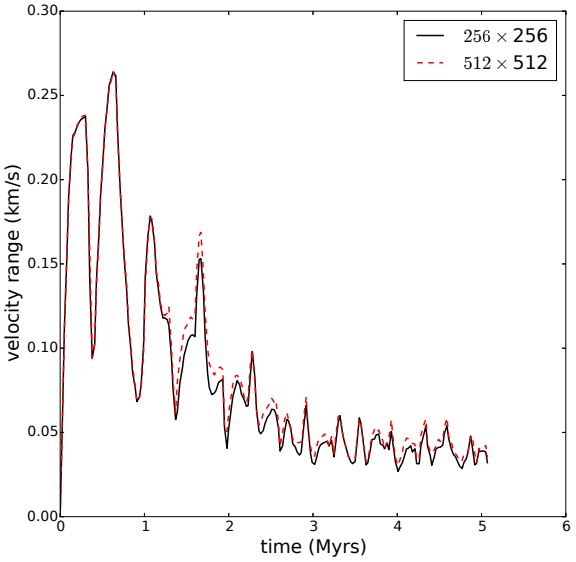

Figure A2. Evolution of the x velocity component as a function of time. With the solid black line we plot our result from the simulation with 256×256 grid points and with the dashed red line the results from the simulation with a resolution of 512×512 points.

Chapter 3

The global structure of a molecular cloud

Based on the result that striations are formed due to waves (Chapter 2) it is expected that normal modes should be establish in the case of an isolated cloud. We have examined dust emission maps from Herschel and we have identified such an oscillating region towards the Musca molecular cloud. This is the first-ever discovery of normal modes in an interstellar cloud. The Musca molecular cloud is considered to be the most representative example of an interstellar filament. Due to the fact that it is isolated and it exhibits a well ordered morphology the predictions of theoretical models of filament formation are preferentially tested against observational surveys conducted towards Musca (see for example Myers 2017). It consists of a moderately dense, continuous elongated structure with perpendicularly orientated striations. The magnetic field is oriented perpendicularly to the dense main body of the cloud and parallel to striations. Our discovery has allowed us to reconstruct the 3D shape of the cloud. We have found that, contrary to common wisdom, Musca is not in fact a filament. It is a sheet-like structure with its line-of-sight dimension being comparable to its largest dimension as this is projected on the plane-of-the-sky.

This result is theoretically expected in a magnetically dominated cloud evolution scenario. Magnetic pressure forces are exerted on the direction perpendicular to the magnetic field, while along field lines the cloud is allowed to collapse freely under its self-gravity, until thermal pressure becomes important. Thus, the resulting configuration will be that of a sheet-like, oblate or disk-like structure with an ordered magnetic field oriented parallel to the shortest axis of the cloud (Mouschovias 1987).

Magnetic seismology of interstellar clouds: unveiling the hidden dimension

Aris Tritsis[1] & Konstantinos Tassis[1,2]

[1]Department of Physics and ITCP [*], University of Crete, PO Box 2208, 71003 Heraklion, Greece
[2]IESL, Foundation for Research and Technology-Hellas, PO Box 1527, 71110 Heraklion, Crete, Greece June 13, 2017

Stars, planets, and ultimately life all trace their origin to interstellar clouds. Despite its significance, the physics that controls the evolution of these clouds and the formation of stars is still poorly understood and hotly debated. This physics, which involves gravity, turbulence, magnetic fields and complex chemical and radiative processes, is imprinted in the 3D shape of clouds. Unfortunately, one of the most fundamental constraints in astrophysics is that astronomical objects are seen as two-dimensional projections on the plane of the sky. For the first time ever, we solve this problem by identifying resonant magnetohydrodynamic (MHD) "ringing" in an isolated interstellar cloud and analysing its normal modes. This is the first cloud found to be vibrating globally, and the largest structure in the Galaxy to which a normal-mode analysis has been successfully applied to date. This discovery allows us to precisely determine the physical dimensions of the cloud and reconstruct its physical properties through 3D MHD simulations.

Normal modes have been used extensively to describe and analyse various systems in the entire spectrum of physical sciences, from quantum mechanics and helioseismology, to geophysics and structural biology. With the exception of a small pulsating condensation inside a molecular cloud[1], normal modes have been underexplored in interstellar medium (ISM) studies. This is not due to oversight, but rather because molecular clouds usually exhibit a "messy" morphology with complex networks of filamentary structures, as a result

[*]Institute for Theoretical and Computational Physics, formerly Institute for Plasma Physics

of turbulent mixing[2].

In contrast to this general trend, recent wide-field radio observations of molecular clouds[3] have unveiled the presence of a new type of structure in their low column density parts: well-ordered, quasi-periodically spaced elongations, termed striations. The state-of-the-art thermal dust continuum emission survey of nearby molecular clouds by the *Herschel* Space Observatory has shown that striations are a common feature of clouds[4–8]. In these *Herschel* observations, striations are often associated with denser filaments[5–8], inside which stars are formed. Complementary polarimetric studies have revealed that striations are always well-aligned with the magnetic field[3,5–9].

From a theoretical perspective, the only viable mechanism for the formation of striations involves the excitation of fast magnetosonic waves[10]. Compressible fast magnetosonic waves can be excited by their nonlinear coupling with Alfvén waves and/or from perturbations created by self-gravity in an inhomogeneous medium. These waves compress the gas and create ordered structures parallel to magnetic field lines, in agreement with observations.

Once magnetosonic waves are excited, they can be reflected in regions of varying Alfvén speed, setting up normal modes, just like vibrations in a resonating chamber. In regions where striations appear to be autonomous structures, this resonating chamber may be the result of external pressure confinement by a more diffuse, warmer medium. However, boundaries can also be naturally created in the case of a contracting self-gravitating cloud as a result of steep changes in density and magnetic field that in turn lead to sharp variations in the velocity of propagation of these waves (see Methods section '3D model of Musca'). Any compressible fast magnetosonic waves excited during the collapse will then be trapped, thus resulting in striations in the vicinity of denser structures.

Fast magnetosonic waves travelling in both directions perpendicular to the magnetic field are coupled[10]. By considering a rectangular box the spatial frequencies of normal modes are given by:

$$k_{mn} = \sqrt{\left(\frac{\pi n}{L_x}\right)^2 + \left(\frac{\pi m}{L_y}\right)^2} \qquad (1)$$

where the ordered component of the magnetic field is considered to be along the z direction, and $\mathrm{L_x}$ and $\mathrm{L_y}$ are the sizes of the box in the x and y directions respectively. In Eq. (1) n and m are integers ranging from zero to infinity. By considering a rotation matrix it is trivial to show that the spatial power spectrum should be independent of the projection angle.

Here, we analyse this magnetohydrodynamic "song" seen at Musca, a molecular cloud located at ~ 150 parsecs from Earth[11]. Due to its very elongated and strikingly ordered morphology and its low column density, Musca is considered to be the prototype of a filamentary/cylindrical molecular cloud[7,12–15] against which many theoretical models are put to test. For this reason, a robust reconstruction of its 3D structure would have a wide-range significance in in-

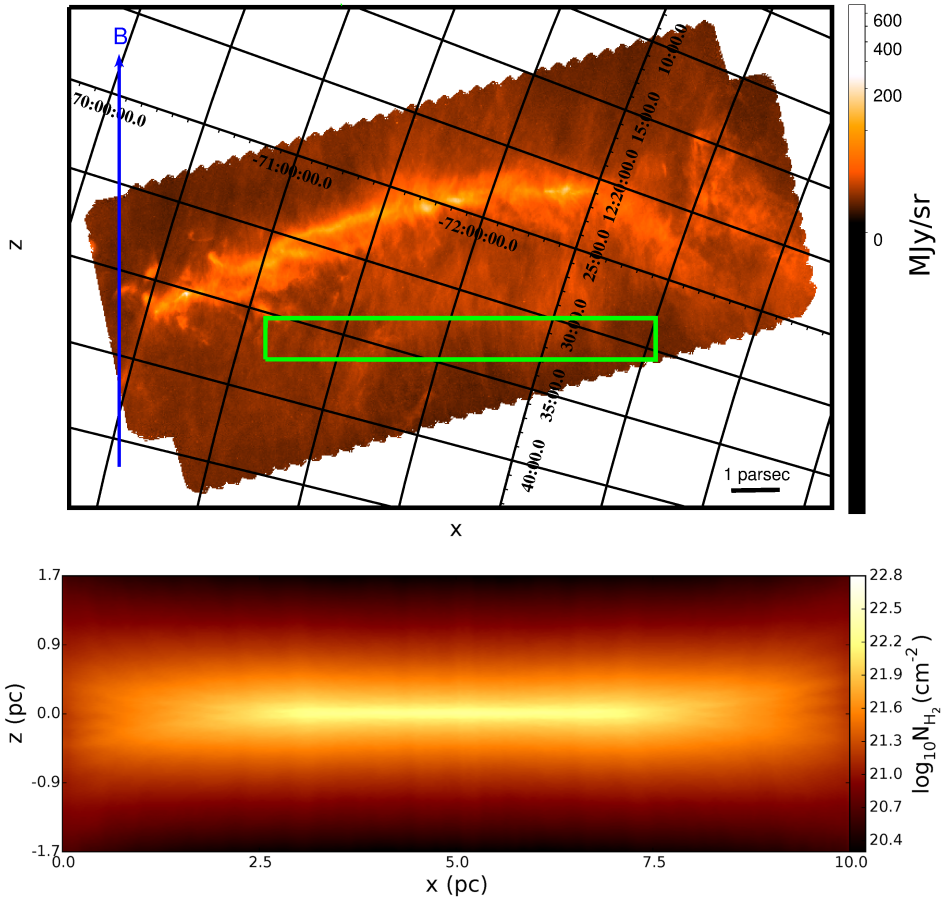

Figure 1 | The observed and simulated Musca molecular cloud Upper panel: *Herschel* 250 μm dust emission map of the Musca molecular cloud depicting both striations and the dense elongated structure. The green rectangle marks the region where we have performed our normal-mode analysis and the blue arrow shows the mean direction of the magnetic field. Grid lines show the sky equatorial coordinates. Lower panel: Edge-on view of the molecular gas column density from our MHD simulation of a sheet-like structure. The color bar shows the logarithm of the column density. The magnetic field is along the z axis.

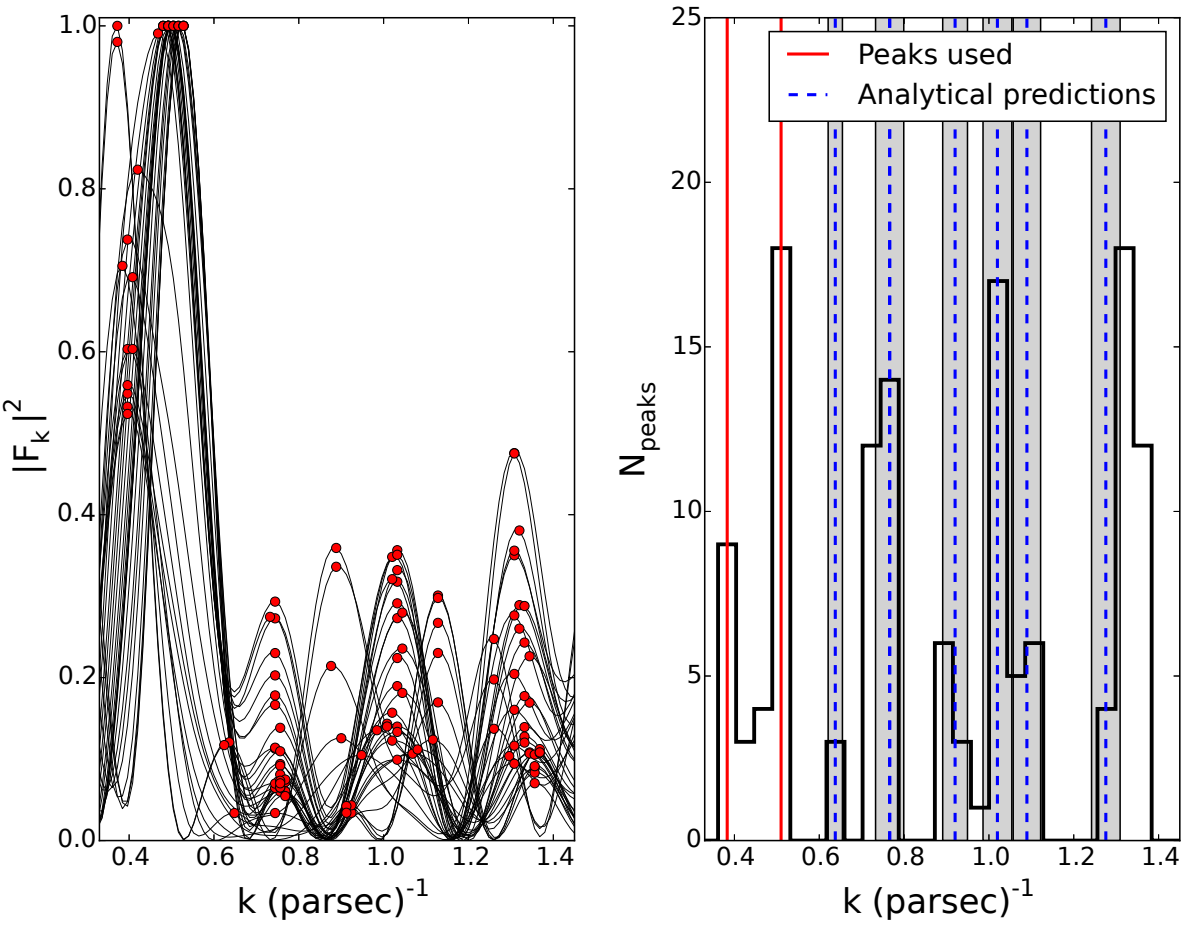

Figure 2 | Comparison of observed normal modes with analytical solution Left panel: Normalized power spectra of cuts perpendicular to the striations (black lines) along with the identified peaks marked with red dots. Right panel: Distribution of peaks at different spatial frequencies. The red lines depict the values used to derive the dimensions of the cloud. The blue dashed lines show the rest of the normal modes (up to n, m = 2), predicted analytically from Eq. (1) given the cloud dimensions derived from the first two peaks. Shaded regions indicate the 1σ regions of the analytical predictions due to uncertainties in the determination of the location of the first two peaks, propagated through Eq. (1). The bin size is comparable to the standard deviations of the points comprising the first two peaks.

terstellar medium physics. Musca has been mapped by *Herschel* as part of the Gould Belt Survey[7] and exhibits clear striations oriented perpendicularly to the main body of the cloud. In the upper panel of Fig. 1 we show the *Herschel*-SPIRE 250 μm dust emission map of Musca. The blue arrow marks the mean direction of the magnetic field[7]. The green rectangle marks the region inside which we have considered cuts perpendicular to the long axis of striations in order to study their spatial power spectra (see the Methods section 'Observations' for details on the selection of the green region). We have verified that our selection of the green rectangle does not introduce biases by performing the same analysis in other regions as well. The spatial frequencies that appear in these regions are practically identical to the ones presented here. This further strengthens the theoretical prediction that striations are normal modes.

The normalized power spectra from all cuts and the distribution of the identified peaks are shown in the left and right panels of Fig. 2 respectively. The value of the first peak in the left panel of Fig. 2 has to correspond to (n, m) = (1, 0) which, assuming L_x is the largest dimension of the cloud, yields $L_x = 8.2 \pm 0.3$ parsecs. This value is in excellent agreement with the observed size of the cloud on the plane of the sky[7,13,16]. The second peak could correspond to either (n, m) = (0, 1) or, in the case of a cylindrical cloud with $L_x \gg L_y$, to (n, m) = (2, 0). However, with $L_x \sim 8$ parsecs, the (n, m) = (2, 0) peak lies at k $\sim$ 0.8 $(\text{parsec})^{-1}$, much higher than the actual location of the second peak. Thus, this second peak has to correspond to (n, m) = (0, 1). Inserting (n, m) = (0, 1) and the value of the second peak in Eq. (1), the hidden, line of sight dimension L_y is revealed to be equal to 6.2 ± 0.2 parsecs, comparable to the largest dimension of the cloud. The rest of the normal modes with their uncertainties determined through error propagation (blue dashed lines and blue shaded regions in right panel of Fig. 2) are predicted analytically by inserting these values for L_x and L_y into Eq. (1) and, as is visible from Fig. 2 (right), are in excellent agreement with observations. Thus, in contradiction to conventional wisdom, Musca, once considered to be the prototypical cylindrical/filamentary cloud, is in fact a sheet-like structure seen edge-on.

In Fig. 2 we plot all the normal modes up to m, n = 2. In reality, the shape of the cloud is more complicated than a rectangle, exhibiting higher order anomalies on smaller scales, and the normal modes may be better fitted considering a rectangle with rounded edges or an ellipse. Thus, Eq. (1) will be an adequate fit only to the normal modes in small spatial frequencies, i.e. large physical scales. Distinct peaks in the histogram of the spatial frequencies are recovered in smaller scales as well, up to the point where the density of normal modes becomes so high that any discriminating power is lost.

Through ideal MHD simulations with self-gravity, we proceed to construct a 3D model of Musca, including the dense structure and striations in the low-density parts. In the lower panel of Fig. 1 we show the column density map from the simulation that reproduces the observed dimensions of the cloud. A 3D representation of the volume density of

the model of Musca is shown in Fig. 3. As intuitively expected from the analysis of the observations, the shape of the cloud is that of a rectangle with rounded edges.

The maximum column density in the simulation, assuming an edge-on view like the one presented, is $1.9 \cdot 10^{22}$ cm^{-2}. For comparison, the maximum column density as derived observationally from dust emission maps[7] is $\sim 1.6 \cdot 10^{22}$ cm^{-2}. The maximum number density in the simulation is $\sim 2 \cdot 10^{3}$ cm^{-3}, high enough for molecules to be collisionally excited and observed. To date, molecular line observations conducted towards the Musca molecular cloud are limited to CO and its isotopologues, and NH_3[12–15], which is however only observed towards the densest core of Musca. The number densities required to excite CO and NH_3 lines are $\sim 10^2$ and 10^3 cm^{-3} respectively[17] which are well within the densities reached in the simulation of the model of the cloud. In contrast, in order to reproduce the observed column density in any filament-like simulation, the number density has to be of the order of $\sim 5 \cdot 10^{4}$ cm^{-3} or higher. If the 3D shape of Musca was that of a filament, strong NH_3 lines should be easily observed throughout the ridge of the dense structure, in contradiction to observations[15]. This could be further tested with radio observations of molecular lines with higher excitation densities (or higher transitions of the molecules mentioned above) or, better yet, with multiple transitions of the same molecule.

We validate our analysis and verify that Eq. (1) can be used to extract the correct cloud dimensions with a suite of simulations of clouds of different shapes. In all of our simulations, the dimensions of the simulated clouds are recovered by the normal-mode analysis with excellent precision. In contrast to the distribution of peaks seen in Fig. 2 (right panel), in cylindrical clouds ($L_y \ll L_x$) the first few peaks in the low spatial frequency part are all multiples of the first peak. These first few peaks are only due to the largest dimension of the cloud, resulting in a much more sparse distribution of peaks (see Extended Data Fig. 2). This is a quantitatively and qualitatively different behaviour than that seen in the Musca data (see Fig. 2), further strengthening the case that the intrinsic shape of Musca is sheet-like.

The determination of the 3D shape of clouds has been for decades a "holy grail" for interstellar medium physics and has been aggressively pursued through primarily statistical studies[18–25] which however, do not provide information on a cloud by cloud basis. Truly innovative methods previously proposed to access the true shape of regions inside clouds[26–27] have relied on complex chemical and/or radiative processes and thus their results depend on many assumptions. With our novel and robust result, Musca can become the largest laboratory to *a*) develop our theoretical models of star formation and molecular cloud evolution *b*) expand our knowledge on entire astronomical branches such as astrochemistry and the properties of interstellar dust grains and *c*) perform high-precision observational measurements. This discovery paves the way to unveil the 3D shape of any isolated cloud where associated striations have been observed in its low-density parts.

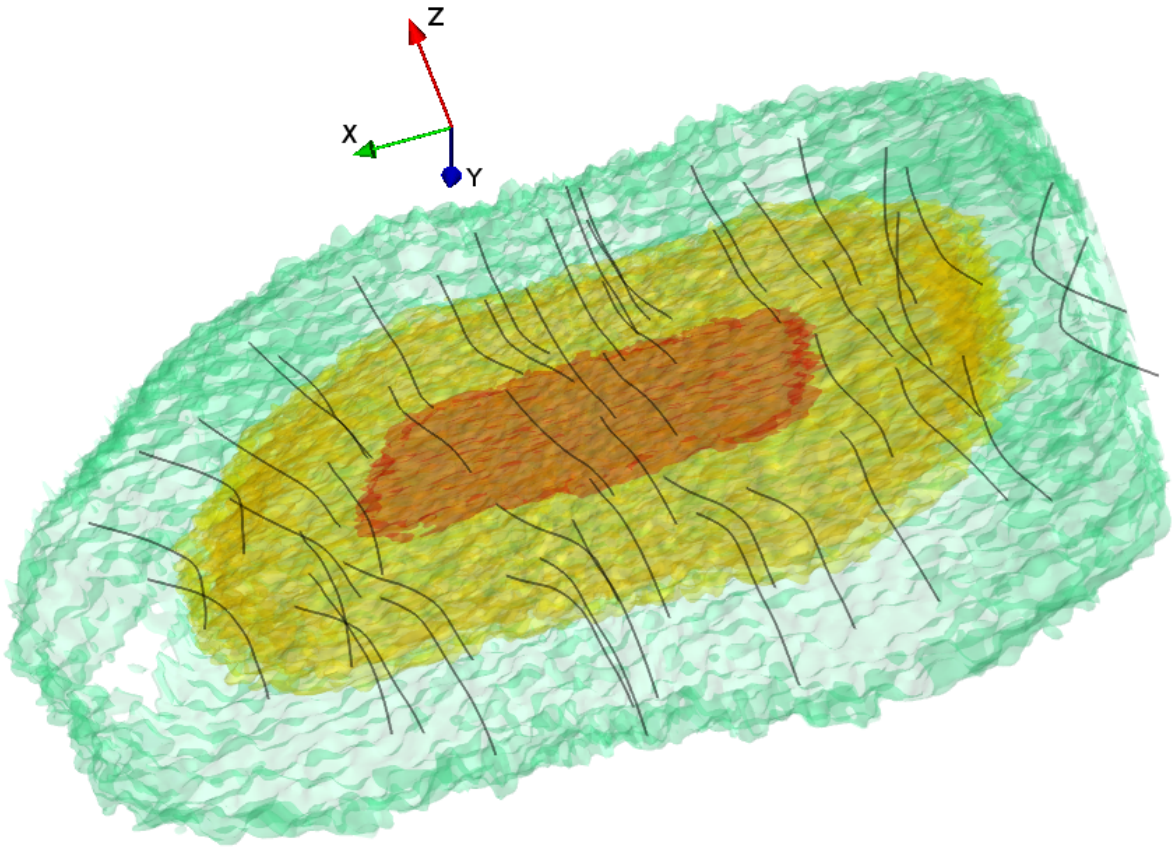

Figure 3 | 3D model of Musca molecular cloud The logarithm of volume density of Musca in 3D as this is reproduced from our MHD simulation. Density isosurfaces are set at 90%, 75%, 70% and 55% of the logarithm of the maximum number density. Black lines represent the magnetic field.

[1] Lada, C. J., Bergin, E. A., Alves, J. F., & Huard, T. L. The dynamical state of Barnard 68: a thermally supported, pulsating dark cloud. *Astrophys. J.*, **586**, 286-295 (2003)

[2] André, P., Di Francesco, J., Ward-Thompson, D., et al. From filamentary networks to dense cores in molecular clouds: toward a new paradigm for star formation. *Protostars and Planets VI*, 27-51 (2014)

[3] Goldsmith, P. F., Heyer, M., Narayanan, G., et al. Large-scale structure of the molecular gas in Taurus revealed by high linear dynamic range spectral line mapping. *Astrophys. J.*, **680**, 428-445 (2008)

[4] Miville-Deschênes, M.-A., Martin, P. G., Abergel, A., et al. Herschel-SPIRE observations of the Polaris flare: structure of the diffuse interstellar medium at the subparsec scale *Astron. Astrophys.*, **518**, L104 (2010)

[5] Alves de Oliveira, C., Schneider, N., Merín, B., et al. Herschel view of the large-scale structure in the Chamaeleon dark clouds. *Astron. Astrophys.*, **568**, A98 (2014)

[6] Palmeirim, P., André, P., Kirk, J., et al. Herschel view of the Taurus B211/3 filament and striations: evidence of filamentary growth? *Astron. Astrophys.*, **550**, A38 (2013)

[7] Cox, N. L. J., Arzoumanian, D., André, P., et al. Filamentary structure and magnetic field orientation in Musca. *Astron. Astrophys.*, **590**, A110 (2016)

[8] Malinen, J., Montier, L., Montillaud, J., et al. Matching dust emission structures and magnetic field in high-latitude cloud L1642: comparing Herschel and Planck maps. *Mon. Not. R. Astron. Soc.*, **460**, 1934-1945 (2016)

[9] Panopoulou, G. V., Psaradaki, I., & Tassis, K. The magnetic field and dust filaments in the Polaris Flare. *Mon. Not. R. Astron. Soc.*, **462**, 1517-1529 (2016)

[10] Tritsis, A., & Tassis, K. Striations in molecular clouds: streamers or MHD waves? *Mon. Not. R. Astron. Soc.*, **462**, 3602-3615 (2016)

[11] Knude, J., & Hog, E. Interstellar reddening from the HIPPARCOS and TYCHO catalogues. I. Distances to nearby molecular clouds and star forming regions. *Astron. Astrophys.*, **338**, 897-904 (1998)

[12] Arnal, E. M., Morras, R., & Rizzo, J. R. Multicolour polarization and CO observations towards a dark filament in Musca. *Mon. Not. R. Astron. Soc.*, **265**, 1 (1993)

[13] Kainulainen, J., Hacar, A., Alves, J., et al. Gravitational fragmentation caught in the act: the filamentary Musca molecular cloud. *Astron. Astrophys.*, **586**, A27 (2016)

[14] Hacar, A., Kainulainen, J., Tafalla, M., Beuther, H., & Alves, J. The Musca cloud: a 6 pc-long velocity-coherent, sonic filament. *Astron. Astrophys.*, **587**, A97 (2016)

[15] Machaieie, D. A., Vilas-Boas, J. W., Wuensche, C. A., et al. Properties of dense cores embedded in Musca derived from extinction maps and ^{13}CO, C^{18}O, and NH_3 emission lines. *Astrophys. J.*, **836**, 19 (2017)

[16] Planck Collaboration, Ade, P. A. R., Aghanim, N., et al. Planck intermediate results. XXXIII. Signature of the magnetic field geometry of interstellar filaments in dust polarization maps. *Astron. Astrophys.*, **586**, A136 (2016)

[17] Shirley, Y. L. The critical density and the effective excitation density of commonly observed molecular dense gas tracers. *Publications of the Astronomical Society of the Pacific*, **127**, 299 (2015)

[18] Myers, P. C., Fuller, G. A., Goodman, A. A., & Benson, P. J. Dense cores in dark clouds. VI - shapes. *Astrophys. J.*, **376**, 561-572 (1991)

[19] Ryden, B. S. The shapes of dense molecular cloud cores. *Bulletin of the American Astronomical Society*, **28**, 886 (1996)

[20] Curry, C. L. Shapes of molecular cloud cores and the filamentary mode of star formation. *Astrophys. J.*, **576**, 849-859 (2002)

[21] Jones, C. E., Basu, S., & Dubinski, J. Intrinsic shapes of molecular cloud cores. *Astrophys. J.*, **551**, 387-393 (2001)

[22] Jones, C. E., & Basu, S. The intrinsic shapes of molecular cloud fragments over a range of length scales. *Astrophys. J.*, **569**, 280-287 (2002)

[23] Goodwin, S. P., Ward-Thompson, D., & Whitworth, A. P. Why do starless cores appear more flattened than protostellar cores? *Mon. Not. R. Astron. Soc.*, **330**, 769-771 (2002)

[24] Tassis, K. The shapes of molecular cloud cores in Orion. *Mon. Not. R. Astron. Soc.*, **379**, L50-L54 (2007)

[25] Tassis, K., Dowell, C. D., Hildebrand, R. H., Kirby, L., & Vaillancourt, J. E. Statistical assessment of shapes and magnetic field orientations in molecular clouds through polarization observations. *Mon. Not. R. Astron. Soc.*, **399**, 1681-1693 (2009)

[26] Steinacker, J., Bacmann, A., Henning, T., Klessen, R., & Stickel, M. 3D continuum radiative transfer in complex dust configurations. II. 3D structure of the dense molecular cloud core ρ Oph D. *Astron. Astrophys.*, **434**, 167-180 (2005)

[27] Li, D., & Goldsmith, P. F. Is the Taurus B213 region a true filament?: observations of multiple cyanoacetylene transition. *Astrophys. J.*, **756**, 12 (2012)

Acknowledgements We thank V. Pavlidou, G. Panopoulou, V. Charmandaris, N. Kylafis, A. Zezas, E. Economou, J. Andrews, S. Williams, P. Sell, D. Blinov, I. Liodakis and T. Mouschovias for comments that helped improve this paper. The software used in

this work was in part developed by the DOE NNSA-ASC OASCR Flash Center at the University of Chicago. For post processing our results we partly used "yt" analysis toolkit[28]. 3D plots were created using "Mayavi2"[29]. K.T. and A.T. acknowledge support by FP7 through Marie Curie Career Integration Grant PCIG- GA-2011-293531 "SFOnset". A.T. and K.T. would like to acknowledge partial support from the EU FP7 Grant PIRSES-GA-2012-31578 "EuroCal". A.T. acknowledges funding from the European Research Council under the European Union's Seventh Framework Programme (FP/2007-2013)/ERC Grant Agreement n. 617001. This research has used data from the Herschel Gould Belt Survey (HGBS) project (`http://gouldbelt-herschel.cea.fr`). Usage of the Metropolis HPC Facility at the CCQCN of the University of Crete, supported by the European Union Seventh Framework Programme (FP7-REGPOT-2012-2013-1) under grant agreement no. 316165, is also acknowledged.

Author Contributions A.T. performed the numerical simulations, the analysis of the observations and wrote the text. K.T. contributed with the interpretation of the results and the writing of the text.

Author Information Reprints and permissions information is available at www.nature.com/reprints. The authors declare no competing financial interests. Readers are welcome to comment on the online version of the paper. Correspondence and requests for materials should be addressed to A.T. (tritsis@physics.uoc.gr).

1 Methods

Observations In the observations we define a cartesian coordinate system where the z axis is aligned with the long axis of the striations and thus the magnetic field, as this is probed by polarization measurements[7], the y axis is parallel to the line-of-sight (LOS), and the x axis is perpendicular to the striations on the plane-of-the-sky (POS). For deriving the normal modes we select a region south of the main filamentary structure (green rectangle in Fig. 1) and consider cuts along the x axis. Gravity and other effects such as shocks resulting from the collapse will impact the structure of regions adjacent to the dense filament. For this reason, the green region has been selected based on three criteria: *a*) it is as far away from the dense filamentary structure as possible so that additional forces can be ignored compared to the effect of MHD waves *b*) it has the largest possible length so that we can retrieve all spatial frequencies and *c*) the cuts are perpendicular to striations throughout, so that small variations in the orientation angle of striations do not affect our results. In order to increase the signal-to-noise ratio in our analysis we average the intensity of z pixel values in every three adjacent cuts along the x direction. We then compute the spatial power spectrum of each averaged cut using the Lomb-Scargle periodogram technique[30–31]. We have verified that increasing the size of the region, selecting a region north of the main filamentary structure and the uncertainties in the orientation of striations results in only small variations in the derived dimensions. The uncer-

tainty in the derived dimensions and in the analytically predicted normal modes is calculated from the uncertainty in the spatial frequencies of the first two peaks through error propagation. For the uncertainty of these spatial frequencies we take the standard deviations of the points comprising each of the first two peaks. The adopted distance of Musca in our analysis is 150 parsecs[11]. Earlier estimates placed Musca at 200 parsecs[32]. Adopting this larger estimate has no effect on the quality of the fitting of normal modes from Eq. (1) since this only depends on the relative distance between peaks. However, because angular size translates to a different physical scale the derived dimensions change to $L_x = 10.4 \pm 0.4$ and $L_y = 8.3 \pm 0.2$ parsecs.

More disk-like rather than triaxial oblate clouds should exhibit normal modes given by:

$$k_{mn} = \frac{j_{mn}}{R} \qquad (2)$$

where R is a mean radius and j_{mn} are the roots of the derivative of the Bessel function of first kind. In the case of Musca, unlike Eq. (1), Eq. (2) fails to fit the observed modes, thus suggesting a more triaxial shape.

Simulations We have used the astrophysical code FLASH 4.4[33–34] to perform three dimensional, ideal MHD simulations with self-gravity in Cartesian coordinates. To solve the equations of ideal MHD we use the unsplit staggered mesh algorithm[35]. This scheme has distinct advantages over truncation-error methods and $\nabla \cdot \vec{B} = 0$ is satisfied at all times to machine precision. In the interest of reducing computational expenses and since we are not interested in the fragmentation of any dense structures created within the cloud we use the standard FLASH multipole algorithm to solve Poisson's equation. To account for all waves that can arise in the MHD equations we use Roe's solver for the Riemann problem. To minimize numerical diffusivity we use van Leer's flux limiter and third order interpolation. Since Musca is an isolated cloud, we model it as such by forcing normal velocity components to zero in guard cells. This is achieved by setting all boundary types to diode, i.e. non-reflective type of boundaries. Thus, our choice ensures that any reflection of waves occurs at boundaries naturally created due to the contraction of the cloud and not at the edges of our simulation box. Finally, diode boundary conditions ensure there is no mass influx during the evolution of our simulations. All simulations have been performed on a fixed resolution grid with 256×256×256 cells.

In our simulations we again define a Cartesian coordinate system such that the direction of the ordered field is along the z direction and y represents the LOS dimension. Through the Chandrasekhar-Fermi method[36] and its more updated interpretation[37], the ordered value of the POS magnetic field towards the Musca molecular cloud has been observationally determined to be 12 ± 5 and 27 ± 11 μG respectively[38]. The number density value assumed in these estimates is 100 cm^{-3}. Here, we adopt a conservative value of 7 μG as an initial condition for our simulations which is within observational limits. In all simulations, we additionally introduce a perturbation in the x and y components of

the magnetic field as:

$$B_x(z) = B_y(z) = \delta B - \delta B sin(k_z z) \qquad (3)$$

where $k_z = \pi / L_z$ and δB was set equal to 10% of the value of the unperturbed field. This setup implies an Alfvén wave passing through the computational box with wavelength twice the size of the z direction. A constant temperature of 14 K is used in all simulations. Random perturbations with maximum amplitude 40% that of the background value are introduced in density and thermal pressure in a self-consistent manner such that isothermality is never violated. All velocity components are initially set to zero in all simulations.

3D model of Musca The initial number density in our simulation of the model of Musca is set equal to 100 cm^{-3}. The dimensions of our simulation box are $\mathrm{L_x} = 10.0$, $\mathrm{L_y} = 8.0$ and $\mathrm{L_z} = 3.5$ parsecs. The x and y dimensions of the simulation box are thus higher than the values we have derived observationally. However, because of contraction due to self-gravity and pinching of the field lines, the region where fast magnetosonic waves are trapped is smaller than the simulation box.

In Extended Data Fig. 1 we show the normalized power spectra (left) and the histogram of the identified peaks (right) from striations in this 3D model of Musca. The derived $\mathrm{L_x}$ and $\mathrm{L_y}$ dimensions are 7.7 ± 0.1 and 5.6 ± 0.1 parsecs respectively, in agreement with the dimensions of the resonating region. Since the morphology of the dense structure is that of a rectangle with rounded edges (see Fig. 3), similar to the observations, Eq. (1) is a good fit only to large physical scales.

In Extended Data Fig. 2 we show the velocity of propagation of fast magnetosonic waves in a mid-plane along the y direction. Changes of magnetic field strength along the x direction due to pinching of field lines result in clear variations in the propagation speed and thus define boundaries where magnetosonic waves are reflected. In 3D the boundaries resemble a square bowl with rounded edges. The green rectangle in Extended Data Fig. 2 marks the region where we performed our normal-mode analysis, at a comparable distance from the main dense structure as in observations.

Benchmarking We have additionally performed a large number of numerical simulations considering various shapes and initial conditions for density, in order to benchmark our analysis. We demonstrate our results using a simulation of a filament-like structure which however does not match Musca. The dimensions of the box of this filament simulation are $\mathrm{L_x} = 6.0$, $\mathrm{L_y} = 2.0$ and $\mathrm{L_z} = 2.0$ parsecs and the unperturbed value of density is set equal to 200 cm^{-3}. The column density map as well as the normalized power spectra are shown in top and bottom panels of Extended Data Fig. 3 respectively. All peaks are due to and can be fitted by the largest dimension of the cloud alone, since the modes from the shortest direction lie at much higher spatial frequencies ($\mathrm{k} > 6$). Thus, all the peaks shown in the bottom panel of Extended Data Fig. 3 correspond to $\mathrm{m} = 0$ in Eq. (1). The normal-mode analysis of striations in the simulation yields $\mathrm{L_x} = 4.2 \pm 0.1$ parsecs and

$L_y \ll L_x$, again in agreement with the size of the resonating region. No normal modes could be retrieved in simulations of a more precisely cylindrical cloud (not shown). Due to fragmentation at its rims[39–40], pronounced overdensities are also created at the edges of vertical cuts to the striations which leads to leakage instead of trapping of waves. None of our cylindrical-like simulations could match observations qualitatively or quantitatively.

[28] Turk, M. J., Smith, B. D., Oishi, J. S., et al. *Astrophys. J.*, **192** (suppl.), 9 (2011)

[29] Ramachandran, P., & Varoquaux, G. Mayavi2: 3D scientific data visualization and plotting. *Astrophysics Source Code Library*, 1205.008 (2012)

[30] Scargle, J. D., Studies in astronomical time series analysis. II - statistical aspects of spectral analysis of unevenly spaced data. *Astrophys. J.*, **263**, 835-853 (1982)

[31] Townsend, R. H. D. Fast calculation of the Lomb-Scargle periodogram using graphics processing units. *Astrophys. J.*, **191** (suppl.), 247-253 (2010)

[32] Gregorio Hetem, J. C., Sanzovo, G. C., & Lepine, J. R. D. Star counts and IRAS sources in southern dark clouds *Astron. Astrophys.*, **76** (suppl.), 347-363 (1988)

[33] Fryxell, B., Olson, K., Ricker, P., et al. FLASH: an adaptive mesh hydrodynamics code for modeling astrophysical thermonuclear flashes. *Astrophys. J.*, **131** (suppl.), 273-334 (2000)

[34] Dubey, A., Fisher, R., Graziani, C., et al. Challenges of extreme computing using the FLASH code. *Numerical Modeling of Space Plasma Flows*, **385**, 145 (2008)

[35] Lee, D. A solution accurate, efficient and stable unsplit staggered mesh scheme for three dimensional magnetohydrodynamics. *Journal of Computational Physics*, **243**, 269-292 (2013)

[36] Chandrasekhar, S., & Fermi, E. Magnetic fields in spiral arms. *Astrophys. J.*, **118**, 113 (1953)

[37] Hildebrand, R. H., Kirby, L., Dotson, J. L., Houde, M., & Vaillancourt, J. E. Dispersion of magnetic fields in molecular clouds. I. *Astrophys. J.*, **696**, 567-573 (2009)

[38] Planck Collaboration, Ade, P. A. R., Aghanim, N., et al. Planck intermediate results. XXXV. Probing the role of the magnetic field in the formation of structure in molecular clouds. *Astron. Astrophys.*, **586**, A138 (2016)

[39] Pon, A., Johnstone, D., & Heitsch, F. Modes of star formation in finite molecular clouds. *Astrophys. J.*, **740**, 88 (2011)

[40] Clarke, S. D., & Whitworth, A. P. Investigating the global collapse of filaments using smoothed particle hydrodynamics. *Mon. Not. R. Astron. Soc.*, **449**, 1819-1825 (2015)

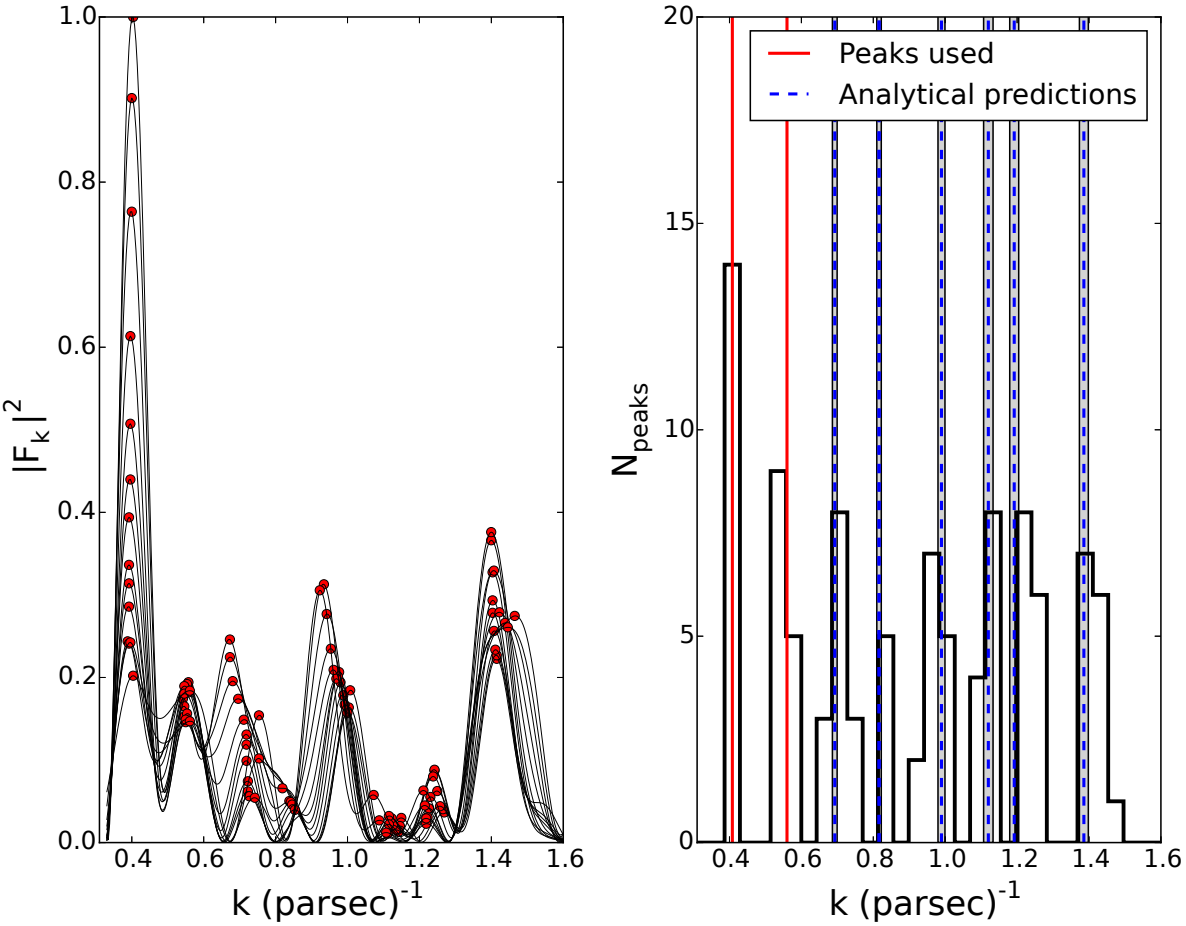

Extended Data Figure 1 | Normal modes in simulated cloud Left and right panels are the same as Fig. 2 but from our numerical simulation of the 3D model of the cloud.

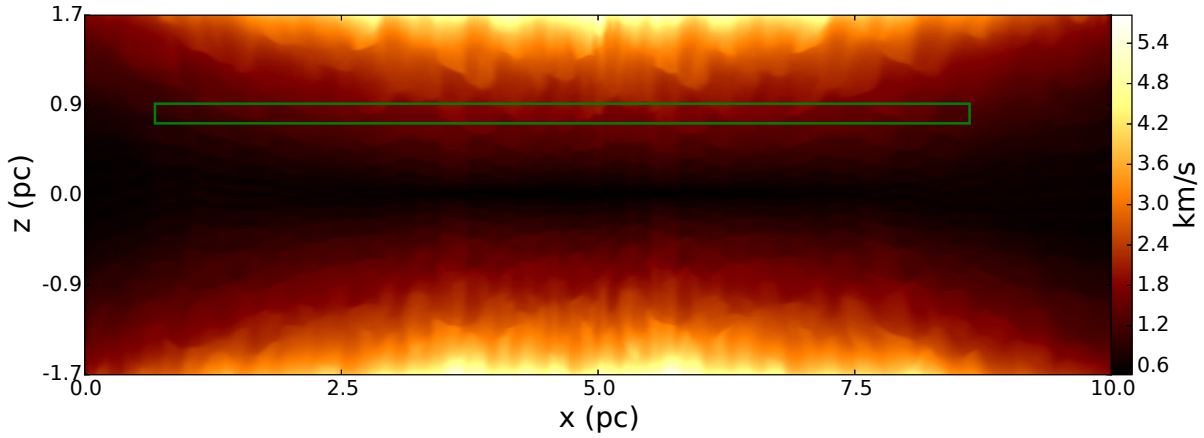

Extended Data Figure 2 | Boundaries formed in the simulated cloud Mid-plane map (along the y direction) of the propagation speed of fast magnetosonic waves. The propagation speed is clearly higher above and below the main body of the cloud compared to the edges. The green rectangle marks the region where we take cuts perpendicular to the striations and perform our analysis.

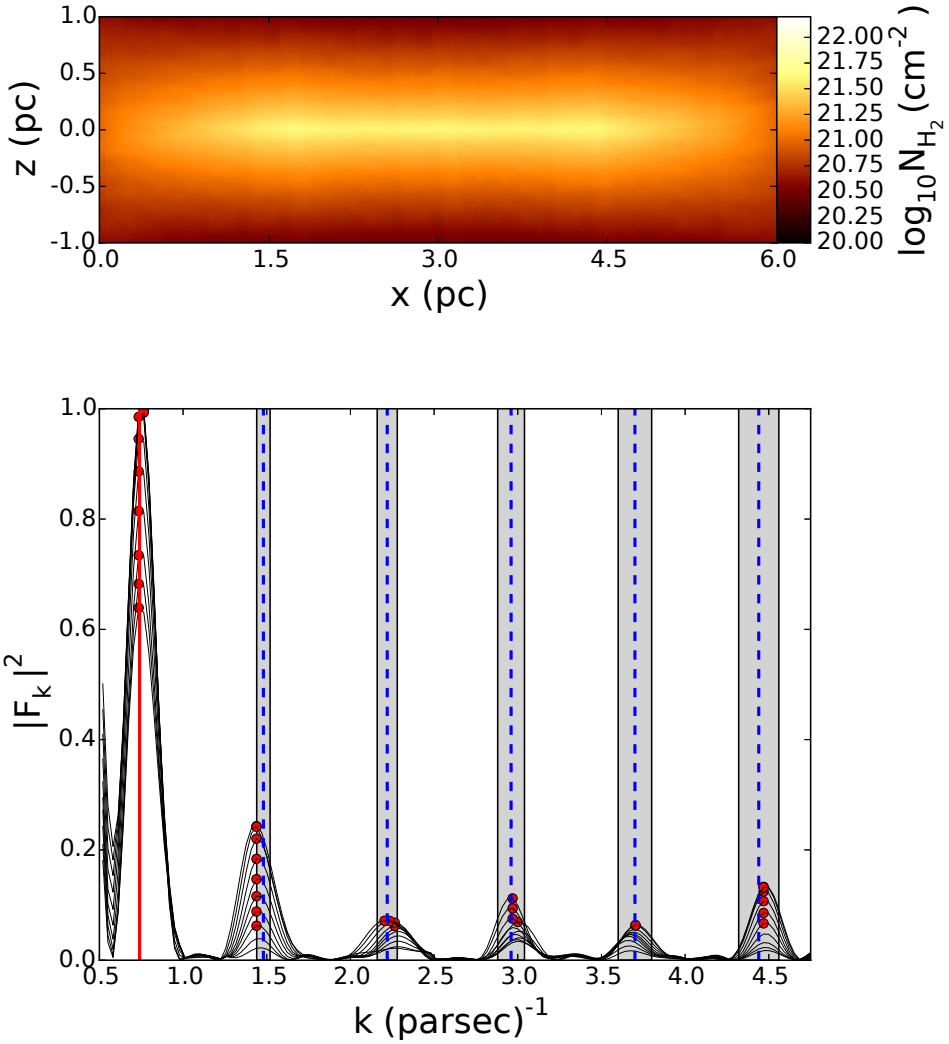

Extended Data Figure 3 | Normal modes in a cylindrical simulated cloud Upper panel: column density map from our MHD simulations considering a filamentary/ribbon-like morphology. Lower panel: Power spectra of the cuts perpendicular to the striations considering this morphology. The solid red and dashed blue lines and the shaded regions are defined in the same manner as in Fig. 2.

Chapter 4

The structure of prestellar cores

Observations have shown that the majority of dense prestellar cores lie within filaments (Men'shchikov et al. 2010; Konyves et al. 2015). However, how prestellar cores are formed and the role that magnetic fields have in their evolution is still a topic of hot debate. In a magnetically driven core formation scenario prestellar cores are expected to have oblate shapes (Basu & Ciolek 2004; Ciolek & Basu 2006) and magnetic field lines are expected to have an hourglass morphology and to be aligned with the minor axis of symmetry of the core (see Chapman et al. 2013 for an observational survey on single protostellar cores). Of central importance in distinguishing between opposing star formation theories is the relation between magnetic-field strength (B) and gas density (ρ) in contracting prestellar cores ($B \propto \rho^{\kappa}$). Bayesian statistical modelling of magnetic field strength measurements through the Zeeman effect (including detections and nondetections) from a large sample of cores have yielded a value for the exponent κ equal to 2/3. However, this value can only be realized if the shapes of cores are spherical, a scenario not favoured neither by observations nor by theoretical arguments. We have traced the inconsistency to simplifying assumptions and especially to an underestimation of density uncertainties and show that the available data do not support $\kappa = 2/3$. Additionally, we have analysed projected shapes of cores from the same sample. Our results show that the shapes of the cores also do not reconcile $\kappa = 2/3$ but are instead consistent with an ensemble of oblate cores projected randomly on the plane-of-the-sky. Our results add to a body of evidence supporting that the evolution of individual cores is controlled by magnetic fields (Mouschovias & Ciolek 1999).

Mon. Not. R. Astron. Soc. **000**, 000–000 (0000) Printed 22 May 2015 (MN LATEX style file v2.2)

Magnetic Field – Gas Density Relation and Observational Implications Revisited

A. Tritsis[1], G. V. Panopoulou[1], T. Ch. Mouschovias[3], K. Tassis[1,2], V. Pavlidou[1,2]
[1] *Department of Physics, University of Crete, PO Box 2208, 71003 Heraklion, Greece*
[2] *IESL, Foundation for Research and Technology-Hellas, PO Box 1527, 71110 Heraklion, Crete, Greece*
[3] *Departments of Physics and Astronomy, University of Illinois at Urbana-Champaign, 1002 W. Green Street, Urbana, IL 61801*

22 May 2015

ABSTRACT

We revisit the relation between magnetic-field strength (B) and gas density (ρ) for contracting interstellar clouds and fragments (or, cores), which is central in observationally determining the dynamical importance of magnetic fields in cloud evolution and star formation. Recently, it has been claimed that a relation $B \propto \rho^{2/3}$ is statistically preferred over $B \propto \rho^{1/2}$ in molecular clouds, when magnetic field detections and nondetections from Zeeman observations are combined. This finding has unique observational implications on cloud and core geometry: The relation $B \propto \rho^{2/3}$ can only be realized under spherical contraction. However, no indication of spherical geometry can be found for the objects used in the original statistical analysis of the $B-\rho$ relation. We trace the origin of the inconsistency to simplifying assumptions in the statistical model used to arrive at the $B \propto \rho^{2/3}$ conclusion and to an underestimate of observational uncertainties in the determination of cloud and core densities. We show that, when these restrictive assumptions are relaxed, $B \propto \rho^{1/2}$ is the preferred relation for the (self-gravitating) molecular-cloud data, as theoretically predicted four decades ago.

Key words: diffusion – ISM: magnetic fields – ISM: clouds – MHD – stars: formation – methods: statistical

1 INTRODUCTION

Whether interstellar magnetic fields play a role in the formation of clouds and stars or are affected by cloud and/or star formation are old questions that predate the discovery of molecular clouds. Mestel & Spitzer (1956) were concerned that the estimated very high electrical conductivity of the interstellar gas implies that the magnetic flux is frozen in the matter and, in the then prevailing picture of star formation (Hoyle's spherical collapse and hierarchical fragmentation), magnetic fields would prevent fragmentation and star formation. For this reason, they suggested that ambipolar diffusion (the motion of electrons and ions together with magnetic flux relative to the neutrals) would set in at some stage and allow a cloud to reduce its magnetic flux and thereby fragment and collapse to form stars.

The first testable prediction of magnetic-field strengths in clouds destined to form stars was given by Mestel (1965). A cloud collapsing spherically and isotropically while conserving its mass (M) and magnetic flux (Φ_B) implies a relation between the magnetic-field strength and gas density: $M \propto \rho R^3 = const$, $\Phi_B \propto BR^2 = const'$. Hence, eliminating the cloud radius R in favor of the density ρ from the two conservation laws yields a scaling between the field strength B and the density: $B \propto \rho^{2/3}$.

Verschuur (1969) summarized the results of Zeeman measurements of the field strength in nine HI clouds on a $\log(B)$ – $\log(n)$ plot, where n is the number density (particles/cm^3) and concluded, as did other workers, that the measurements were in agreement with that theoretical prediction – without, however, performing an actual fit to those data.

Mouschovias (1976a, b) provided the first self-consistent formulation and solution of the problem of the equilibrium of self-gravitating, isothermal, magnetic clouds embedded in a hot and tenuous intercloud medium. He also considered the implication of the contraction of such clouds (or fragments) on the $B-\rho$ relation. In the deep interior of *each* cloud, he found that the ratio of magnetic and gas pressures, $\alpha \equiv B^2/8\pi P$, tends to remain constant during contraction. In fact, it tends to retain a value near unity. For isothermal contraction, $P = \rho_{\rm n} C^2$, where $C = (k_{\rm B}T/\bar{m})^{1/2}$ is the isothermal speed of sound at temperature T and mean mass per particle $\bar{m}$; the quantity $k_{\rm B}$ is Boltzmann's constant. Hence, Mouschovias' result $\alpha \approx 1$, specialized to isothermal contraction, yields $B \propto \rho^{1/2}$. For an equation of state $P \propto \rho^{\gamma}$, the relation between B and ρ becomes $B \propto \rho^{\gamma/2}$ (see review by Mouschovias 1991b). An analysis by Crutcher (1999) of a larger sample of clouds than that used by Verschuur, with measured magnetic-field strengths and number densities (greater than

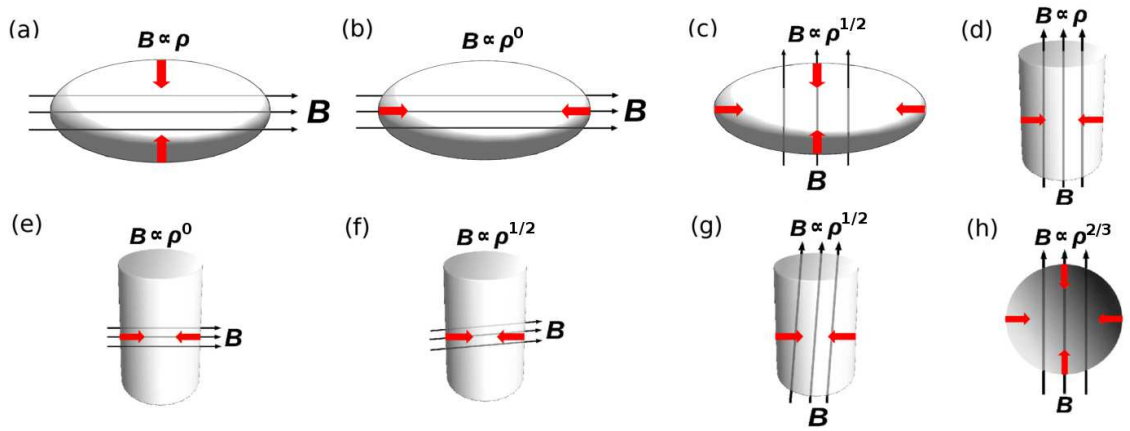

Figure 1. Different geometries of contracting clouds and magnetic fields examined in §2.1. Black arrows represent the direction of the magnetic field and bold red arrows the direction of contraction. The $B \propto \rho^{2/3}$ relation is uniquely associated with spherical contraction and, therefore, has unique observational implications.

100 cm^{-3}), found a best-fit exponent of 0.47 for the $B-\rho$ scaling, in agreement with the theoretical prediction. Detailed numerical simulations by Fiedler & Mouschovias (1992, 1993) predicted a slope $\kappa = 0.47$ for contracting cores formed by gravitationally-driven ambipolar diffusion and evolving from initially magnetically subcritical to supercritical states. More recently, Li et al. (2015) inferred $\kappa = 0.41$ from observations in the massive star forming region NGC 6334. For lower densities, although the theoretical prediction for an evolving cloud was $\kappa \approx 0$ (because self-gravity is not strong enough to compress the cloud perpendicular to the field lines), the observational picture has generally been less clear, with various scaling exponents derived empirically (see Vallée 1997 and references therein; Marchwinski 2012) for sets of clouds observed at the same time.

Crutcher et al. (2010, hereinafter referred to as CWHFT10) revisited the scaling between B and ρ for a yet larger sample of both low-density (primarily HI) and high-density (primarily molecular) clouds. They used a Bayesian statistical analysis that allowed them to treat nondetections and varying angles between the magnetic field and the line of sight, and they optimized a family of models consisting of a uniform distribution of magnetic-field values between some minimum and maximum, with the maximum having two distinct branches in its behavior (on a log$B$ – logρ plot): a flat part at low densities (B independent of ρ), and a power-law scaling at higher densities ($B \propto \rho^{\kappa}$), with the exponent κ, the break density ρ_0, and the width of the magnetic-field strength distribution being the free parameters of their model. Their conclusion was that the data prefer $\kappa \approx 2/3$ and reject $\kappa \approx 1/2$. They took this result to be an indication of "isotropic contraction of gas too weakly magnetized for the magnetic field to affect the morphology of the collapse."

In this work, we examine more closely the observational implications of different geometries of contraction on the $B-\rho$ relation. The distribution of forces in a cloud determines its evolution, including its geometric shape and the associated $B-\rho$ relation. Although a given (or observed) $B-\rho$ relation does not necessarily imply a unique geometric shape of a cloud, it is nevertheless the case that a given (or observed) $B-\rho$ relation can only be found in a very restricted set of geometric shapes, which in turn restrict the kind of motions capable of producing those shapes and the $B-\rho$ relation. Here, we test whether the observed shapes of the objects (clouds and cores) on which the latest $B-\rho$ relation study (that of CWHFT10) has been based are consistent with the underlying geometries in which the claimed scaling ($B \propto \rho^{2/3}$) could develop.

In §2.1 we summarize the $B-\rho$ relations implied by different cloud geometries that could be established by the evolution of molecular clouds with frozen-in magnetic fields (no significant ambipolar diffusion). Density maps of clouds and cores used in CWHFT10 are examined in §2.2, testing for consistency between geometry and the exponent κ. The value $\kappa = 2/3$ claimed by CWHFT10 cannot be reconciled with the observed cloud shapes. The source of the discrepancy lies in various assumptions of the CWHFT10 analysis, as we show in §3. Relaxing the problematic assumptions, we reconcile the observed shapes and the $B-\rho$ relation in §4, and we show that the value $\kappa = 1/2$ is preferred by the data over the value $\kappa = 2/3$. We summarize the conclusions in §5.

2 CLOUD GEOMETRY AND THE $B-\rho$ RELATION

In this section we address the connection between the slope of the $B-\rho$ relation and the cloud geometry. First, in §2.1, we investigate theoretically the $B-\rho$ relation implied by different geometries of clouds and magnetic fields. Then, in §2.2, we examine the shapes of objects in the CWHFT10 sample and whether they are consistent with the claimed slope $\kappa = 2/3$.

2.1 $B-\rho$ Relations Implied by Different Geometries

2.1.1 Disklike or Slab Cloud with $\boldsymbol{B}$ *in the Plane of the Disk*

We first consider an oblate (disklike) cloud of half-thickness Z_0 and arbitrarily large radius R_0, uniform density ρ_0, threaded by a uniform magnetic field B_0 in the plane of the disk (see Fig. 1a). A slab-shaped cloud is a special case of this. Contraction perpendicular to the plane of the disk to a new half-thickness Z increases the density and the magnetic field by the same factor, Z_0/Z; hence, $B \propto \rho$. One should note that, for this kind of contraction, the gravitational force per unit mass perpendicular to the plane of the disk on a fluid element initially at z depends only on the column density ρz, which does not change upon contraction. However, the magnetic-pressure force per unit mass on that

same fluid element, $|-\boldsymbol{\nabla}B^2/8\pi|/\rho$, increases upon contraction as $(Z_0/Z)^2$. Consequently, even if such contraction sets in for some reason, magnetic forces will eventually stop it.

We now consider the same oblate cloud, threaded by the same magnetic field, but now the cloud is allowed to contract only along the field lines (see Fig. 1b); i.e., the half-thickness (or polar radius) Z_0 does not change, but the local extent of the cloud along field lines ($\propto R_0 \cos\theta$, where θ is the angle between the field lines and a line from the cloud's centre to the point of interest on the rim of the cloud) decreases such that the density increases uniformly in the cloud model. The ultimately resulting shape is in general one of a prolate, triaxial object, a "filament" perpendicular to the field lines. The motions that created this filamentary cloud do not by themselves change the strength of the magnetic field; hence, $B \propto \rho^0$, i.e., B is independent of ρ. However, the increased density in the filamentary structure implies a stronger gravitational field *along* the filament, toward the centre of the original oblate cloud. *Will this filament fragment along its length to form at least one more-or-less spherical core?*

If this filament contracts as a whole along its length, an argument similar to the one in Mouschovias (1976b) shows that the magnetic-tension force near the ends of the filament increases more rapidly than the gravitational force, so such contraction (perpendicular to the field lines) can more easily take place in the central part of the filament. If a fragment (or core) is to separate out and contract gravitationally in this region, its mass-to-flux ratio must exceed the critical value for collapse,

$$\mu_{\rm cr} \equiv \left(\frac{M}{\Phi_{\rm B}}\right)_{\rm cr} = \left(\frac{\sigma}{B}\right)_{\rm cr} \approx \frac{1}{\sqrt{63G}} \qquad (1)$$

(Mouschovias & Spitzer 1976). The quantity σ is the column density along field lines (in g cm^{-2}), and B is the magnetic field strength. (The constant on the right-hand side of eq. [1] has a slight dependence on the geometry of the cloud.) If the original size of the cloud, both parallel and perpendicular to the field lines, is very large, then the resulting filament will also be very long, and it is possible for several fragments to separate out along its length, provided that criterion (1) is satisfied for each. The thermal critical mass per unit length of a filament, $2C^2/G$ (Ostriker 1964), is not a relevant quantity for the fragmentation of a filament threaded by a magnetic field perpendicular to its long dimension. For each fragment, $B \propto \rho^{1/2}$ for as long as the magnetic field remains frozen in the matter. Detailed numerical simulations (Fiedler & Mouschovias 1992, 1993) showed that ambipolar diffusion sets in in the interiors of initially subcritical molecular clouds and leads to an increase in the mass-to-flux ratio toward its critical value for collapse (see eq. [1]). Prior to establishment of critical conditions, the magnetic-field strength increases by at most 30% while the density can increase by a very large factor; hence, $\kappa \approx 0$. After the mass-to-flux ratio reaches its critical value, contraction accelerates and proceeds with balance of forces along field lines and as rapidly as magnetic forces allow perpendicular to the field lines. These are the sufficient conditions for establishment of the relation $B \propto \rho^{\kappa}$ with $\kappa = 1/2$. (Actually, the numerical simulations show that $\kappa = 0.47$, meaning that flux-freezing is not perfect; some ambipolar diffusion takes place even during the dynamical stage of contraction – see Fiedler & Mouschovias 1993, Fig. 9c.)

2.1.2 Disklike or Slab Cloud with $\boldsymbol{B}$ Perpendicular to the Plane of the Disk

We now consider the same disklike cloud, threaded by the same magnetic field as above, but now the field is perpendicular to the plane of the disk (see Fig. 1c), with field lines "fanning out" outside the cloud, acquiring a characteristic hour-glass shape (not shown in Fig. 1c because it is not essential for the present purposes). Such oblate clouds are unavoidable if they form out of lower-density interstellar gas in which the magnetic field has an ordered component and, locally, the magnetic force is nonnegligible relative to the gravitational force. The $B \propto \rho^{1/2}$ relation implied by the gravitational, isothermal contraction of such a cloud (both along and perpendicular to the field lines) as well as its physical origin were described above in the *Introduction* and at the end of the preceding subsection and they need not be repeated here. Fragments can separate out in the interior of the cloud and contract dynamically if their mass-to-flux ratio exceeds the critical value for collapse given by equation (1). A magnetically subcritical cloud can reach critical conditions because of gravitationally-driven ambipolar diffusion, whose modern understanding is that it redistributes mass in the central flux tubes of molecular clouds, where the degree of ionization is relatively small ($< 10^{-7}$), but it does not lead to flux loss by a cloud as a whole (Mouschovias 1979).

2.1.3 Cylindrical or Filamentary Cloud with $\boldsymbol{B}$ Along the Cylinder

Cylindrical model clouds threaded by a magnetic field along the axis of symmetry of the cylinder (see Fig. 1d) were studied exhaustively by Mouschovias & Morton (1991, 1992a, 1992b). During lateral contraction (perpendicular to the symmetry axis and the magnetic field), both the instantaneous density ρ and magnetic-field strength B of a fluid element at instantaneous cylindrical polar radius r increase as $1/r^2$; hence, $B \propto \rho$. The gravitational force per unit mass at the position of the fluid element increases as $1/r$, while the magnetic force per unit mass increases as $1/r^3$. Consequently, the magnetic forces will stop such contraction at some stage. There is neither a critical mass per unit length nor a critical mass-to-flux ratio per unit length for such self-gravitating filaments to suffer collapse (see Mouschovias & Morton 1991, discussion following eq. [38]). The evolution of such model clouds was followed numerically by Mouschovias & Morton (1992a, b); the density quickly acquires a spatial profile approximated by $1/r^2$.

2.1.4 Cylindrical or Filamentary Cloud with $\boldsymbol{B}$ Perpendicular to the Cylinder

The case in which the magnetic field is perpendicular to the axis of the cylinder (Fig. 1e) is similar to the one discussed in §2.1.1 above – the object that started as an oblate (disklike) cloud threaded by a magnetic field in the plane of the disk and then contracted primarily along the field lines to acquire a triaxial, prolate shape perpendicular to the field lines.

2.1.5 Cylindrical or Filamentary Cloud with $\boldsymbol{B}$ at an Angle with respect to the Cylinder

If the magnetic field is at an angle with respect to the axis of the cylindrical cloud, one might think that its component along the axis would ensure that there is no critical mass or mass-to-flux ratio for lateral collapse, while its component perpendicular to the axis would bring in the Mouschovias & Spitzer (1976) critical mass-to-flux ratio for collapse and/or fragmentation of the cloud in both directions. Then the longitudinal component of $\boldsymbol{B}$ would tend to increase as ρ, while the lateral component would tend to increase as $\rho^{1/2}$. Unfortunately, the effect of the magnetic field on the evolution of a cloud cannot be deduced correctly by considering separately the effect of each of its components and then superimposing the two results. To visualize the behavior of a prolate cloud threaded by a magnetic field at an angle with respect

to its length, we consider two cases: (a) $\boldsymbol{B}$ is almost perpendicular to the axis of the cylinder (see Fig. 1f), and (b) $\boldsymbol{B}$ is almost parallel to the axis (see Fig. 1g).

In case (a), motions along the field lines can, in principle, take place and make the extent of the cloud along $\boldsymbol{B}$ as small as thermal-pressure and/or turbulent-pressure forces allow. If only this evolution took place, B would be independent of ρ. However, for self-gravitating fragments (or cores) to form, destined to collapse and form stars, contraction *perpendicular* to the field lines has to take place as well. This brings in the critical mass-to-flux ratio given by equation (1), and the relation $B \propto \rho^{1/2}$ is established again.

In case (b), motions along field lines can transform the cylinder into an oblate (disklike) object or even break it up into several such oblate objects, with hardly affecting the magnetic-field strength. However, as we have already seen, for an oblate object to collapse its mass-to-flux ratio has to exceed the critical value. Evolution beyond that state results in the relation $B \propto \rho^{1/2}$. How the fragmentation of an initially critical magnetic flux tube affects the $B - \rho$ relation depends on the number of fragments that may form along the flux tube, and is discussed in detail in Mouschovias (1991c; see § 2.4 and Fig. 1 therein).

2.1.6 Spherical Cloud

The $B - \rho$ relation implied by spherical, isotropic contraction (Fig. 1h) was discussed in §1. The relation $B \propto \rho^{2/3}$ is unique among $B - \rho$ relations in that only spherical contraction can cause it. If contraction along field lines is more rapid than perpendicular to the field lines, the exponent κ in the relation $B \propto \rho^{\kappa}$ becomes less than 2/3. If the opposite is true, the exponent κ becomes greater than 2/3. Thus the recent claim by CWHFT10 that Zeeman and density observations, taken in aggregate, yield $B \propto \rho^{2/3}$ has unique, observationally testable implications on the shapes of the observed objects (clouds or cores): they *must* be spherical.

The severe constraint on the geometry that can produce the $B \propto \rho^{2/3}$ relation does not get relaxed by a random component of $\boldsymbol{B}$ dominating its ordered (or mean) component inside the observed object (cloud or core)[1] . While a completely random component of the magnetic field does not introduce a spatial anisotropy that would tend to destroy the spherical geometry and the $B \propto \rho^{2/3}$ relation, it does not enter the $B - \rho$ relation, and it also does not contribute to the observed line-of-sight B. The $B - \rho$ relation refers to the mean B, and Zeeman observations measure that field's component along the line of sight.

2.2 Observational Determination of CWHFT10 Cloud Shapes

The conclusion that the exponent $\kappa = 2/3$ requires spherical clouds and cores is difficult to reconcile with the CWHFT10 result at high densities. Although the shapes of molecular clouds and their fragments are an important part of the debate on the process that regulates cloud evolution and star formation, spherical clouds and cores are not a contender in either the theoretical or the observational arguments.

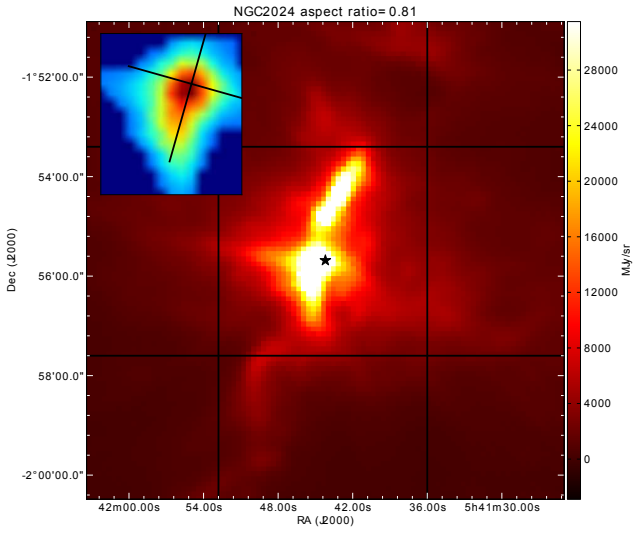

Figure 2. Archival *Herschel*-SPIRE 250μm dust continuum emission map of the core NGC2024. The star represents the coordinates of the core as reported by Falgarone et al (2008). The inset image is the outcome of our data processing and the black lines represent the principal axes of the core.

According to theory, if ambipolar diffusion is the agent mainly responsible for core formation, then the cores are expected to be flattened along the magnetic field because magnetic forces act only perpendicular to the field lines. Thus, the expected shapes are oblate (Mouschovias 1976b; Fiedler & Mouschovias 1993), although not necessarily axisymmetric (Basu & Ciolek 2004; Ciolek & Basu 2006; Kudoh & Basu 2011). If cores form as the result of converging turbulent flows (e.g., see review by Mac Low & Klessen 2004), then they are expected to have random, triaxial shapes, with a slight preference for prolateness (Gammie et al. 2003; Li et al. 2004). Predominantly spherical cores and clouds are not expected by any formation mechanism.

Observationally, the issue is how to distinguish between oblate and prolate intrinsic shapes from two-dimensional projections. Spherical clouds and cores are straightforward to spot even in projection: their two-dimensional projections are circles and the aspect ratio of the projected shapes is very sharply peaked at 1. Early work on core shapes, assuming axial symmetry, seemed to favour prolate cores (Myers et al. 1991; Ryden 1996). However, subsequent investigations which relaxed the axisymmetry assumption have consistently yielded triaxial, preferentially oblate core shapes (e.g., Jones, Basu & Dubinski 2001; Jones & Basu 2002; Goodwin, Ward-Thompson & Whitworth 2002), independently of tracer or core sample. Tassis (2007) and Tassis et al. (2009) found strong indications for triaxial, preferentially oblate cores. Spherical cores and clouds on the other hand are not common in nature.

However, it may still be possible that the molecular sample used in the CWHFT10 study does contain an unusually high fraction of spherical objects, which would be consistent with their finding of $B \propto \rho^{2/3}$. To test for this possibility, we have calcu-

[1] In any case, at core scales (smaller than about 0.1 pc), the magnetic field is both observed (e.g., Girart et al. 2006, Chapman et al. 2013) and theoretically expected (Mouschovias 1987a) to be dominated by an ordered component. The reason is that, because of magnetically-driven ambipolar diffusion, a random component of $\boldsymbol{B}$ cannot be sustained on scales smaller than the Alfvén length-scale, $\lambda_A = \pi v_A \tau_{\rm ni}$, where $v_A = B/(4\pi\rho)^{1/2}$ is the Alfvén speed in the neutrals, and $\tau_{\rm ni}$ is the slowing-down time of a neutral particle due to collisions with ions; for typical molecular clouds, $\lambda_A = 0.1$ pc (Mouschovias 1987a; 1991a). The timescale for straightening out field lines that are tangled on a scale l is proportional to l^2 and, for typical molecular cloud densities ($10^3\,{\rm cm}^{-3}$), magnetic fields ($30\,\mu$G), and core sizes (0.1 pc), is much smaller than the free-fall time. (e.g., see Mouschovias et al. 2011).

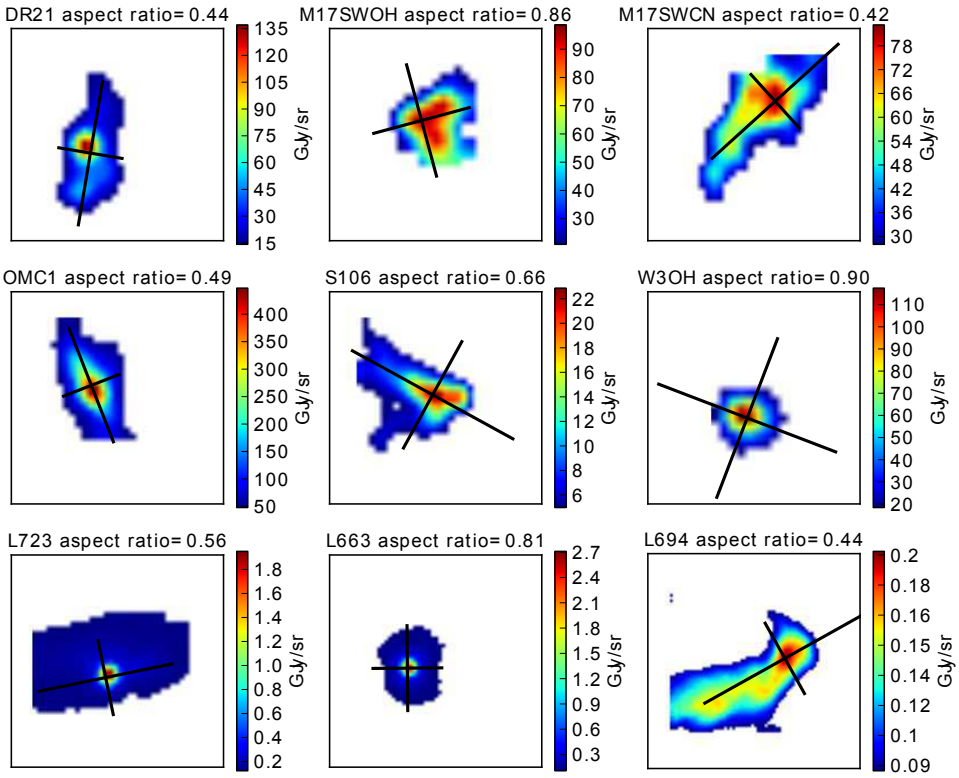

Figure 3. 250μm dust continuum emission maps from the *Herschel* Science Archive. Black lines represent the principal axes of the cores.

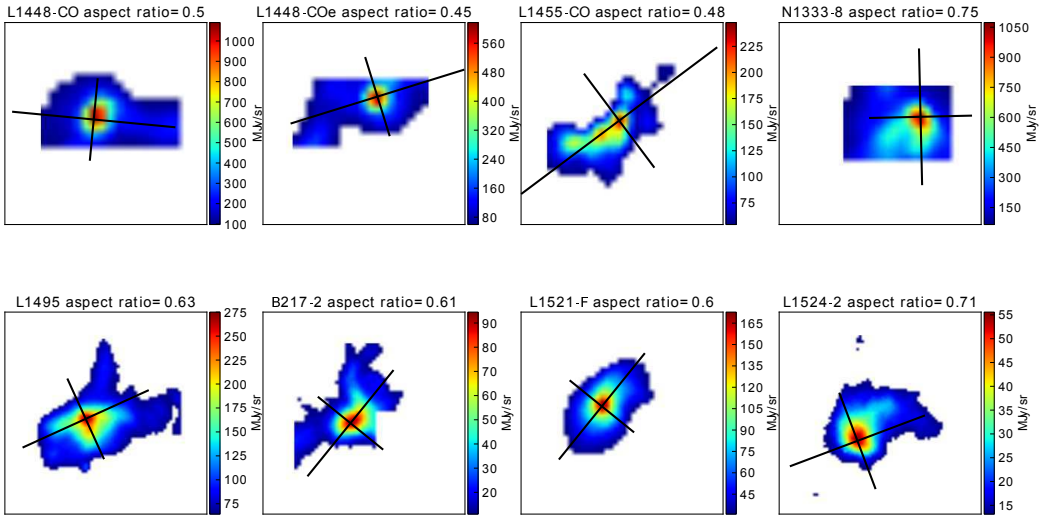

Figure 4. 500μm dust continuum emission maps from the *Herschel* Science Archive. Black lines represent the principal axes of the cores.

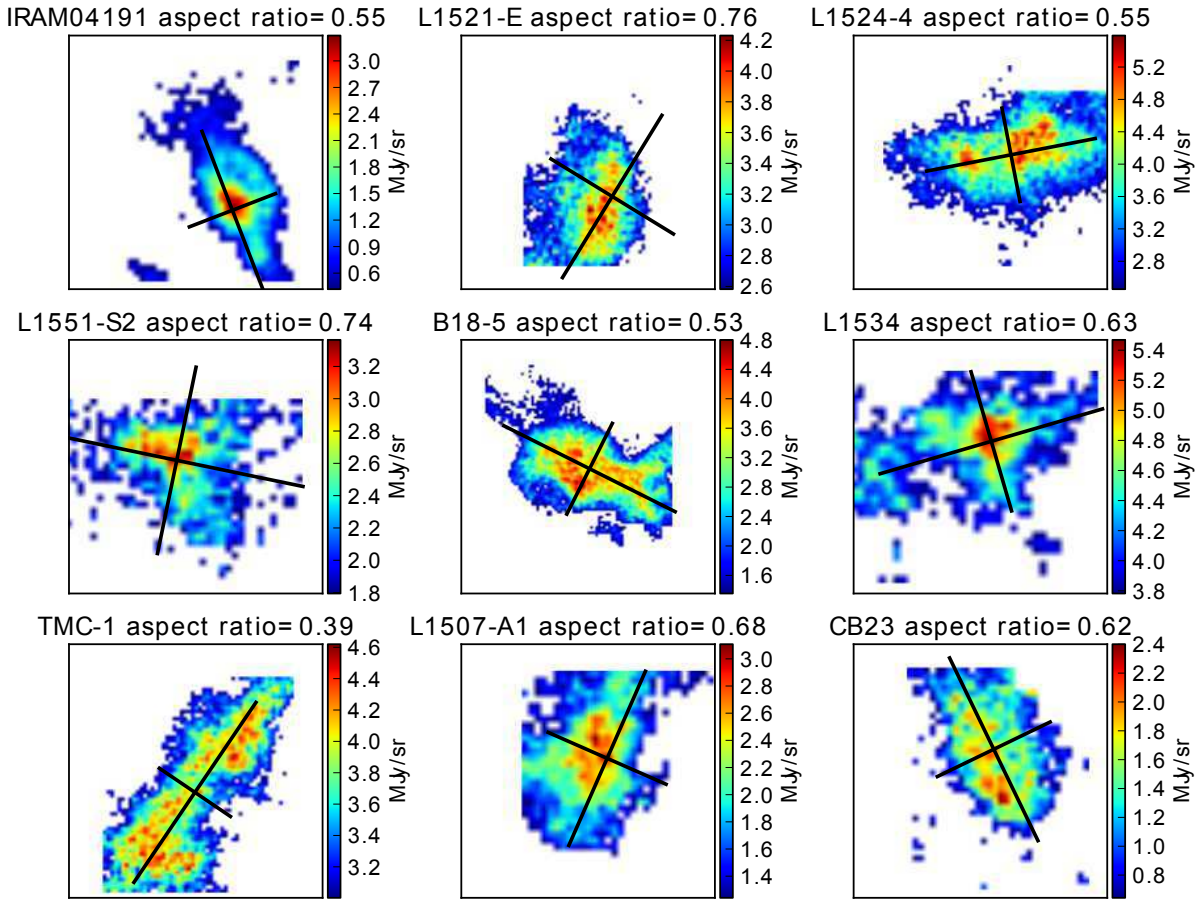

Figure 5. ^{13}CO line emission maps of the J=1-0 transition from the FCRAO survey. Black lines represent the principal axes of the cores.

lated aspect ratios of plane-of-the-sky maps for as many of the objects of CWHFT10 as we could find appropriate data.

We used dust continuum emission images from the online data archive of the *Herschel* Space Telescope (Pilbratt et al. 2010) observed with SPIRE at 250 μm and 500 μm to create maps of 18 of these objects, and ^{13}CO line emission data of the J=1-0 transition from the FCRAO survey of the Taurus molecular cloud (Goldsmith et al. 2008) for another 9 of them. The maps were centered on the coordinates given by Troland & Crutcher (2008) and Falgarone et al. (2008) as referenced by CWHFT10. The angular sizes of the maps were 3 to 4 times the typical sizes of cores. The method we used to calculate the aspect ratios is based on the first and second moment of the flux density and is described in detail by Tassis et al. (2009). In certain cases, cores, as projected on the plane of the sky, are closely spaced; for this reason, flux from a nearby core can severely affect the aspect ratio of the object under examination. To avoid this, we performed a visual inspection to select a region that contains only one core. Finally, in order to remove the background which can also affect the analysis, we set a threshold and calculated the aspect ratio only from the pixels whose intensity was greater than the mean intensity of the final region (e.g., see Fig. 2 and inset). The resulting maps of the cores, along with their principal axes and their aspect ratios, are presented in Figures 3 - 5.

Even visual inspection of these maps reveals that these objects do not appear to be spherical. Indeed, only 4 of these objects have an aspect ratio consistent with a spherical geometry. The mean value of the aspect ratios as computed here is 0.63, suggesting that in our sample of cores the preferred geometry is a flattened, oblate one (Fig. 6). We therefore conclude that the shapes of the cores in the CWHFT10 sample are not consistent with the spherical geometry implied by the $B \propto \rho^{2/3}$ relation.

In our theoretical analysis of shapes, we considered only the case of a pure dataset following a specific geometry and evolutionary path. It is also conceivable that a mixture of different object geometries, each with its own $B - \rho$ relation, could yield a value of κ different from the values characterizing the individual objects, including possibly $\kappa = 2/3$. In order for such a scenario to be realized, objects with both smaller values of κ (i.e., 1/2 or 0) and greater values of κ (i.e., 1) need to be present in the sample. As discussed in §2.1, values of κ greater than 2/3 can be produced by one-dimensional contraction of a disklike (oblate) cloud with its magnetic field parallel to the plane of the disk, or the lateral contraction of a long cylindrical cloud with its magnetic field along the cylinder (see § 2). Both of these cases were found to be unlikely in a combined study of cloud shapes and magnetic fields using data for 32 clouds surveyed by the Hertz polarimeter (Tassis et al. 2009, see their Figs. 2b and 2e). The latter possibility is also contradicted by our study of the CWHFT10 core shapes alone, as it would require a different aspect ratio distribution than the one shown in Figure 6. The CWHFT10 aspect ratio distribution is similar in shape to the one of the sample studied

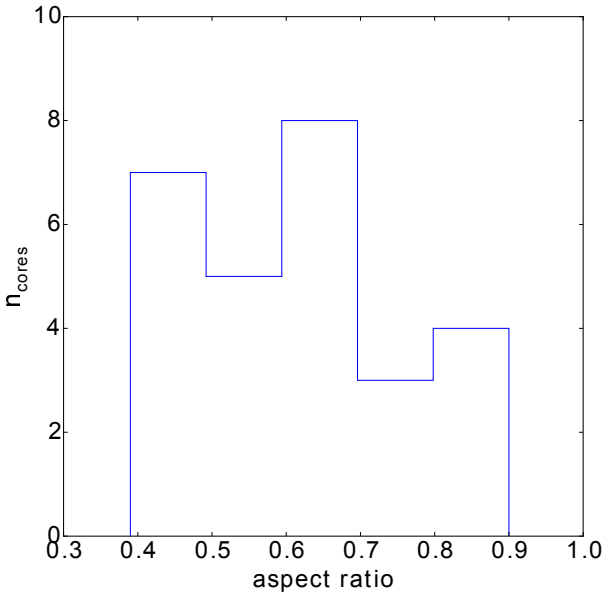

Figure 6. Distribution of the aspect ratios of the cores for which we could find observational data. The distribution peaks away from unity, in contradiction to what is expected from spherical geometry.

by Tassis (2007), and which was shown to be strongly peaked around intrinsically oblate cores. Even a uniform shape distribution (equal number of oblate and prolate objects) would require a much greater fraction of aspect ratios between 0 and 0.4. It is therefore unlikely, given what we know regarding core shapes and the orientation of their magnetic fields, that the CWHFT10 sample contains enough cores that evolve either as $B \propto \rho^{2/3}$ or as $B \propto \rho$ to effectively "pull" the observed $\log B - \log\rho$ relation away from a slope of 0.5.

3 TRACING THE SOURCE OF THE DISCREPANCY BETWEEN NONSPHERICAL SHAPES AND CWHFT10'S $\kappa = 2/3$

We have found in §2 that the preferred model in CWHFT10 would require spherical shapes, which are very rare among their observed objects. In this section, we focus on tracing the cause of the disagreement between the results of the CWHFT10 analysis and the results of our own tests.

3.1 A joint treatment of HI and molecular clouds?

One likely culprit is the set of assumptions regarding the *family of models* CWHFT10 used to describe their data. The conclusion of CWHFT10 about the $B - \rho$ relation is obtained through a careful Bayesian analysis. Despite the important conceptual and methodological advantages of Bayesian statistics in treating diverse datasets, Bayesian analyses are necessarily model-dependent: they select the best parameter values in a specific family of models to treat the data at hand; but they do not convey information on how good a fit to the data the adopted family of models is as a whole. For example, a Bayesian analysis can always find a set of parameters of a normal distribution that best describe a specific dataset, even if the data are not distributed normally. However, that "best description" is actually a very poor representation of reality.

A central assumption in the CWHFT10 family of models that could be affecting their findings on the value of the exponent κ is that concerning low densities (HI data), namely, that the average magnetic field remains constant with density. This assumption is problematic for two reasons. First, observationally, it is not consistent with our *empirical* understanding of the behavior of magnetic fields with density for HI clouds. Several values of κ have been proposed, but the value $\kappa = 0$ has not been one of them (e.g., see review by Vallee 1997). This has also been reported by Marchwinski et al. (2012), who explicitly contrasted their results to the model adopted by CWHFT10 at low densities. Second, if one forces data on the $B - \rho$ plane on a horizontal line at low densities and demands continuity of the $B - \rho$ relation between low- and high-density datapoints, one necessarily sets a pivot point for the high-density part of the relation. If the value of the magnetic field at the "transition density" n_0 (the density which separates the low-density and high-density branches of the model) is too low, the value of κ for the high-density part of the $B - \rho$ relation will be forced to acquire greater values in order to accommodate the magnetic fields at the highest densities.

We devise a "goodness of fit" test to quantify whether indeed the assumption that the average magnetic field in HI clouds is independent of density is consistent with the data, and whether this assumption can affect the global model fit.

We start with the set of observed number densities for the objects used in the CWHFT10 analysis. For each number density $n_{\rm i}$, we randomly select a magnetic field according to the best generalized model by CWHFT10. First we calculate the $B_{\rm max}$ value appropriate for $n_{\rm i}$ through,

$$B_{\rm max}(n) = \begin{cases} B_0, & n < n_0 \\ B_0(\frac{n}{n_0})^{\alpha}, & n > n_0 \end{cases} \quad (2)$$

where $B_0 = 10$ μG, $n_0 = 300$ cm^{-3}, $\alpha = 0.65$. We then select a total magnetic field $B_{\rm i}$ of the cloud from a uniform distribution with boundaries between $f \cdot B_{\rm max}$ and $B_{\rm max}$, as prescribed by CWHFT10. To account for various orientations we multiplied each $B_{\rm i}$ by $\cos(\phi)$ randomly drawn from a uniform distribution between -1 and 1, to obtain the line-of-sight magnetic field $B_{\rm LOS,i}$. We then "observed" this $B_{\rm LOS,i}$ by drawing a random value from a normal distribution with mean equal to $B_{\rm LOS,i}$ and standard deviation equal to the actual observational uncertainty σ_B recorded by CWHFT10 for the cloud with density $n_{\rm i}$.

In this way, we produce "mock" magnetic field observations *at the same densities* as the CWHFT10 dataset that are consistent with the CWHFT10 model for the magnetic field. We then compare the mock data with the actual magnetic field measurements through a Kolmogorov-Smirnov test. We perform the test for (i) the entire dataset, (ii) just HI observations, and (iii) just molecular observations. When we treat the entire dataset (HI and molecular observations), the K-S p-value for the $\alpha = 0.65$ case was 19.7% - the model is acceptable. However, when we treat the HI and molecular data separately, the picture changes: for the molecular observations alone (where B *is* dependent on ρ according to the CWHFT10 model), the p-value for $\alpha = 0.65$ is only 5.2% - only marginally consistent with the data. In the case of HI data, the K-S test p-value is only 0.35%: $B \propto \rho^0$ is *not* a good description of the low-density data.

Figure 7 shows the cumulative distribution functions (CDFs) of the measured line-of-sight value of the magnetic field, for the different datasets, and demonstrates what happens when we combine HI and molecular data: both HI and molecular datasets are in poor agreement with the model, but *in opposite directions*: one produces too few low values of B (data CDF starts out below the model), and the other produces too many (data CDF starts out above the model). Adding the two datasets together moves the data CDF closer to the model.

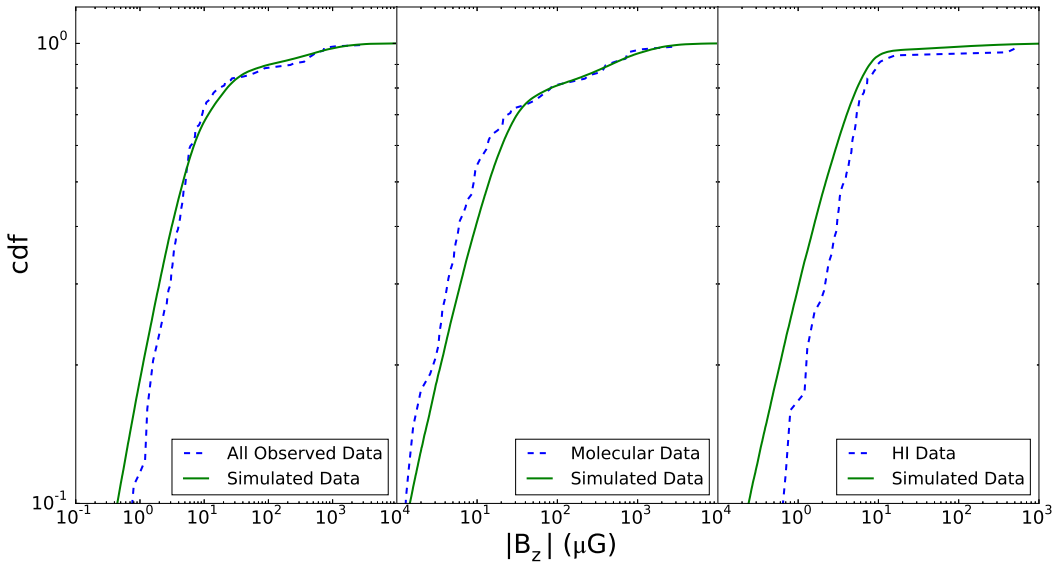

Figure 7. Cumulative distributions of the actual observations (dashed blue lines) and mock-observed values drawn from the CWHTF10 "best-fit" model (green solid lines) of each of the following cases: entire dataset (left), just molecular observations (middle), and just HI observations (right).

We have therefore shown quantitatively in this section that treating HI and molecular clouds jointly can affect the acceptability of a value of κ for the molecular branch of the model. For this reason, for the remainder of this work, we treat the molecular data by themselves.

3.2 An uncertainty of only a factor of 2 in volume densities?

An additional potentially problematic issue in the CWHFT10 analysis is the estimate of uncertainties in the density of each cloud/core. In CWHFT10 the issue is stated as follows: "Based on our experience in making such estimates, we choose to trust the inferred value within a factor of two, although the actual degree of uncertainty is not precisely known" (Cructher et al. 2010). However, the uncertainty in the data is an important factor in any statistical analysis. Underestimated uncertainties can make a dataset appear much more constraining than it really is. For this reason, we try to assess the actual degree of uncertainty for as many objects as possible by conducting a literature search of density estimates for each object and examining the spread between different estimates.

In approximately half of the total number of molecular datapoints given in Crutcher et al. (2010), volume densities are taken from surveys different from those from which the magnetic field data are taken. Even if the centre coordinates and angular resolution between the Zeeman survey and the one probing other physical parameters are the same, volume densities are usually derived from CO and CS measurements (see appendices in Crutcher 1999, and Falgarone et al. 2008). This introduces a bias since these molecules provide information for regions different from those where Zeeman emission occurs. Additional chemical assumptions, as for example the $N(H_2)/N(CO)$ ratio and the depletion of the species onto dust grains, can further complicate the picture (see Tassis et al. 2012; 2014).

An example of the spread of volume-density estimates using different tracers is DR21OH: Vallée & Fiege (2006) used ^{12}CO observations to determine the volume density of the core, which they reported to be $n(H_2) = 3.4 \times 10^5$ cm^{-3}. Mangum et al (1991) used C^{18}O observations to derive $n(H_2) \geq 6 \times 10^6$ cm^{-3} for the same object. The difference is over an order of magnitude, much greater that the factor of 2 used by CWHFT10. Further uncertainties are introduced through the morphology of the cores. In absence of a better practice, column densities are converted to volume densities by assuming spherical geometry. However, no real information exists for the line-of-sight size of the core. It is clear from the above that the uncertainties in the volume densities can be much greater than the factor of two adopted by CWHFT10.

Studying the cited literature, we find that volume-density values reported in CWHFT10 are not always consistent with the references to which they are attributed, presumably as a result of updated data analysis (cores NGC2024, L1457S, L1457Sn, L1495(6), L1534, L1544). In any case, the changes in the adopted volume densities are indicative of the uncertainties introduced by various choices in the data analysis.

Even if discrepancies greater than a factor of two are only present in a small number of cases, since the total number of points is small, the resulting effect on the statistical analysis of the dataset can be significant. We find the greatest variations for the more evolved cores; measurements of volume densities in other literature sources are generally greater than the ones reported in CWHFT10. Table 1 summarizes different volume density measurements for the fraction of CWHFT10 objects for which a literature search yielded additional density estimates. Figure (8) demonstrates the effect of density uncertainties on the slope of the $B-\rho$ relation in a simple way, focusing on datapoints with significant ($> 3\sigma$) measurements of the magnetic-field strength rather than upper limits. Objects for which multiple measurements of the volume density are available in the literature are shown in color. If the lowest available measurements of the volume density are used, the value of κ (apparent slope derived through log-log regression on the $B-\rho$ plane using detection-only data) is $\kappa_{ll} = 0.58$ (solid line). These points are consistent with the volume-density values adopted by CWHFT10. If the highest available

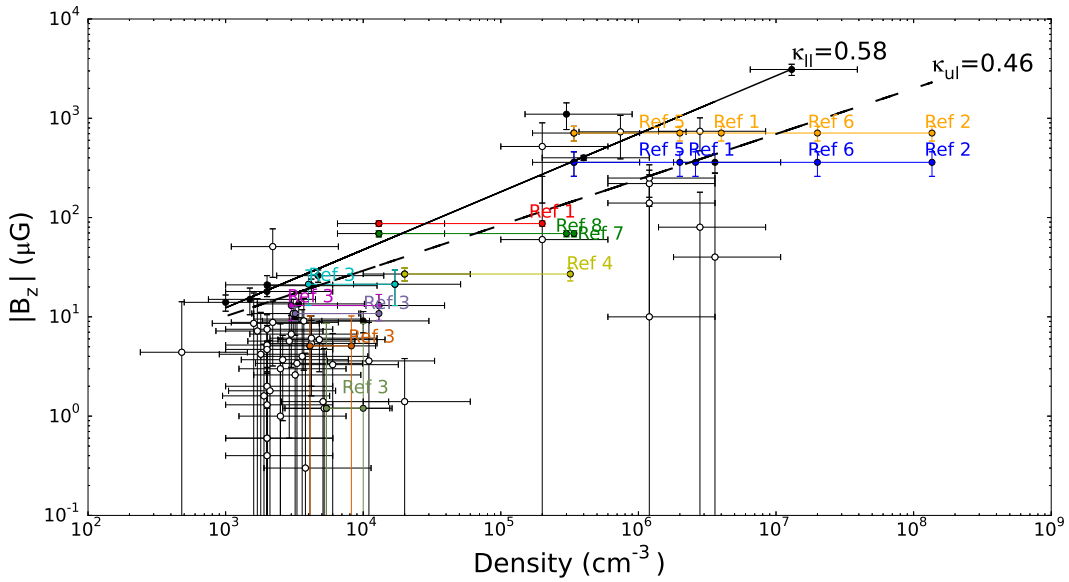

Figure 8. Two least-squares fits to detections only, when upper and lower limits of volume density measurements (curves labeled by $\kappa_{\rm ul}$ and $\kappa_{\rm ll}$, respectively) are adopted from the literature. Even when Zeeman measurements are accurate enough, volume density uncertainties can produce ambiguous results. Objects for which multiple measurements are available, and references, are given in Table 1.

measurements of the volume density are used, then $\kappa_{\rm ul} = 0.46$ (dashed line).

We can also quantify the statistical effect of the updated uncertainties, by performing a Monte-Carlo simulation of the apparent slope κ derived through a naive statistical analysis of mock observations drawn from the CWHFT10 model with updated uncertainties in the volume density where these are available (and a factor of 2 when no additional information is available). Our analysis is similar to that of Crutcher (1999): a single power law is fitted through regression to the detections-only data (as defined in Crutcher 1999: measured line-of-sight $|B|$ in units of its observational uncertainty greater or equal than 2.5). We repeat the "experiment" 10^5 times. The distribution of κ values obtained in this manner is shown in Figure 9. A Gaussian fit to the distribution shown yields a mean of 0.59 and a spread of 0.07: the detections-only slope is nonconstraining, and can be anywhere from ~ 0.4 to ~ 0.8 within 2σ (assuming the CWHFT10 model is correct).

We conclude that there are several cases for which the true uncertainty in the volume density is much greater than the factor of 2 adopted by CWHFT10, and that the effect of changing the adopted volume-density measurements within the range of estimates found in the literature can have a very significant effect on the $B - \rho$ relation of at least detections-only data.

In order to quantify the effect of the large volume-density uncertainties in the treatment of the entire datasets, we repeat the goodness-of-fit test of §3.1 for molecular objects only, properly accounting for uncertainties in density: for objects for which multiple volume-density estimates exist in the literature, we choose a density uniformly distributed in the available range. For other objects, we assign a density within a factor of two of the CWHFT10 value. We calculate the cumulative distribution of simulated (mock-observed) magnetic-field values and we check its consistency with the cumulative distribution of actual magnetic-field strength observations through a K-S test. The hypothesis that the two distributions are the same is rejected at the 0.3% level.

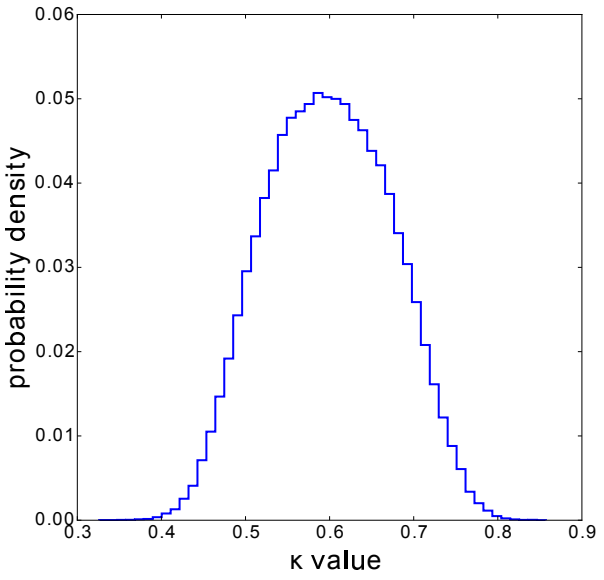

Figure 9. Distribution of apparent slope κ derived through log-log regression on the $B - \rho$ plane of detection-only data for the optimal model of CWHFT10, using updated volume-density uncertainties.

The reason for this discrepancy can be seen in Figure 10, which overplots data and model predictions on the $B - \rho$ plane. Using the same algorithm described above, we calculate, at each density bin, the median simulated $|B_z|$ (solid line) as well as the $|B_z|$ limits that contain 1σ (68%, dashed lines) and 2σ (95%, dotted lines) of our simulated observations. On the same plot, we overplot with red dots the measurements that come from molec-

Table 1. Density measurements of various objects in CWHFT10. Values from: Crutcher et al. 1999 (1); Mookerjea et al 2012 (2); Troland & Crutcher 2008 (3); Hirota et al. 1997 (4); Motte et al. 2007 (5); Girart et al 2013 (6); Sarma et al 2013 (7); Saito et al. 2007 (8).

Core	CWHFT10 value (cm^{-3})	Other Measurements (cm^{-3})	Ref.
NGC 2024	1.3×10^4	2×10^5	(1)
S88B	1.3×10^4	3×10^5	(8)
		3.4×10^5	(7)
DR21OH1	3.4×10^5	2×10^6	(1)
		1.36×10^8	(2)
		2×10^6	(5)
		2×10^7	(6)
DR21OH2	3.4×10^5	4×10^6	(1)
		1.36×10^8	(2)
		2×10^6	(5)
		2×10^7	(6)
L1457S	1.3×10^4	3×10^3	(3)
L1457Sn	1.7×10^4	4×10^3	(3)
L1534	5.4×10^3	1×10^4	(3)
L1544	3.2×10^3	1.3×10^4	(3)
L1595(6)	4.1×10^3	8.2×10^3	(3)
B1	2×10^4	3.2×10^5	(4)

ular tracers in CWHFT10. The cause of the strain registered by the K-S test between the CWHFT10 model and the data can be clearly identified in this plot. While reasonable fractions of points are within the expected 1σ and 2σ limits at various densities, they are not symmetric about the expected median: *a larger fraction of points lies systematically below the median than above.*

3.3 A flat distribution of magnetic field strengths?

A final potentially problematic assumption in CWHFT10 is that of the shape of the probability distribution of magnetic-field values. CWHFT10 adopt a uniform distribution of B-values, between some minimum and some maximum value. There are two issues arising from this choice. The first one is statistical. The uniform distribution is a convenient tool and significantly simplifies statistical analyses when it can be used without loss of generality or in absence of further information. However, it is always the most restrictive option among all frequently used bi-parametric distributions of the same variance σ^2. The reason is that, for a uniform distribution of finite width, the probability to have intrinsic (i.e., free of observational error) values of the quantity of

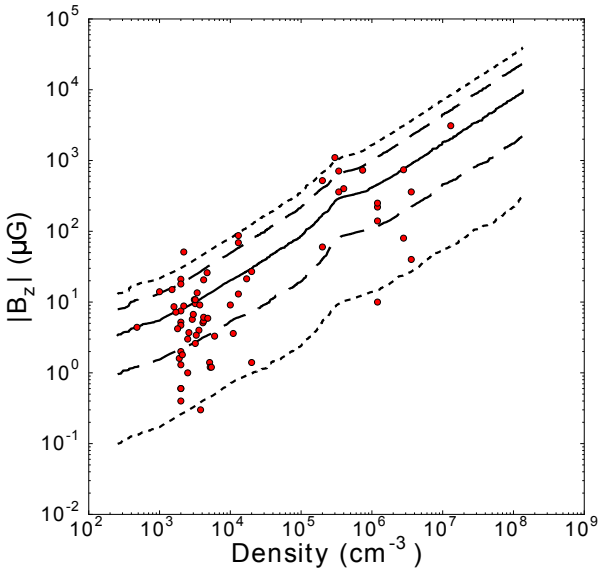

Figure 10. Median (solid line), 1σ (dashed lines) and 2σ (dotted lines) limits of the simulated $|B_z|$ at each density according to the CWHTF10 model, overplotted with molecular data from CWHTF10.

interest at a distance greater than $\sqrt{3}\sigma$ from the mean is exactly zero. This means that this type of distribution cannot adequately describe peaked distributions with tails. If a collection of datapoints that shows a preferred value (a peak) as well as outliers (tails) is forced onto a uniform distribution of variable width, the best fit that will be obtained by likelihood analysis is a uniform distribution that completely misses the peak and stretches out all the way to the farthest outlier. In terms of the $B-\rho$ scaling problem: in order to accommodate, say, a single abnormally high value of the B–field at very high densities, the uniform B-distribution has to stretch its maximum to very high values, and this could again result in a steeper scaling than otherwise warranted by the data. This effect of the uniform-distribution choice is somewhat moderated by the treatment of observational uncertainties (making the probability of observation of an outlier finite due to observational error), but it is not clear that this is enough to eliminate the bias that could potentially be introduced.

The second problem with the choice of a uniform distribution of B-values is conceptual. CWHFT10 assign a physical interpretation to the width of the best-fit uniform distribution they derive from their data: that, since the best-fit distribution extends uniformly from almost zero to a maximum value, this implies that there is no preferred value of the magnetic field in objects of a specific density, and that this is additional evidence for the dynamical insignificance of magnetic fields, compounded with their preferred 2/3 slope of the $B-\rho$ scaling. However, if there *were* a preferred value of the magnetic field in the interstellar medium, but there were also outliers, the CWHFT10 uniform distribution would miss it and, consequently, would lead to a misleading physical interpretation of the available data.

The first question we ask in addressing these issues is whether a different family of distributions which *is* capable of describing peaked distributions with tails may be an equally good or better fit to the magnetic-field data. Such a family of distributions is the lognormal,

$$p(B) = \frac{1}{B\sqrt{2\pi}\sigma_0} \exp\left[-\frac{(\ln B - \ln B_{\rm m,a})^2}{2\sigma_0^2}\right], \qquad (3)$$

which represents a Gaussian distribution of $\ln B$ centered at $\ln B_{\rm m,a}$ and with spread σ_0. We will identify optimal parameters for a lognormal (instead of a uniform) distribution of intrinsic magnetic-field strengths, B, which is consistent with the observed $|B_z|$ values in a narrow density range (from 2×10^3 to $4 \times 10^3\,{\rm cm}^{-3}$). We have chosen that particular density range because it is well populated (27 observed objects) so that it provides enough statistics to give a good sense of the underlying distribution, and narrow enough so that we can ignore any evolution with density between points.

In order to determine parameters of this distribution, we scan the two-dimensional parameter space of ($B_{\rm m,a}$, σ_0), and for each pair we simulate a distribution of observed $|B_z|$ with random observation directions (uniform $\cos\theta$) and including Gaussian observational errors identical to the ones quoted in CWHTF10. The resulting distribution is then compared to the distribution of observed $|B_z|$. Since the purpose of this work is not to repeat the sophisticated statistical analysis of CWHTF10 but simply to assess the effect of relaxing the potentially problematic assumptions, we have not formally obtained a best-fit distribution; instead, we selected the set of parameters that minimizes the K-S statistic (yielding, in our case, a K-S p-value of 80% of the two datasets to be drawn from the same distribution). This means that a proper fit (for example, through a maximum-likelihood analysis) may yield a slightly different set of optimal parameters, which, if anything, will be an *even better* fit to the data. The optimal parameters we have identified for the lognormal in this narrow density range are $\ln(B_{\rm m,a}/\mu{\rm G}) = 2.57$ and $\sigma_0 = 0.3$, respectively. We assign this distribution to a number density of $n_{\rm a} = 2.61 \times 10^3\,{\rm cm}^{-3}$, which is the average of the CWHTF10 quoted densities for objects in the density range we have considered. In the analysis that follows we assume that, for all densities above $300\,{\rm cm}^{-3}$, the distribution $p(B)$ remains lognormal with the same σ_0 at all densities, while $B_{\rm m}$ scales as

$$B_{\rm m}(n) = B_{\rm m,a}(n_{\rm a}) \left(\frac{n}{n_{\rm a}}\right)^{\alpha} . \qquad (4)$$

Figure 11 shows how the observed $|B_z|$ values in the density range we have considered compare to those expected from the optimal lognormal B distribution and the CWHTF10 uniform B distribution (assuming in both cases uniform viewing angles $\cos\theta$ and observational uncertainties as quoted in CWHTF10). It is clear that the lognormal is a better match for the qualitative behavior of the observed data.

Figure 12 shows the corresponding probability density functions for the intrinsic magnetic-field strength B (instead of the observed line-of-sight strength of the magnetic field, $|B_z|$) at the number density $n_{\rm a}$. The plot demonstrates how the CWHFT10 conclusion, that there appears to be no preferred value of the magnetic field at a specific density in the interstellar medium, because a wide uniform distribution is preferred over a much narrower one, is a direct result of the constraining nature of a uniform distribution: the optimal lognormal, which we have shown is a better qualitative description of the observed data, *does* show a significant peak, corresponding to a preferred value at a given density; however, significant tails exist. In contrast, the optimal uniform distribution misses this peak, and extends to high and low values in order to accommodate the tail values, giving the false impression that the spread in intrinsic B needed to explain the observed B_z is much greater than it is in reality.

4 RECONCILING THE $B - \rho$ RELATION WITH CORE SHAPES.

Having identified three potentially problematic assumptions in the CWHFT10 analysis, we now re-evaluate the information their (B_z, n) datapoints convey regarding the slope of the $B - \rho$ relation

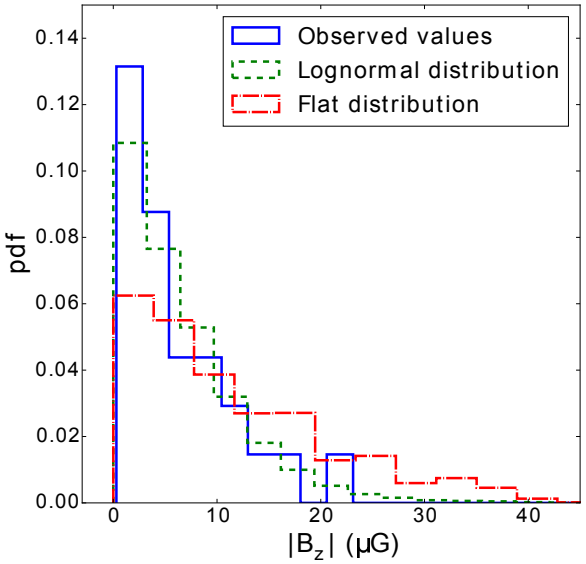

Figure 11. Distribution of line-of-sight magnetic field values B_z in the density range $2 - 4 \times 10^3\,{\rm cm}^{-3}$. Blue histogram (solid line): all observed objects (molecular data only). Green histogram (dashed line): optimal lognormal distribution. Red histogram (dashed-dotted line): CWHTF10 model (uniform distribution).

and we reconcile the latter with the lack of evidence for a preference for spherical geometry in the CWHFT10 cores. We do so by: (a) treating molecular (high-density) data on their own, since this is where the debated scaling ($B \propto \rho^{2/3}$ vs $B \propto \rho^{1/2}$) arises; (b) using updated uncertainties in the volume density where these are available; and (c) using a lognormal distribution of intrinsic magnetic-field strengths.

We repeat our goodness-of-fit tests of §3.1 using the optimal lognormal distribution described in §3.3, with its mean scaled with n with a slope α equal to either 0.65 (the CWHFT10 preferred value) or 0.5 (the historically preferred value due to theoretical expectations from magnetically-controlled gravitational contraction and due to the empirical results from fitting a power law to detection-only data). Figures 13 and 14 show the $|B_z|$ – n plane with lines corresponding to the median (solid), 1σ (long dashes), and 2σ (short dashes) expected limits of mock observations drawn from the lognormal model, with slope α equal to 0.65 and 0.5, respectively. A K-S test between the observed and simulated distributions of $|B_z|$ values in the entire density range of molecular datapoints, as in §3.2, returns a p-value of 7.5% for observed and simulated data to be drawn from the same distribution, for a scaling slope of 0.65; it returns a p-value of 15.2% for a scaling slope of 0.5.

The agreement between data and model has improved significantly even for a scaling slope of 0.65 (from 0.3% to 7.5%) by switching from a uniform distribution of B-values to a lognormal. This is achieved without changing the number of modeling parameters; both uniform and lognormal are bi-parametric families of distributions. However, a slope of $\alpha = 0.5$ is preferred over $\alpha = 0.65$, although the two cannot be distinguished at a statistically significant level.

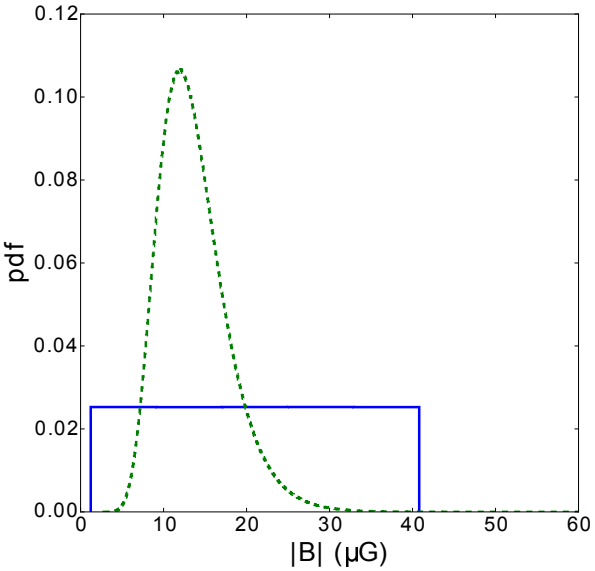

Figure 12. Distribution of intrinsic magnetic-field strength B at $n = 2.61 \times 10^3\,\mathrm{cm}^{-3}$. Green (dashed) line: optimal lognormal; Blue (solid) line: CWHTF10 model (uniform distribution).

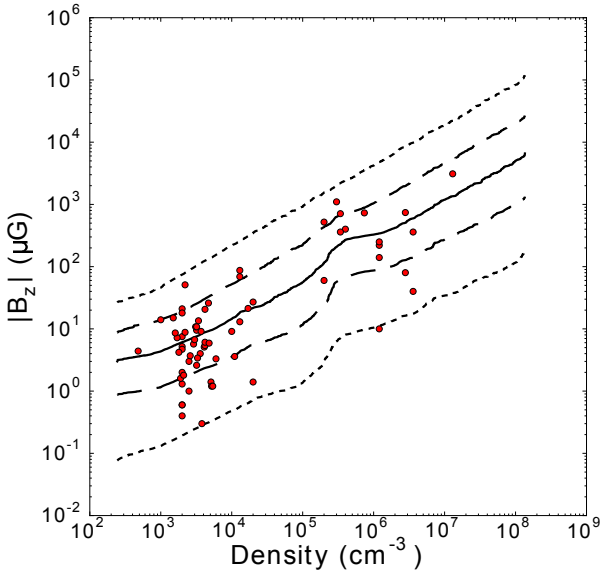

Figure 13. Median (solid line), 1σ (long-dashed lines) and 2σ (short-dashed lines) limits of the simulated $|B_z|$ at each density obtained from the optimal lognormal $p(B)$ and $\alpha = 0.65$, overplotted with molecular data from CWHTF10.

5 SUMMARY

In this paper, we discussed ways to assess the relation between the magnetic-field strength and the gas density in the interstellar medium.

We reviewed the connection between the exponent κ in the relation $B \propto \rho^{\kappa}$ and the geometry of a cloud. We showed that specific combinations of cloud geometry and magnetic-field orientation result in different $B - \rho$ relations, with $B \propto \rho^{2/3}$ being unique to the spherical-cloud (or core) geometry.

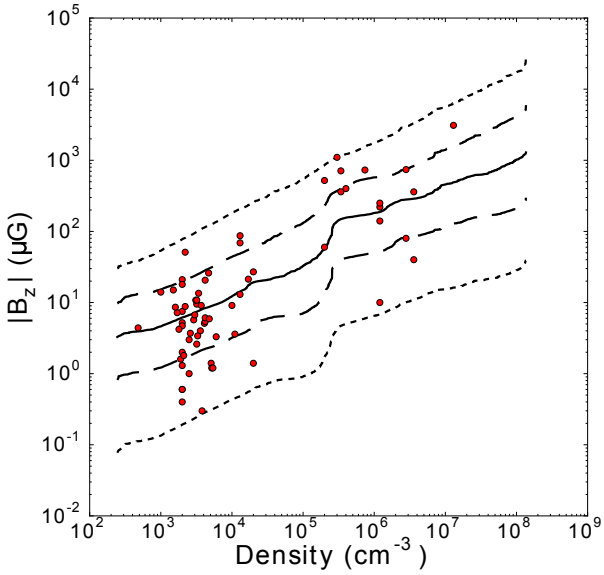

Figure 14. Median (solid line), 1σ (long-dashed lines) and 2σ (short-dashed lines) limits of the simulated $|B_z|$ at each density obtained from the optimal lognormal $p(B)$ and $\alpha = 0.5$, overplotted with molecular data from CWHTF10.

In light of this result, we sought to verify whether the claim of $B \propto \rho^{2/3}$ (at high densities) through the statistical analysis of a large sample of density and magnetic-field measurements by CWHFT10 is consistent with the geometry of objects in their sample. To this end, we have studied emission maps in all 27 objects in the CWHFT10 sample for which such data were available. We only found aspect ratios consistent with a spherical geometry in 4 of them; the distribution of aspect ratios does not show any preference toward unity, which would be the signature of spherical shapes. We thus concluded that there is no evidence of preferentially spherical objects in the CWHFT10, a result inconsistent with a $B \propto \rho^{2/3}$ relation.

We then investigated the possibility that this disagreement could be caused by simplifying assumptions in the CWHFT10 statistical analysis.

We first tested the effect of using a joint model for low- and high-density data and forcing the low-density data to a constant magnetic-field strength, independent of density. We used Monte-Carlo simulations to produce mock observations from the best CWHFT10 model with identical observational uncertainties as the ones quoted in CWHFT10, and we used a Kolmogorov-Sminrov test to determine whether the mock observations were consistent with the data. We found that:

- When treating the two branches (HI and molecular) of the CWHFT10 model separately, the low-density $B \propto \rho^0$ branch is inconsistent with the data (p-value = 0.35%), while the high-density branch is marginally consistent (p-value = 5.2%).
- These two branches deviate from the data in opposite directions, and, as a result, when we treat the combined dataset, we find artificially improved consistency (p-value = 19.7%).

We therefore conclude that the finding of CWHFT10, that a model with $B \propto \rho^0$ at low densities and $B \propto \rho^{2/3}$ at high densities is the preferred description of observations of densities and magnetic fields, is an artifact of their combined treatment of low- and high-density datapoints.

We also checked whether the uncertainty in volume densities of a factor of 2 adopted by CWHFT10 is a good estimate, by tracing literature sources and comparing different density estimates for the same objects when these were available. We found that for several objects the actual uncertainties, as reflected in the spread of estimates in the literature, are much greater. When repeating our consistency analysis between the high-density branch of the CWHFT10 model and the data using updated volume-density uncertainties, the agreement between model and data worsens, with the p-value dropping to 0.3%. The reason for this is that the additional density values available in the literature (especially at the highest-density objects) tend to be greater, instead of being symmetrically distributed about the value adopted in CWHFT10: more recent estimates have generally produced upward corrections in volume densities.

We investigated whether a lognormal distribution for $p(B)$ would yield better agreement with the data than the CWHFT10 uniform distribution. We found that it does.

Finally, we relaxed the three problematic assumptions, by (a) treating molecular observations on their own, (b) using updated volume-density uncertainties, and (c) using the optimal longormal to model the distribution of magnetic-field strengths. We repeated our goodness-of-fit K-S tests for the lognormal models, scaled with density with slopes of 0.65 (the optimal CWHFT10 slope) and 0.5. We found that the K-S test accepts both models. However there is a preference for $B \propto \rho^{1/2}$ (by a factor of 2 in the p-value of the K-S test), which is also preferred by the independent analysis of cloud shapes. This result is in agreement with predictions of the ambipolar-diffusion theory of star formation.

ACKNOWLEDGEMENTS

KT acknowledges support by FP7 through Marie Curie Career Integration Grant PCIG- GA-2011-293531 SFOnset. AT, GVP, and KT acknowledge partial support from the EU FP7 Grant PIRSES-GA-2012-31578 EuroCal. GVP, KT, and TM acknowledge support by the RoboPol project, which is implemented under the ARISTEIA Action of the OPERATIONAL PROGRAMME EDUCATION AND LIFELONG LEARNING and is co-funded by the European Social Fund (ESF) and Greek National Resources. TM is grateful for the hospitality of the Department of Physics of the University of Crete during part of this work and writing of this paper. AT, GP, and KT thank the Astronomy Department of Caltech, for its hospitality during various stages of this work. We have made ample use of the public *Herschel* Science Archive data products. We thank P. Goldsmith for providing the CO data of the Taurus Molecular Cloud and for comments on the manuscript. We are grateful to T. Hartquist for careful reading of the paper and insightful comments.

REFERENCES

Basu, S., Ciolek, G. E., 2004, ApJ, 607, 39
Chapman, N. L., Davidson, J. A., Goldsmith, P. F., et al., 2013, ApJ, 770, 151
Ciolek, G.E., Basu, S., 2006, ApJ, 652, 442
Crutcher, R. M., 1999, ApJ, 520, 706
Crutcher, R. M., Wandelt, B., Heiles, C., Falgarone, E., Troland, T. H., 2010, ApJ, 725, 466
Falgarone E., Troland T. H., Crutcher R. M., Paubert G., 2008, A&A, 487, 247
Fiedler, R. A., Mouschovias, T. Ch., 1992, ApJ, 391, 199
Fiedler, R. A., Mouschovias, T. Ch., 1993, ApJ, 415, 680
Gammie, C. F., Lin, Y. T., Stone, J. M., Ostriker, E. V., 2003, ApJ, 592, 203
Girart, J. M., Rao, R., Marrone, D. P., 2006, Science, 313, 812
Girart, J. M., Frau, P., Zhang, Q., Koch, P. M., Qiu, K., Tang, Y. W., Lai, S. P., Ho, P. T. P., 2013, ApJ, 772, 69
Goldsmith P. F., Heyer M., Narayanan J., Snell R., Li D., Brunt C., 2008, ApJ, 680, 428
Goodwin, S. P., Ward-Thompson, D., Whitworth, A. P., 2002, MNRAS, 330, 769
Hirota, T., Yamamoto, S., Mikami, H., Ohishi, M., 1997, ApJ, 503, 717
Jones, C. E., Basu, S., 2002, ApJ, 569, 280
Jones, C. E., Basu, S., Dubinski, J., 2001, ApJ, 551, 387
Kudoh, T., Basu, S., 2011, ApJ, 728, 123
Li, H.-b., Yuen, K.H., Otto, F., Leung, P.K., Sridharan, T.K., Zhang, Q., Liu, H., Tang, Y.-W., Qiu, K., 2015, DOI:10.1038 Nature14291
Li, P. S., Norman, M. L., Mac Low, M. M., Heitsch, F., 2004, ApJ, 605, 800
Mac Low, M. M., Klessen, R., S., 2004, RvMP, 76, 125
Mangum, J. G., Wootten, A., Mundy, L. G., 1991, ApJ, 378, 576
Marchwinski, R. C., Pavel, M. D., Clemens, D. P., 2012, ApJ, 755, 130
Mestel, L., 1965, QJRAS, 6, 265
Mestel, L., Spitzer, L. Jr., 1956, MNRAS, 116, 503
Mookerjea, B., Hassel, G. E., Gerin, M., Giesen, T., Stutzki, J., Herbst, E., Black, J. H., Goldsmith, P. F., Menten, K. M., Krelowski, J., De Luca, M., Csengeri, T., Joblin, C., Kazmierczak, M., Schmidt, M., Goicoechea, J. R., Cernicharo, J., 2012, A&A, 546, 75
Motte, F., Bontemps, S., Schilke, P., Schneider, N., Menten, K. M., Broguiere, D., 2007, A&A, 476, 1243
Mouschovias, T. Ch., 1976a, ApJ, 206, 753
Mouschovias, T. Ch., 1976b, ApJ, 207, 141
Mouschovias, T. Ch., 1979, ApJ, 228, 475
Mouschovias, T. Ch., 1987a, in Physical Processes in Interstellar Clouds, ed. G. Morfill & M. Scholer (Dordrecht: Reidel), 453
Mouschovias, T. Ch., 1991a, ApJ, 373, 169
Mouschovias, T. Ch., 1991b, in The Physics of Star Formation and Early Stellar Evolution, ed. C. J. Lada & N. D. Kylafis (Dordrecht: Kluwer), 61
Mouschovias, T. Ch., 1991c, in The Physics of Star Formation and Early Stellar Evolution, ed. C. J. Lada & N. D. Kylafis (Dordrecht: Kluwer), 449
Mouschovias, T. Ch., Ciolek, G., E., Morton, S., A., 2011, MNRAS, 415, 1751
Mouschovias, T. Ch., Morton, S., A., 1991, ApJ, 371, 296
Mouschovias, T. Ch., Morton, S., A., 1992a, ApJ, 390, 144
Mouschovias, T. Ch., Morton, S., A., 1992b, ApJ, 390, 166
Mouschovias, T. Ch., Spitzer, L., Jr., 1976, ApJ, 210, 326
Myers, P., C., Fuller, G., A., Goodman, A., A., Benson, P., J., 1991, ApJ, 376, 561
Ostriker, J., 1964, ApJ, 140, 1056
Pilbratt, G. L., Riedinger, J. R., Passvogel, T., Crone, G., Doyle, D., Gageur, U., Heras, A. M., Jewell, C., Metcalfe, L., Ott, S., Schmidt, M., 2010, A&A, 518, L1
Ryden, B. S., 1996, ApJ, 471, 822
Saito, H., Saito, M., Sunada, K., Yonekura, Y., 2007, ApJ, 659, 459
Sarma, A. P., Brogan, C. L., Bourke, T. L., Eftimova, M., Troland, T. H., 2013, ApJ, 767, 24
Tassis, K., 2007, MNRAS, 379, L50
Tassis, K., Mouschovias, T. Ch., 2007, ApJ, 660, 402
Tassis K., Dowell C.D., Hildebrand R.H., Kirby L., Vaillancourt J.E., 2009, MNRAS, 399, 1681
Tassis, K., Willacy, K., Yorke, H. W., Turner, N. J., 2012, ApJ, 754, 6
Tassis, K., Willacy, K., Yorke, H. W., Turner, N. J., 2014, MNRAS, 445, L56
Troland T. H., Crutcher R. M., 2008, ApJ, 680, 457
Vallee, J. P., 1997, Fund. Cosm. Phys., 19, 1
Vallee, J. P., Fiege, J. D., 2006, ApJ, 636, 332
Verschuur, G. L., 1969, Nature, 223, 140

Chapter 5

A new method for accessing the shapes of cores

Motivated by the need for accurate density estimates we have developed a new method for probing the shape of each prestellar core individually. With knowledge of the column density and the 3D shape of the core calculating the volume density is then trivial. Previous methods for the determination of the shape of prestellar cores on an object-by-object basis have been highly complex and with limited application to observational data (Steinacker et al. 2005; Li & Goldsmith 2012).

For over 70 years, molecules have been the leading probes of the physical conditions of molecular clouds and cores (see van Dishoeck & Blake 1998 for a review on interstellar chemistry). However, molecular emission maps have never been used to probe the shape of cores. The dynamical and chemical evolutions are coupled and thus different shapes translate to different abundance distributions (Aikawa et al. 2002; Tassis et al. 2012). Furthermore, the length of the path of integration also differs depending on the intrinsic shape of each core. Based on these two arguments we devised a method using integrated, molecular emission maps to access the intrinsic structure of cores. We have demonstrated that our method compared remarkably well with available observational data.

Mon. Not. R. Astron. Soc. **000**, 000–000 (0000) Printed 11 February 2016 (MN LATEX style file v2.2)

Chemistry as a diagnostic of prestellar core geometry

A. Tritsis[1], K. Tassis[1,2], K. Willacy[3]
[1]*Department of Physics, University of Crete, PO Box 2208, 71003 Heraklion, Greece*
[2]*IESL, Foundation for Research and Technology-Hellas, PO Box 1527, 71110 Heraklion, Crete, Greece*
[3]*Jet Propulsion Laboratory, California Institute of Technology, Pasadena, CA 91109, USA*

11 February 2016

ABSTRACT

We present a new method for assessing the intrinsic 3D shape of prestellar cores from molecular column densities. We have employed hydrodynamic simulations of contracting, isothermal cores considering three intrinsic geometries: spherical, cylindrical/filamentary and disk-like. We have coupled our hydrodynamic simulations with non-equilibrium chemistry. We find that *a*) when cores are observed very elongated (i.e. for aspect ratios ≤ 0.15) the intrinsic 3D geometry can be probed by their 2D molecular emission maps, since these exhibit significant qualitative morphological differences between cylindrical and disk-like cores. Specifically, if a disk-like core is observed as a filamentary object in dust emission, then it will be observed as two parallel filaments in N_2H^+; *b*) for cores with higher aspect ratios (i.e. $0.15 \sim 0.9$) we define a metric Δ that quantifies whether a molecular column density profile is centrally peaked, depressed or flat. We have identified one molecule (CN) for which Δ as a function of the aspect ratio probes the 3D geometry of the core; and *c*) for cores with almost circular projections (i.e. for aspect ratios ~ 1), we have identified three molecules (OH, CO and H_2CO) that can be used to probe the intrinsic 3D shape by close inspection of their molecular column density radial profiles. We alter the temperature and the cosmic-ray ionization rate and demonstrate that our method is robust against the choice of parameters.

Key words: ISM: clouds – ISM: molecules – star: formation – methods: numerical

1 INTRODUCTION

The intrinsic 3D shape of prestellar cores holds important clues about the star formation process since it is determined by the interplay of forces responsible for cloud fragmentation and core formation. Unfortunately, the two dimensional projection of a prestellar core on the plane of the sky probed by dust emission maps can be identical for different intrinsic 3D core shapes (Figure 1). Knowledge of the 3D structure of cores combined with observations that probe their kinematics and magnetic field could provide valuable insights as to which is the predominant mechanism that regulates star formation.

The significance of the problem has lead to numerous statistical studies over the past few years. Myers et al. (1991); Ryden (1996) and Curry(2002) each considered a sample of dense cores and suggested that prestellar cores have a preferentially prolate shape. More recent work (Jones, Basu & Dubinski 2001; Jones & Basu 2002; Goodwin; Ward-Thompson & Whitworth 2002; Tassis 2007; Tassis et al. 2009) has shown that most prestellar cores have an oblate morphology. The theoretical picture is no clearer. In MHD turbulent simulations (Gammie et al. 2003; Li et al. 2004) evidence points towards triaxial cores, with a preference to prolate shapes, whereas simulations where core formation is magnetically driven (Basu & Ciolek 2004; Ciolek & Basu 2006) indicate that prestellar cores should have oblate shapes. Spherical cores are not favoured in any of the studies mentioned above as they would require all 2D projections to be circular. However, close-to-round objects are observed in nature, albeit seldom. Poidevin et al. (2014) analysed a sample of 27 cores in the Lupus I cloud using *Herschel*-SPIRE 350 μm data. They found that 3 cores had aspect ratios consistent with that of a circular object. Similarly, Tritsis et al. (2015) considered a sample of 27 cores from various clouds and found that 4 had close to circular projections.

For circular objects, as projected on the plane of the sky, dust emission maps alone cannot break the degeneracy between disk-like, cylindrical and spherical cores. Dapp & Basu (2009) considered analytical column density profiles of prestellar cores and proposed:

$$\Sigma(x) = \frac{\Sigma_c}{\sqrt{1+(x/a)^2}} \times \arctan\left(\frac{\sqrt{R^2-x^2}}{\sqrt{x^2+a^2}}\right) \qquad (1)$$

as a column density profile appropriate for spherical cores. Here, R is the radius of the sphere, x is the offset from the

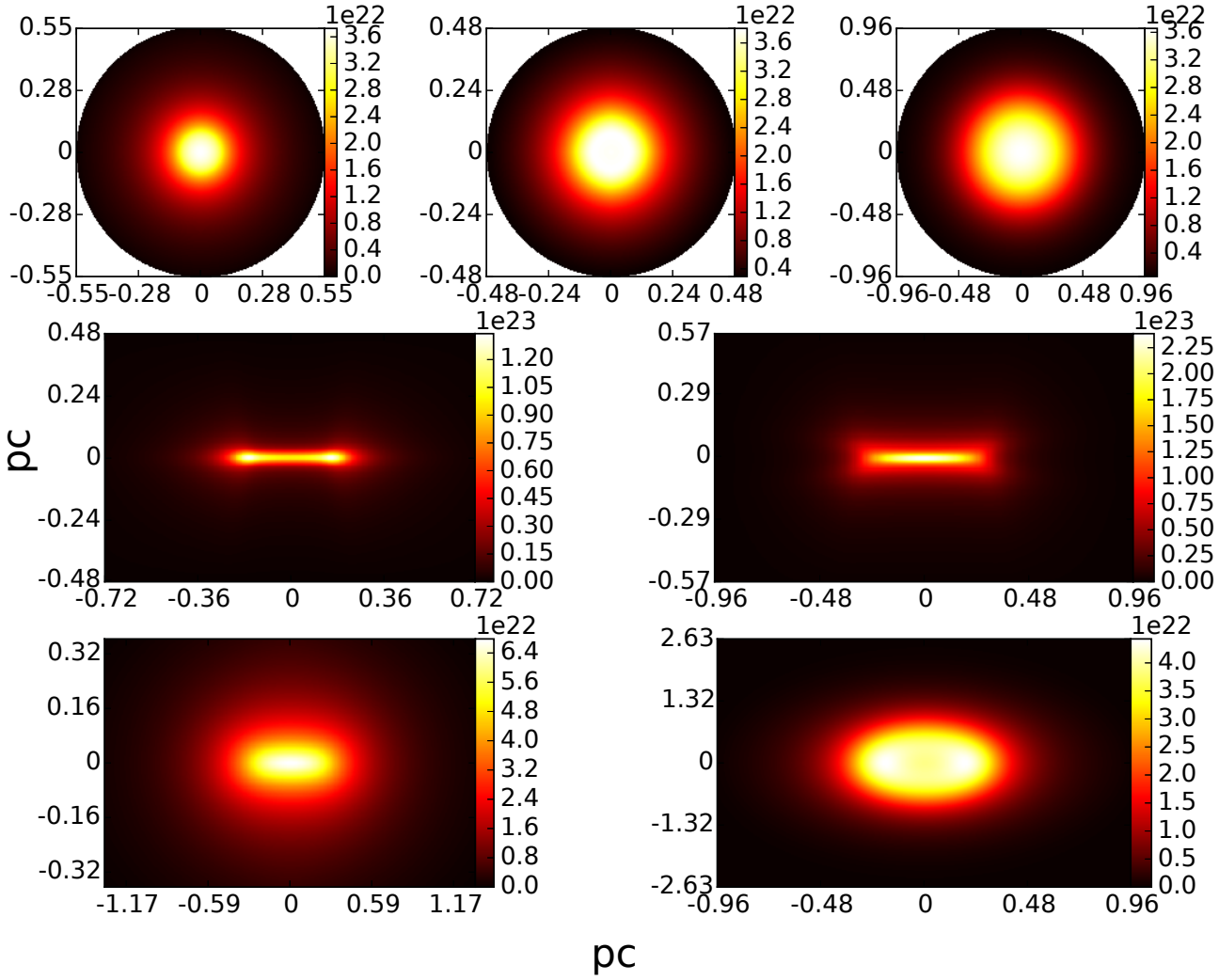

Figure 1. Total column density maps from our hydrodynamical simulations for a spherical (upper left), cylindrical (upper middle) and a disk-like (upper right) core as seen face-on. The middle panel depicts the total column density maps for the cylindrical (left) and disk-like (right) cores as seen edge-on. In the lower panels we show total column density maps for the cylindrical (left) and disk-like (right) cores each seen at an angle such that the aspect ratio of their projections is ~ 0.5.

centre, α is a parameter proportional to the Jeans length, and Σ_c is the central column density. In the same paper they find that the analytical expression for the column density profile for a thin disk viewed with its axis of symmetry parallel to the line of sight (face-on) is:

$$\Sigma(x) = \frac{\Sigma_c}{\sqrt{1+(r/a)^2}} \tag{2}$$

where r is the distance from the centre of the disk. For a filamentary cloud, integration of the volume density profile given in Arzoumanian et al. (2011) along the z-axis yields:

$$\Sigma_p(r) = \frac{\Sigma_c}{[1+(r/R_{flat})^2]^{p/2}} \tag{3}$$

where Σ_c is column density on the axis of symmetry of the cylinder, R_{flat} corresponds to the thermal Jeans length, and the value of p is determined from observations to be $1.5 < p < 2.5$. Thus, when the projections of all three geometries considered here are circular, their total column density profiles can in general be characterized by a flat inner part followed by a power-law decrease which steepens at large radii[1]. The ambiguity in the total column density profiles between different shapes and projection angles has also been pointed out by past numerical work (Boss & Hartmann 2001; Ballesteros-Paredes et al. 2003; Nielbock et al. 2012).

Despite the similarity of profiles in dust emission maps, much effort has been made to derive the 3D density distribution of prestellar cores from continuum observations. In a pioneering work, Steinacker et al. (2005) fitted the con-

[1] Observed column density profiles will deviate from the analytical expressions. A flaring disk seen face-on, will be observed as a ring in a column density map despite the fact that the maximum volume density is at its centre. However, the peak of the ring will be less than a factor of two larger than the column density at the centre of the disk.

tinuum emission map with Gaussian functions and using an inverse 3D radiative transfer technique they were able to reconstruct the intrinsic structure of the molecular core ρ Oph D. Lomax et al. (2013) fitted dust continuum observations from Ophiuchus, using Bayesian analysis with just one free parameter but with the a priori assumption that the intrinsic shapes were ellipsoids.

From the chemical point of view, comparison between simulations and molecular observations can provide important clues about the dynamics and the shape of the core. Keto et al. (2015) compared predicted spectra for H_2O ($1_{10} - 1_{01}$) and $C^{18}O$ ($1 - 0$) with observations from the starless core L1544 for various spherical models. They concluded that the contraction of the core was best approximated by that of a quasi-equilibrium Bonnor-Ebert sphere. Aikawa et al. (2003) were able to reproduce molecular column density profiles for the same core by adopting a Larson-Penston solution for the dynamics.

Molecular observations alone have also been used to estimate the line-of-sight dimensions of structures inside molecular clouds. Li & Goldsmith(2012) were able to estimate the line-of-sight dimension of the B213 region in Taurus using HC_3N (1 - 0) observations. They found that it was comparable to the smaller projected dimension and much smaller than the largest projected dimension, thus suggesting a cylindrical geometry. On the other hand, Storm et al.(2014) derived the line-of-sight dimensions of elongated structures seen in Barnard 1 from the kinematics of the gas. Interestingly enough, they found that the depths into the sky for some of them were comparable to their plane of the sky dimensions, thus suggesting a disk-like geometry.

Here, we present a new recipe designed to break the shape degeneracies caused by projections on the plane of the sky and probe a prestellar core's 3D structure. Our method is based on column densities of commonly observed molecules and can be applied to each core *individually*. This paper is organized as follows. In section § 2.1 we give an overview of our model. Our chemical network and the parameters altered in our models are described in § 2.2 and § 2.3 respectively. We present our results in § 3. We give a summary and discuss our conclusions in § 4.

2 NUMERICAL METHODS

2.1 Models of dynamically evolving cores

We have performed hydrodynamic simulations of self-gravitating, isothermal cores in 1D spherical and 2D cylindrical symmetry using the astrophysical code FLASH 4.0.1 (Fryxell et al. 2000; Dubey et al. 2008). We consider 3 intrinsic shapes; spherical, cylindrical/filamentary and disk-like. We solve the equations of hydrodynamics on an adaptive mesh grid with maximum nine levels of refinement (including the zeroth level). The maximum level of refinement yields a resolution of ∼10 AU. We use the standard FLASH multipole algorithm to solve Poisson's equation.

For each of our models, the initial density of the core is uniform and equal to 10^3 cm^{-3}. The extent of the computational area for the spherical models is 0.55 pc. In the cylindrical core models the axial and radial dimensions are 0.72 and 0.48 pc respectively. Finally, the size of the simulated region in disk-like core models is 0.96 pc in the radial direction and 0.57 pc in the axial direction. All modelled cores shape have four or more Bonnor-Ebert masses for all temperature values in our parameter study but with their masses being consistent with the core mass function (CMF) (Sadavoy et al. 2010). Thus, all cores are thermally supercritical to collapse.

Our cylindrical model will eventually fragment in two condensation at its edges with a mean separation of ~ 0.36 pc in agreement to observations (Kainulainen et al. 2015). However, for the intended purposes of the current paper, we end our simulations before the fragmentation of the cylinder proceeds at a stage where it cannot longer be considered a continuous structure.

Since our 2D simulations are cylindrically symmetric and in the interest of reducing computational cost we have only simulated one quadrant. At the outer boundary normal velocity components are forced to zero in guard cells so as to have no mass influx. Inner boundaries for these models as well as at both boundaries of our spherical model are reflective. We assume zero initial velocities in all dimensions and allow the cores to collapse under their self-gravity. We terminate each run when the central density reaches $\sim 10^7$cm^{-3}.

2.2 Chemical Network

We couple the dynamical models with non-equilibrium chemistry and follow the abundances of 214 gas-phase and 82 dust grain species. The evolution of these species is governed by 13967 chemical reactions. The reaction rates of our chemical network are adopted from the fifth release of the UMIST database (McElroy et al. 2013). In Table 1 we list all the species present in our network.

The initial elemental abundances, relative to the total density, are $[He] = 2.2 \times 10^{-1}$, $[Si^+] = 3.1 \times 10^{-8}$, $[N] = 3.3 \times 10^{-5}$, $[C^+] = 1.1 \times 10^{-4}$, and $[O] = 2.7 \times 10^{-4}$. Approximately 98% of hydrogen is in molecular form with the rest as H atoms. The total deuterium abundance is 1.87×10^{-5}, with 33% in molecular form and 66% in the form of HD. Thus, the C/O ratio is 0.4, the D/H ratio 1.6×10^{-5}, and the mean molecular weight is 2.4. The initial abundances of molecular species are $[H_2] = 7.6 \times 10^{-1}$ and $[D_2] = 6.2 \times 10^{-6}$. Therefore, at the beginning of each simulation, the only molecules present are H_2, D_2 and HD.

FLASH is able to monitor multiple fluids. We have appropriately modified the ionization unit which already has multispecies capabilities build in, and treat each molecular species as a different fluid. Thus, for each species a separate advection equation is solved with chemical abundances calculated after advection terms. The abundances of H_2 and D_2 are calculated from the conservation of the total hydrogen and deuterium at the end of each timestep. We follow the formulation of Tassis et al. (2012) to model gas-grain interactions.

The abundance profiles from our chemical model were compared with those of previous chemical studies (Tassis et al. 2012) and were found to be in good agreement. The results of these previous chemical runs were in turn extensively compared with observations from a number of dense cores (see Tassis et al. 2012 for a list of the observational studies). The values obtained from these observations are, within uncertainties, consistent with the range of predictions obtained by the chemical models.

Table 1. Chemical species considered

Gas phase species										
H^+	H	H_2^+	H_3^+	He	He^+	C	C^+	CH	CH^+	CH_2^+
CH_2	N	N^+	CH_3	NH^+	CH_3^+	NH	NH_2^+	O	CH_4	CH_4^+
O^+	NH_2	CH_5^+	OH	OH^+	NH_3^+	NH_3	H_2O	NH_4^+	H_2O^+	H_3O^+
C_2	C_2^+	C_2H^+	C_2H	$C_2H_2^+$	C_2H_2	CN	CN^+	HCN^+	$C_2H_3^+$	HCN
HNC	Si^+	$C_2H_4^+$	H_2NC^+	Si	N_2	CO^+	$HCNH^+$	CO	N_2^+	HCO
N_2H^+	HCO^+	H_2CO	H_2CO^+	NO	NO^+	H_3CO^+	CH_3OH	O_2	O_2^+	$CH_3OH_2^+$
C_3^+	C_3H^+	C_2N^+	CNC^+	$C_3H_3^+$	CH_3CN	CH_3CNH^+	CO_2	CO_2^+	HCO_2^+	HC_3N
HC_3NH^+	D^+	D	HD^+	D_2^+	H_2D^+	HD_2^+	D_3^+	CD	CD^+	CHD^+
CD_2^+	CHD	CD_2	CH_2D	CHD_2	CD_3	ND^+	CH_2D^+	CHD_2^+	CD_3^+	ND
NHD^+	ND_2^+	CH_3D	CH_2D_2	CHD_3	CD_4	CH_3D^+	$CH_2D_2^+$	CHD_3^+	CD_4^+	NHD
ND_2	$CH_4D_2^+$	$CH_3D_2^+$	$CH_2D_3^+$	CHD_4^+	CD_5^+	OD	OD^+	NH_2D^+	NHD_2^+	ND_3^+
NH_2D	NHD_2	ND_3	HDO	D_2O	NH_3D^+	$NH_2D_2^+$	NHD_3^+	ND_4^+	HDO^+	D_2O^+
H_2DO^+	HD_2O^+	D_3O^+	C_2D+	C_2D	$C_2D_2^+$	C_2HD	C_2D_2	DCN^+	$C_2H_2D^+$	$C_2HD_2^+$
$C_2D_3^+$	DCN	DNC	$C_2H_3D^+$	$C_2H_2D_2^+$	$C_2HD_3^+$	$C_2D_4^+$	$HDNC^+$	D_2NC^+	$DCNH^+$	$HCND^+$
$DCND^+$	DCO	N_2D^+	DCO^+	HDCO	D_2CO	$HDCO^+$	D_2CO^+	H_2DCO^+	HD_2CO^+	D_3CO^+
CH_2DOH	CHD_2OH	CD_3OH	CH_3OD	CH_2DOD	CHD_2OD	CD_3OD	CH_3OHD^+	$CH_3OD_2^+$	$CH_2DOH_2^+$	$CHD_2OH_2^+$
$CD_3OH_2^+$	CH_2DOHD^+	CHD_2OHD^+	CD_3OHD^+	$CH_2DOD_2^+$	$CHD_2OD_2^+$	$CD_3OD_2^+$	C_3D^+	$C_3H_2D^+$	$C_3HD_2^+$	$C_3D_3^+$
CH_2DCN	CHD_2CN	CD_3CN	CH_3CND^+	CH_2DCNH^+	CHD_2CNH^+	CD_3CNH^+	CH_2DCND^+	CHD_2CND^+	CD_3CND^+	DCO_2^+
DC_3N	DC_3NH^+	HC_3ND^+	DC_3ND^+	HD	CHD_2CNH^+	CD_3CNH^+	CH_2DCND^+	CHD_2CND^+	CD_3CND^+	DCO_2^+
C_3H_2	C_3H	$C_3H_2^+$	C_3HD	C_3D	C_3HD^+	C_3D_2	$C_3D_2^+$	H_2	D_2	
Dust grain species										
H	C	CO	H_2CO	Si	C_2	O_2	CH	OH	NO	CH_2
H_2O	CO_2	CH_3	CH_4	HNC	HCO	C_2H_2	HC_3N	N_2	CN	NH
HCN	C_2H	NH_3	CH_3CN	CH_3OH	NH_2	N	O	H_2	CH_2OH	D
HDCO	D_2CO	CD	OD	CHD	CD_2	HDO	D_2O	CH_2D	CHD_2	CD_3
CH_3D	CH_2D_2	CHD_3	CD_4	DNC	DCO	C_2HD	C_2D_2	DC_3N	ND	DCN
C_2D	NH_2D	NHD_2	ND_3	CH_2DCN	CHD_2CN	CD_3CN	CH_2DOH	CHD_2OH	CD_3OH	CH_3OD
C_2D	NH_2D	NHD_2	ND_3	CH_2DCN	CHD_2CN	CD_3CN	CH_2DOH	CHD_2OH	CD_3OH	CH_3OD
CH_2DOD	CHD_2OD	CD_3OD	NHD	ND_2	HD	D_2	CHDOH	CD_2OH	CH_2OD	CHDOD
CD_2OD	C_3H_2	C_3H	C_3HD	C_3D_2	C_3D					

Table 2. Parameters used in each run.

Runs	Temperature (K)	Ionization Rate (s^{-1})
1	10	1.3×10^{-17}
2	14	1.3×10^{-17}
3	7	1.3×10^{-17}
4	10	5.2×10^{-17}
5	10	3.3×10^{-18}

2.3 Parameter Study

We study the sensitivity of chemical abundances on the temperature and the cosmic-ray ionization rate by performing a suite of simulations. The parameters altered in each run are listed in Table 2.

For our reference run (i.e. run 1 in Table 2) we adopt typical H_2 cloud conditions. The temperature is set at 10 K, and a standard value of $\zeta = 1.3 \times 10^{-17}$ s^{-1} is used for the cosmic-ray ionization rate. For each shape, we consider models with T = 7 K and T = 14 K. We change the cosmic-ray ionization rate a factor of four above and bellow the standard value ($\zeta = 5.2 \times 10^{-17}$ s^{-1} and $\zeta = 3.3 \times 10^{-18}$ s^{-1} respectively). Thus, we have a total of 15 runs, 5 for each intrinsic geometry. The initial abundances of metals are the same for all runs.

3 RESULTS

We have produced and examined the column density maps, in various projection angles, of the total density and of all molecules present in our chemical network when the central density for all three geometries is 10^6 cm^{-3}. The total column density maps of our simulated cores when these appear circular (i.e with aspect ratios ~ 1), very elongated (i.e. with aspect ratios ≤ 0.15), and with an aspect ratio of $^1/_2$ are shown in the upper, middle and lower panels of Figure 1 respectively.

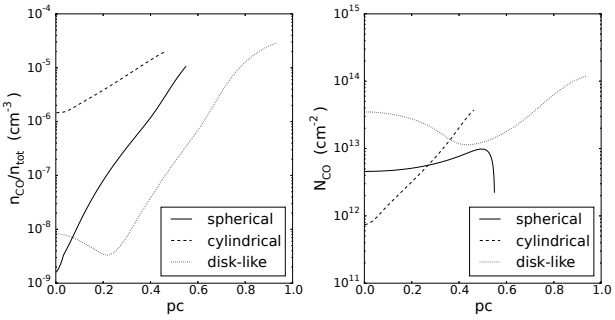

Figure 2. Radial profiles of CO abundance (left) and CO column density (right) for the three geometries. The disk-like and cylindrical core models are assumed to be viewed face-on. Abundance profiles for the disk-like and cylindrical cores are taken to extend radially from the maximum density point on the axis of symmetry. The central density for all three geometries is 10^6 cm^{-3}.

A two-dimensional projection of a spherical core will always be circular. Hence, candidates for spherical cores are the easiest to identify. Nonetheless, an indistinguishable, circular shape can also result from the projection of a cylindrical or a disk-like cloud if viewed with their axis of symmetry parallel to line of sight (face-on) (see upper panel of Figure 1). Therefore, even seeing a core as a close-to-round object in a dust emission map does not necessarily imply it is spherical. In the opposite case, when a disk-like and a cylindrical core are observed with their axis of symmetry perpendicular to the line of sight (edge-on), they would both appear as elongated objects almost identical to one another

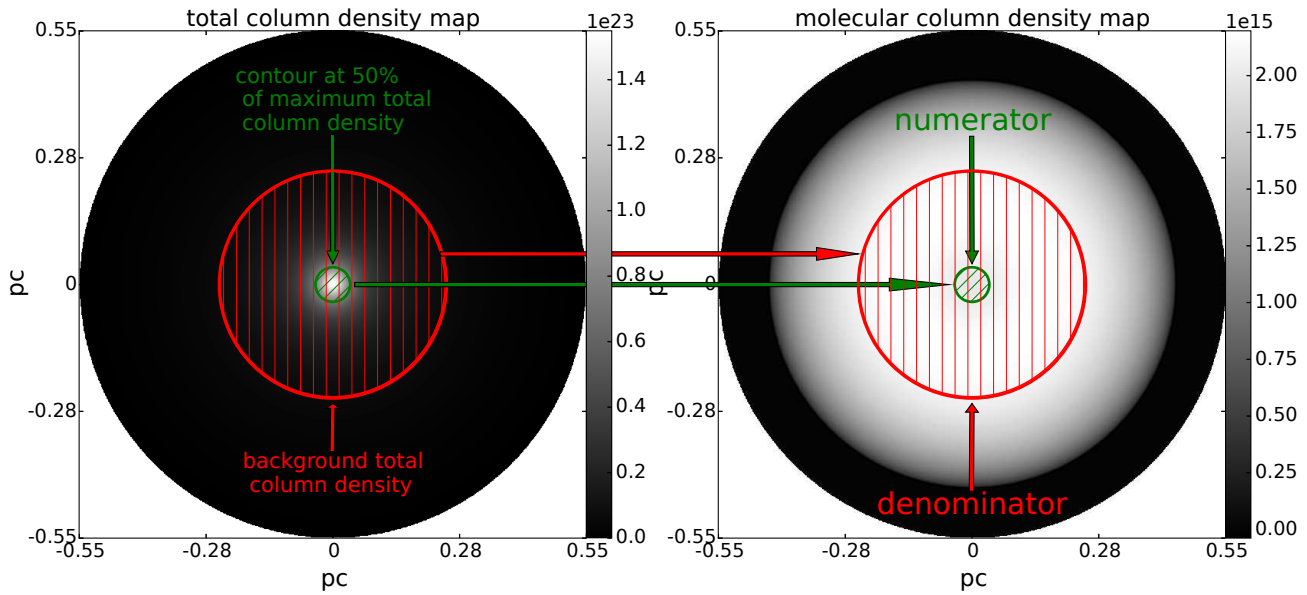

Figure 3. Schematic definition of the parameter Δ for a circular object. In the left panel we plot the total column density of our spherical model. The green circle is a contour that marks 50% of the maximum of the *total column density*. The numerator of Δ is the mean of the molecular column density inside that contour (*green hatched region* in the right panel). The red circle is a contour that marks the region of the core with total column density higher than a background value. The denominator of Δ is the mean of the molecular column density inside the red circle (*red hatched region* in the right panel). The molecular column density map here is that of CO for a spherical geometry.

(see middle panel of Figure 1). The degeneracy amongst the 2D projections of a disk-like and a cylindrical cloud remains for intermediate projection angles as well. In this case, both intrinsic 3D shapes would manifest themselves as ellipsoids with their aspect ratios depending on the projection angle. This is shown in the lower panel of Figure 1 when the cylindrical (left) and the disk-like cores (right) are both viewed such that their projections have aspect ratios $^1/_2$. For the same evolutionary stage, the projection angle required so that our simulated cylindrical and disk-like cores are seen as ellipses with aspect ratio $^1/_2$ would be 85° and 65° respectively. However, the frequency of the different aspect ratios varies for different intrinsic shapes and has been studied before (Curry 2002; Tassis 2007). Although our results are consistent with these studies, in the edge-on case these objects would be most probably identified as dense "filaments" rather than "cores" with the difference only being semantic.

Physical scales in Figure 1 are of little importance since in real life, a core of smaller size could be at a smaller distance and thus appear equal in size to a larger core at a larger distance. Depending on the mass and the evolutionary stage, two cores with different intrinsic geometries, located at the exact same distance, could have the same physical scales.

A molecular column density profile is determined by two factors:

(i) the distribution of the abundance of that molecule, and
(ii) the path of integration along a line-of-sight.

Clouds and cores with different intrinsic shapes evolve at different rates. Since the dynamical and chemical evolution are coupled (Aikawa et al. 2002; Tassis et al. 2012) the abundance of a molecular species and its distribution at a certain evolutionary stage will differ for discrete geometries. The path of integration along a line of sight is also subject to the core's morphology. We illustrate these two effects in Figure 2 assuming the disk-like and cylindrical cores are seen face-on. In the left panel we plot the abundance of CO and for all three intrinsic geometries the profiles are centrally depressed as expected for a depletion-affected molecule. In the right panel, we show the column density of CO for these geometries. For the spherical core it is only slightly centrally depressed, for the disk-like core it is slightly centrally peaked with an overall flat behaviour, and only for the cylindrical core does it resemble the true, abundance profile of CO.

It is clear that geometrical effects have a strong impact on the appearance of the core when it is observed through the chemical lens. The differences induced in molecular column density profiles from the intrinsic shape of the core can in turn be used to identify its true shape. However, radiative transfer processes also have a strong influence on how a core is observed on the plane of the sky. Such processes are approximated by either the critical density (n_{crit}) or by the effective density (n_{eff}).

The concept of critical density is an overly simplistic approximation since subthermal excitation of molecules is neglected. In addition, calculations of n_{crit} usually do not take under consideration optical depth effects. The effective density is defined as the density needed to produce an 1 K molecular line (Evans 1999). This is an easily detectable line. In contrast to n_{crit}, in n_{eff} radiative trapping is accounted

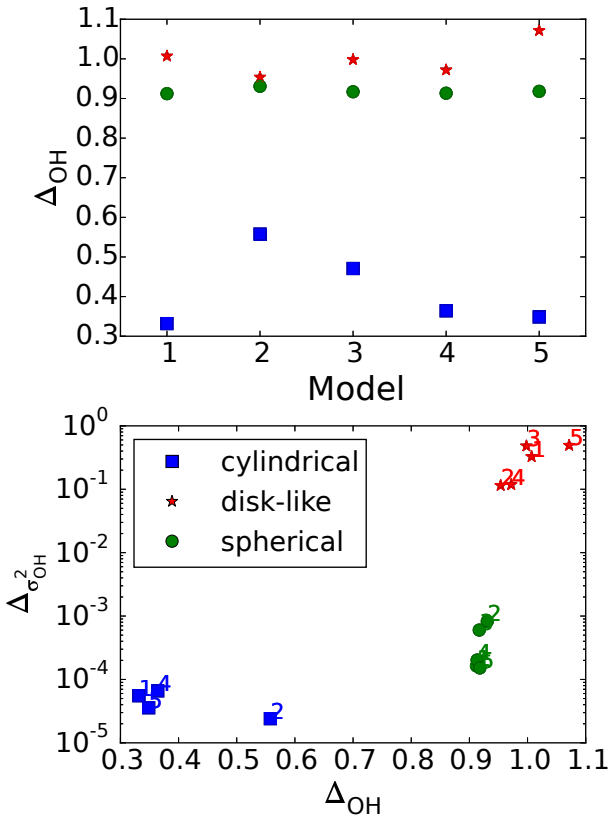

Figure 4. Upper panel: the value of the parameter Δ for OH for each run and each geometry separately. Lower panel: The parameter Δ_{σ^2} plotted against the parameter Δ. Symbols represent different intrinsic geometries (red star=disk-like, green circle=sphere, and blue square=cylindrical) and numbers denote runs with different parameters (see Table 2). Different intrinsic shapes occupy different regions of the plot.

for. The concept of n_{eff} is not free of caveats either. The approximation brakes down for low molecular column densities and is not appropriate to describe more complex molecules (CH_3CHO). However, we examine prestellar cores where the molecular column density is by definition high and we do not propose any complex molecule as a geometry tracer.

We produced our molecular column density maps by considering only the regions of the core with density higher than the effective excitation density. We repeated the same analysis by considering the critical density n_{crit} instead of n_{eff}. We present only the molecules for which the results with n_{crit} and with n_{eff} converge to each other. In this manner, we ensure that radiative transfer effects are negligible compared to the chemical effects. Critical and effective densities are adopted from Shirley (2015). Driven from observations (Marchwinski et al. 2012) and the discussion in Shirley (2015), we adopt a value of 10^2 cm^{-3} for the effective density of CO. For OH, which is commonly believed to be optically thin, we adopt a value of 4 cm^{-3} for the critical excitation density (Goldsmith & Li 2005).

For the disk-like and filamentary cores the path of integration and thus the column density also depends on the projection angle. For example, for a cylindrical core the path of integration will be larger when it is viewed with its axis of symmetry parallel to the line of sight rather than when it is seen with its axis of symmetry perpendicular to the line of sight. What is more, the molecular abundance distribution and the fact that we are only considering the portions of the core where $n_{tot} \geq n_{eff}$ when integrating, will have an effect on the resulting molecular column density map which also depends on the projection angle. Hence, we distinguish three cases; face-on, edge-on and intermediate angles. We have identified geometry-probing molecules that apply for each case *separately*. Consequently, the aspect ratio of the projected object as observed in dust emission determines the geometry-probing molecules that should be used.

3.1 Face-on

Face-on, when all intrinsic 3D shapes appear circular, we only get one-dimensional information from the column density profiles for all intrinsic geometries (along the radius of the projected, circular object). The true 3D shape of a core has such a strong effect on the molecular column density profile that for a specific geometry the profiles appear similar for the majority of molecules or for group of molecules. In spherical cores, depletion is not obvious in column density maps in any of the molecules in our chemical network, not even for the ones that are most affected by it, such as CO and HCO^+. The reason for this is that the path of integration shortens as the offset from the centre increases. Hence, lower abundances in the centre of spherical cores are counterbalanced by the larger integration paths.

In disk-like cores, seen face-on, molecular column density profiles are usually flat since the path of integration is always the same and molecular abundances mostly change within an innermost, very thin disk. In cylindrical cores, we meet a variety of behaviours. For this intrinsic shape, column density profiles are either very centrally peaked or very centrally depleted. The difference with disk-like cores is that now abundances vary in a much larger portion of the core. If, for example, we consider a depletion-affected molecule, then in cylindrical cores we integrate through more gas where the abundance of that molecule is low than we do in disk-like cores.

Therefore, we need a way to measure the quantitative differences of molecular profiles. To do so, we define two parameters. The first parameter Δ is defined to be the ratio of mean values of molecular column density in two different regions of the core. These two regions are defined based on the *total column density* traced by dust emission maps. More specifically, the numerator is the mean molecular column density inside a contour that marks 50% of the maximum total column density. The denominator is the mean of the molecular column density in the extent of the core where the total column density is higher than a background value, i.e.:

$$\Delta = \frac{\overline{N_X} \text{ inside a contour that marks 50\% of the maximum of } N_{tot}}{\overline{N_X} \text{ in the extent of the core where } N_{tot} \geq \text{background value}}$$

where X is a molecular species and the background total column density value is set to 7×10^{21} (Könyves et al. 2013)[2].

[2] We have verified that results do not change significantly if the

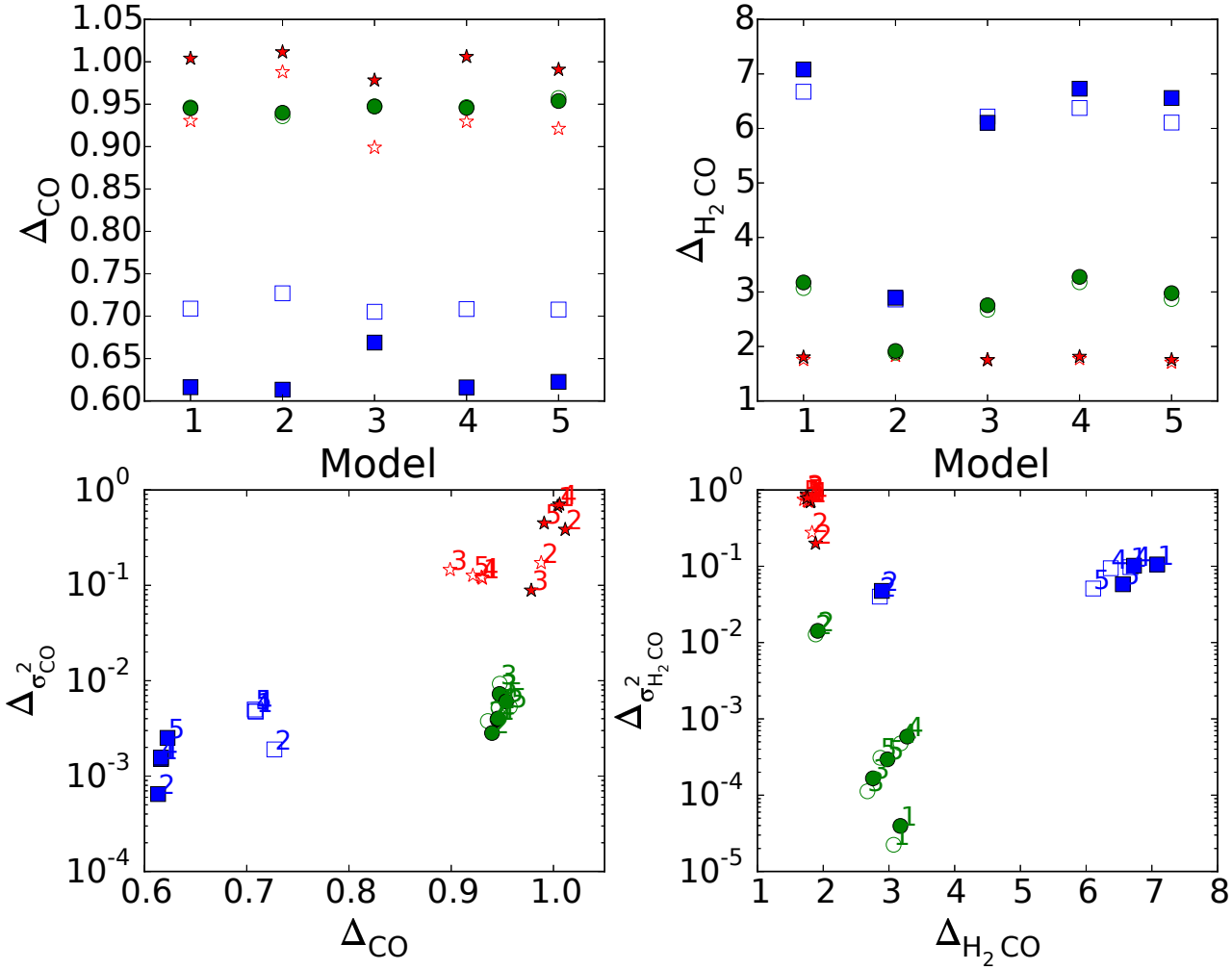

Figure 5. Same as in Figure 4 for CO (left column) and H_2CO (right column). Numbers denote models with different parameters (see Table 2) and symbols represent different intrinsic geometries, as in Figure 4 (star=disk-like, circle=sphere, and square=cylindrical). We use open symbols to plot the results where we considered n_{crit} instead of n_{eff} when producing the molecular column density maps.

The definition of Δ is also shown schematically in Figure 3. Here we show the total column density map (left panel) and the column density map of CO (right panel) for the spherical core. We have also overplotted the contour marking 50% of the maximum of the total column density with a green circle and the one marking the region of the core with $N_{tot} \geq 7 \times 10^{21}$ with a red circle in both maps.

The second parameter Δ_{σ^2} is the ratio of the variance of the molecular column density profiles in the same two regions of the core. Hence, while Δ quantifies whether a molecular column density profile is centrally peaked (> 1), depressed (< 1) or flat (≈ 1), Δ_{σ^2} quantifies how much a profile changes from the central to the outer regions of the core. Since the parameter Δ is a ratio of mean values, it can be confidently computed even from low resolution observations. However, to adequately describe the variation of molecular column density from the inner to the outer regions of the core and thus the parameter Δ_{σ^2}, high angular resolution data are required.

In the upper panel of Figure 4 we plot the parameter Δ for OH for each run and for each intrinsic geometry separately. We plot our results with red stars for the disk-like core, with blue squares for cylindrical core models, and with green circles for spherical cores. We present only the results obtained considering n_{eff} but results considering n_{crit} are identical since both values are very low. For our cylindrical core models, the column density profiles of OH are centrally depressed and clearly separate from the other two intrinsic shapes. The profiles of both the disk-like and spherical models are only slightly centrally depressed and the parameter Δ alone cannot break the degeneracy. However, when we plot the parameter Δ_{σ^2} against Δ in order to also include how the profiles change, the three geometries clearly separate. This is shown in the lower panel of Figure 4 where

contour in which we compute the numerator is changed to 25% or 70% of the maximum of the total column density and the background column density is changed a factor of two above and below the value adopted here.

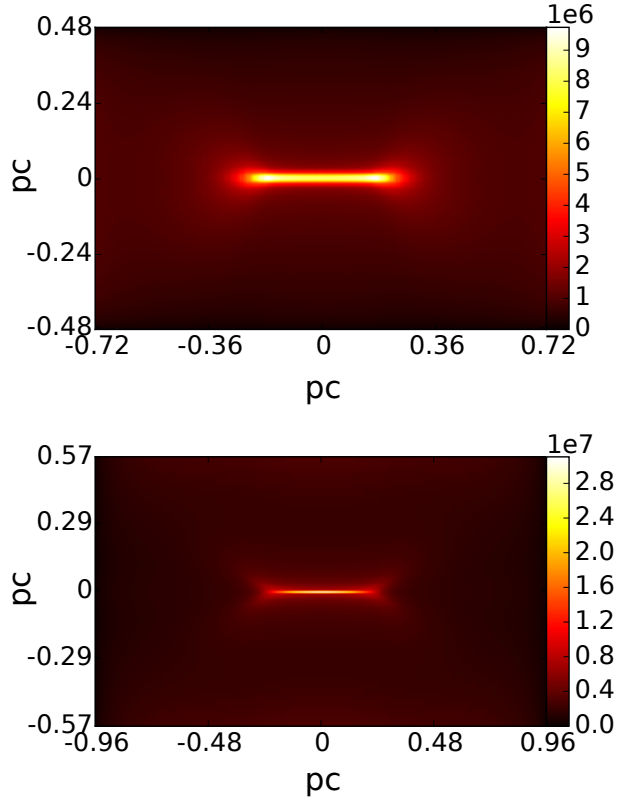

Figure 6. CD_2 column density maps for a cylindrical (upper panel) and an disk-like (lower panel) core. The maps closely resemble those of the total column density.

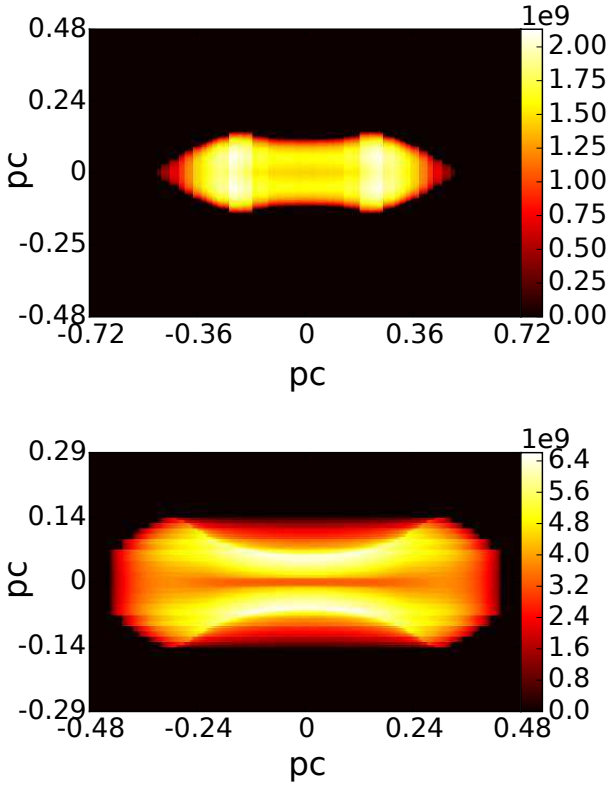

Figure 7. Zoomed N_2H^+ column density maps for a cylindrical (top) and a disk-like (bottom) core seen edge-on. Temperature and ionization rate are those of our reference run. The disk-like core would be observed as two parallel filaments whereas the cylindrical core would split into two horseshoe-shaped cores.

the numbers next to each symbol denote runs with different parameters. Two more molecules, CO and H_2CO, that can be used in the same manner are shown in Figure 5. In this Figure, we use open symbols to plot the results obtained with n_{crit}. Thus, *the intrinsic geometry of a circular object can be identified by plotting the parameter* Δ_{σ^2} *against the parameter* Δ *for specific molecules. Different intrinsic 3D shapes will occupy different regions of the plot.*

3.2 Edge-on

When disk-like and cylindrical clouds are observed edge-on (i.e. for aspect ratios ≤ 0.15), distinguishing them from spherical clouds is trivial. What is more, we now get two dimensional information (e.g. along the 2 principal axes of the projected object) and classification of clouds can be made without use of the parameter Δ. Instead, a simple comparison of 2D emission maps from observations with column density maps from simulations for key molecules is sufficient.

All fully deuterated hydrocarbons consisting of one carbon atom trace the total column density very accurately and thus the resulting maps for both a cylindrical and a disk-like core would be qualitatively indistinguishable from a dust continuum emission map. For CD_2 this is shown in Figure 6. Certain fully deuterated hydrocarbons consisting of two carbon atoms, such as C_2D_2 also behave in the same manner. Partly deuterated hydrocarbons with one or more carbon atoms such as C_2HD and CH_2D may also be good density tracers but this is not a robust property against the parameter study. Since these molecules follow the total density we have not taken into account radiative transfer processes when producing their column density maps. If the critical densities of these molecules are much higher than 10^6 cm^{-3}, i.e. the central density of all three modelled cores, then they will not be detected in a core of that evolutionary stage. However, if their critical densities are smaller than 10^6 cm^{-3} then they will continue to trace the central region and their molecular column density maps will qualitatively resemble those of the total column density in all projection angles and thus suffer from the same degeneracies with respect to the intrinsic shape.

Qualitative differences between cylindrical and disk-like clouds are observed in the column density maps of certain molecules with low critical densities. In CH_3N and OH, disk-like cores manifest themselves as a depletion hole. In contrast, an irregular shape with no clear structures results when the core is cylindrical. Unfortunately, the differences are not large enough in order for these molecules to be used as probes of the intrinsic geometry.

In Figure 7 we show zoomed N_2H^+ column density maps of the cylindrical (upper panel) and disk-like (lower panel) cores for our reference run. In N_2H^+ a disk-like core

would be observed as two semi-parallel, slightly bent filaments. Cylindrical cores, which are a better approximation to a filamentary cloud, will either be seen as two separate elliptical objects or as continuous elongated structures, similar to but broader than in dust emission maps. Column density maps of N_2H^+ for the rest of our parameter study runs are shown in Figures 8 & 9. When the N_2H^+ column density maps of disk-like cores are produced by considering n_{crit} instead of n_{eff} this *splitting effect* is still prominent.

The effect does not uniquely occur for N_2H^+. Other molecules that follow the same behaviour are NH_3 and C_3H_2. The column density maps of these molecules are very similar to those of N_2H^+ for both intrinsic shapes. For NH_3 this splitting in molecular column density maps of disk-like models occurs independently of whether we include radiative transfer effects in our analysis. In contrast, for C_3H_2 the effect is visible only when we consider the regions of the core with $n_{tot} \geq n_{eff}$.

As a result, whether the *splitting effect* is visible in a molecular column density map of our disk-like core also depends on the critical density of the molecule under consideration. In contrast to C_3H_2, the effect is visible in CH_3CN if we neglect the critical density when integrating to get its 2D projection map but it is not visible when we properly take it into account. In the latter case, the CH_3CN column density maps of both the disk-like and cylindrical core models resemble those of the total column density. If the critical density is neglected, the *splitting effect* is also seen in the molecular column density maps of HCO_2^+, H_2CO, H_2DO^+, CD_3^+, $C_3H_2D^+$, CHD_2^+, CH_2D^+, CH_4, CO_2, and DCO_2^+ provided of course that the shape of the core is that of the disk. Thus, these molecules are promising candidates in which the *splitting effect* may be seen, especially if they have transitions with low effective densities.

This *splitting effect* can be understood if depletion is considered. Despite the fact that N_2H^+ is a high-density tracer (Tafalla et al. 2002), at very high densities depletion will eventually take over. Bergin et al.(2002) took N_2H^+ (1 - 0) observations of the well studied prestellar core B68 using the IRAM 30 m telescope (beam size 25"). They found an N_2H^+ depletion hole towards the centre of the core. Pagani et al. (2007a) & Pagani et al. (2007b) observed the prestellar core L183 with the same telescope and found that N_2H^+ was depleted by a factor of 6 in the inner regions of the core. Chitsazzadeh et al. (2014) observed the prestellar core L1689-SMM16 and also found a decrease in abundance of NH_3 and N_2H^+ towards higher densities. Di Francesco et al. (2004) found evidence of N_2H^+ depletion towards the Ophiuchus A core. In agreement to these observations the abundance of NH_3 and N_2H^+ in our chemical models drops inside the high-density region. In Figure 10 we show, in 3D, the N_2H^+ abundance distribution for the disk-like (left) and cylindrical (right) core models. Isosurfaces are at 35% (blue isosurfaces) and 90% (red isosurfaces) of the maximum N_2H^+ abundance. The inner blue shaded isosurface of the disk-like core has a larger radius than that of the cylindrical core. Thus, for a thin disk seen edge-on, the effect in molecular column density will be more severe than that for a cylindrical cloud, since the path of integration along a line of sight passing through the high-density region is larger. Furthermore, for a disk-like core the high-abundance region of N_2H^+ will be parallel to the actual high-density region, whereas the opposite is true for a cylindrical cloud. Consequently, in such a map, the N_2H^+ column density will probe the regions above and below the disk. With this reasoning, one might expect that the column density of N_2H^+ would also probe the regions on either side of the high-density region of the disk. Hence, if the regions surrounding the disk were also connected, the resulting projected shape would be that of an empty ellipse. However, the gradient from the N_2H^+ column density peak towards the centre of the cloud is sharper in the z direction (see Figure 11) and the net result is two parallel elongated structures.

The *splitting effect* that occurs for disk-like cores might have already been observed. Fernández-López et al. (2014) observed the Serpens South molecular cloud in N_2H^+ ($J = 1 \rightarrow 0$) using CARMA. They found that what appeared as a single filamentary structure in dust continuum was actually composed of two or three N_2H^+ filaments. In a subsequent study of Serpens Main and with the same tracer, Lee et al. (2014) also found two separate filaments inside what appeared to be a filamentary structure in dust emission. They argued that with CARMA's higher resolution they were able to resolve substructures of the filamentary objects observed with *Herschel*.

Fernández-López et al. (2014) also estimated the width of the N_2H^+ filaments. They found that these structures had approximately half the width of the filaments observed in dust continuum. Figure 12 shows the total column density and N_2H^+ column density profiles, parallel to the short axis, for our cylindrical (left) and disk-like (right) core models. If the true 3D shape of the structure observed by Fernández-López et al. (2014) were that of a cylinder then, due to the fact that no splitting occurs for such an intrinsic geometry, the N_2H^+ profile would be broader, leading to a larger width, in contradiction to their results. If however, the intrinsic geometry of that object were disk-like, because of the splitting due to depletion, the two apparent N_2H^+ filaments would have smaller widths (right panel of Figure 12). Sugitani et al.(2011) took polarization measurements at the region observed by Fernández-López et al. (2014). They found that the magnetic field was perpendicular to the filamentary structure where the splitting occurs.

As a proof of concept we have created the N_2H^+ column density map of our disk-like core as seen edge-on at the highest resolution possible from the simulations. The core was then "placed" at a distance of 415 pc (i.e. the same distance adopted by Fernández-López et al. 2014 for the Serpens South Molecular Cloud) and the image was convolved using a Gaussian filter assuming a beam size equal to that of CARMA (7") (upper panel of Figure 13). We then convolved the original map to *Herschel's* 350 μm beam size (25") (lower panel of Figure 13). In agreement with the observational results of Fernández-López et al. (2014) the splitting is no longer visible when N_2H^+ emission is convolved to *Herschel's* resolution (see their Figure 3 where they perform the same analysis using observations).

3.3 Intermediate projection angles

Observationally, there is no way of determining the angle between the axis of symmetry of a core and the line of sight. Also, for the same projection angle, an ellipsoid resulting from a cylindrical cloud will have a different aspect ratio

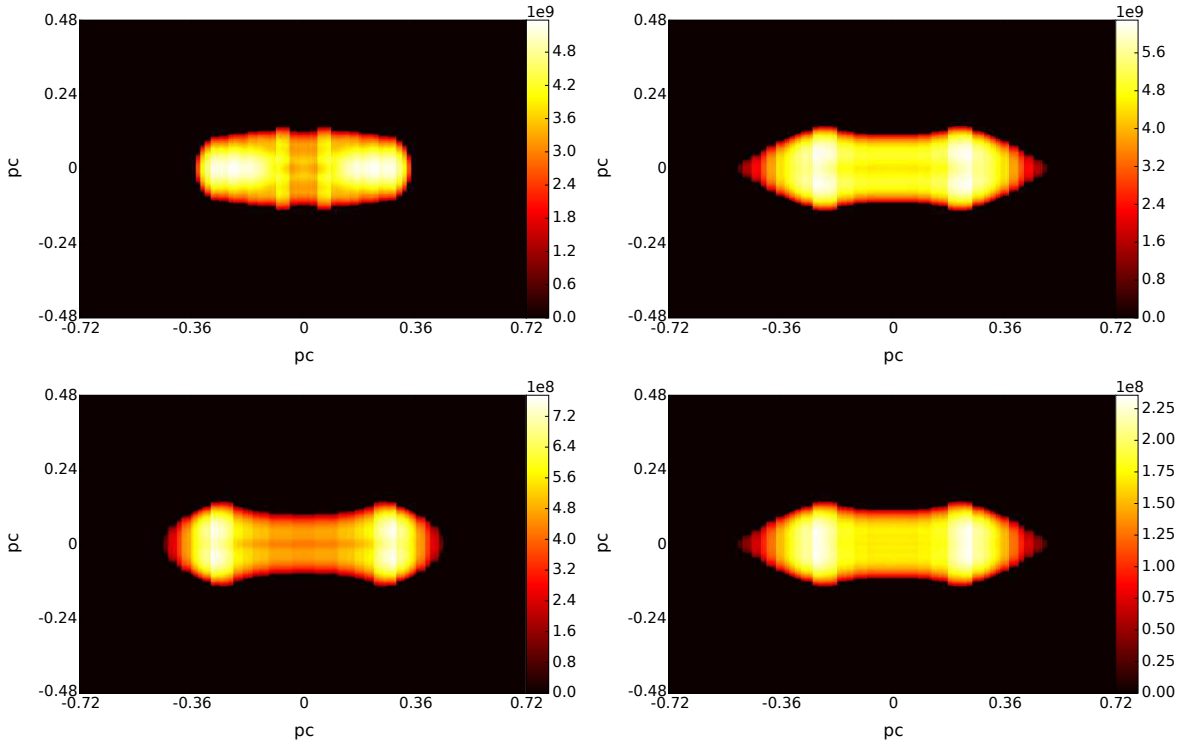

Figure 8. N_2H^+ column density maps for a *filamentary* core as seen edge-on for various sets of parameters. Top left is run 2, top right is run 3, bottom left is run 4 and bottom right is run 5. See Table 2 for details on the parameters of each run.

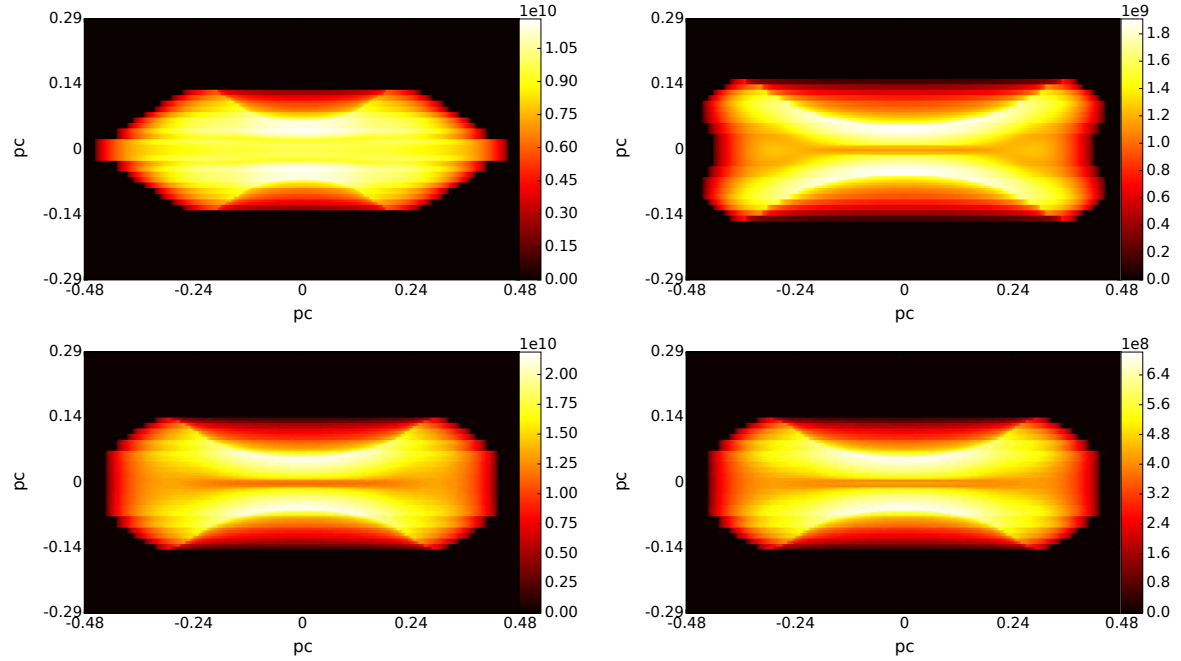

Figure 9. Same as in Figure 8 but for our *disk-like* models.

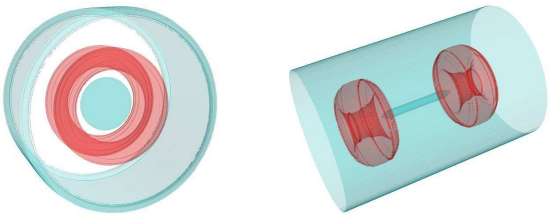

Figure 10. N_2H^+ 3D abundance plots for a disk-like (left) and a cylindrical (right) core. Isosurfaces are at 35% (blue shaded isosurfaces) and 90% (red shaded isosurfaces) of the maximum N_2H^+ abundance. The inner, low abundance disk will have a larger radius than that of the inner, low abundance cylinder and as a result the effect of depletion will be more severe in the column density map of a disk when it is observed edge-on.

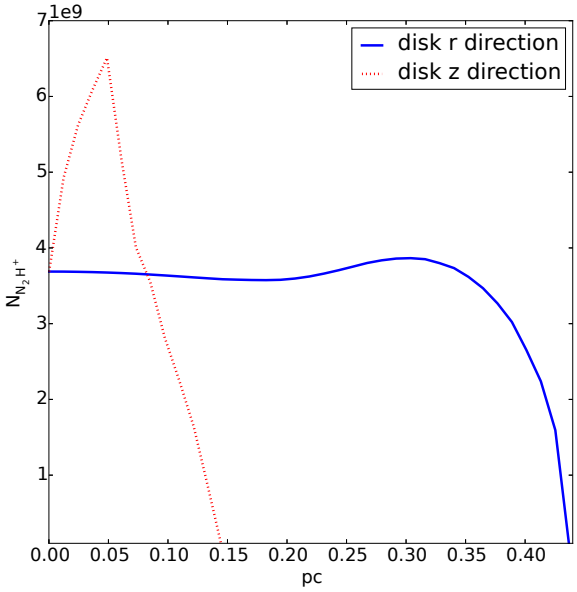

Figure 11. N_2H^+ column density profiles for a disk-like core. The gradient in the z direction from the peak to the centre of the disk-like core (dotted red line) is larger than that in the radial direction (solid blue line). As a result, a disk-like cores will not be observed as an empty ellipse when observed in N_2H^+.

than an ellipsoid resulting from the projection of a disk-like core. Thus, in order to have a recipe that probes the true 3D shape of a core, it is only meaningful to relate a parameter to the aspect ratio of the projected shape. That parameter can again be the parameter Δ as defined in § 3.1. Here, there is no need to make use of the parameter Δ_{σ^2} since the degeneracy between disk-like and spherical cores is broken by dust emission maps alone.

In order to compute the aspect ratio of the projection of core, we first define the contour that marks 50% of the maximum of the total column density. We then divide the lengths of the two principal axes determined by that contour. Thus, we define both the parameter Δ and the aspect ratio in a self-consistent manner.

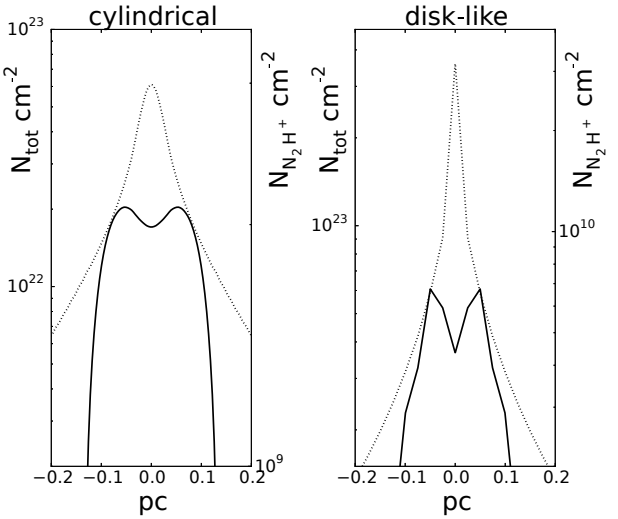

Figure 12. Left: Total column density radial profile (dotted line) and N_2H^+ column density radial profile (solid line) for a cylindrical core. Right: Total column density axial profile (dotted line) and N_2H^+ column density axial profile (solid line) for a disk-like core. A scenario in which the N_2H^+ filamentary structures have half the width from the filamentary structures observed in dust emission can more easily be realized if the intrinsic geometry of the core is disk-like rather than cylindrical.

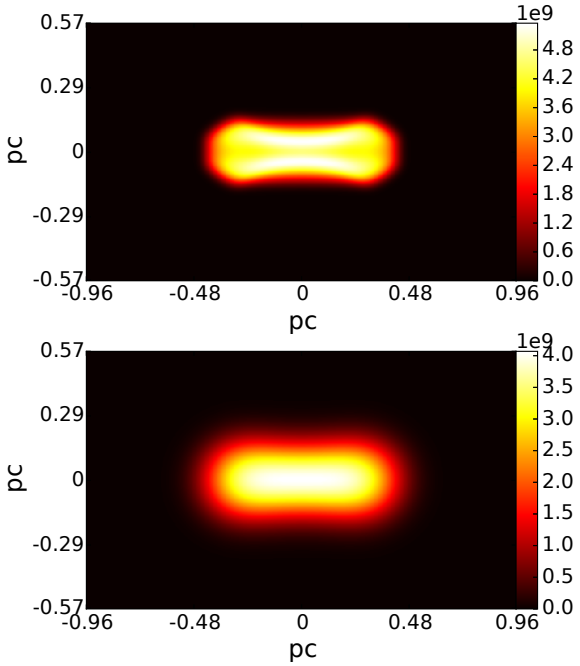

Figure 13. N_2H^+ column density maps for the disk-like core as observed edge-on convolved with two different beam sizes. In the upper panel the map was convolved with a beam size equal to that of CARMA and in the lower panel with *Herschel's* 350 μm beam size. At *Herschel's* resolution the "splitting effect" is not visible and N_2H^+ emission appears to peak at the z=0 plane.

Limited observational resolution can cause a projected object look rounder and can also change the apparent peakness of a molecular column density profile. Hence, for a molecule to be a good geometry tracer the value of the parameter Δ must be different for cylindrical and disk-like cores regardless of the resolution. To that end, results from simulations were convolved with a Gaussian filter assuming a beam size equal to 35" and a distance of 1 kpc. The value of the parameter Δ and the aspect ration were then computed at both instances. We have identified one molecule which satisfies these criteria.

In Figure 14 we show the parameter $\Delta_{\rm CN}$ as a function of the aspect ratio. If the true shape of the core is that of a disk (red shaded region in Figure 14), $\Delta_{\rm CN}$ is close to unity, especially for aspect ratios ≥ 0.6. In contrast, if the core is cylindrical (blue shaded region in Figure 14), the molecular column density profiles along both axes of the projected object are very centrally peaked and $\Delta \gg 1$. This is the case for aspect ratios from 0.2 to unity, although the greatest differences in the values of the parameter Δ are found if the projected objects have aspect ratios ≈ 0.6. In Figure 14 the upper boundaries of the shaded regions are obtained by considering the best possible resolution of the simulations. The value of Δ and the aspect ratio for different combinations of beam sizes and distances fall inside these shaded regions provided that the resolution is better than that obtained with a beam size of 35" and distance 1 kpc. The results presented here are obtained by considering the effective excitation density $\rm n_{eff}$ of CN although results obtained by considering the critical density $\rm n_{crit}$ of CN are in very good agreement.

The differences between cylindrical and disk-like cores seen in Figure 14 can be understood as follows. For cylindrical clouds, the molecular abundance of CN will be higher in a cylindrical shell just outside the innermost high-density thin cylinder. When such a core is seen at an offset from exactly edge-on, higher abundances will be integrated over a longer line of sight. As a result, the molecular column density will peak even more in the central region and the parameter Δ will increase. In contrast, for disk-like cores the path of integration gets shorter as the viewing angle changes from exactly edge-on to exactly face-on and therefore the value of Δ will be closer to unity.

4 DISCUSSION AND CONCLUSIONS

In the simulations presented here, the initial abundances of all chemical compounds were set to zero. In order to examine to what extent this approximation is unphysical, we have also considered a run in which the chemistry is left to evolve for 1 Myr at a uniform density of 10^3 cm^{-3} before collapse. We have confirmed that the abundances at a central density of 10^6cm^{-3} do not change significantly. However, as it has been pointed out by previous studies (Aikawa et al. 2001), if the pre-collapse phase lasts longer and/or is at a higher density, abundances will deviate more from the models without a pre-collapse phase.

The molecular column density maps presented in this paper are produced only from the portions of the cores where $\rm n_{tot} \geq n_{crit}$ and $\rm n_{tot} \geq n_{eff}$, where we considered the transitions corresponding to the lowest possible values for $\rm n_{crit}$ and $\rm n_{eff}$. These are the inner regions of the cores, away from the boundaries of the computational region. Furthermore, when defining Δ and Δ_{σ^2}, we have not included values of molecular column density that coincided with regions with total column density below a background value. We are thus confident that our results are not affected by the boundaries.

The disk-like and cylindrical cores as well as the spherical core are idealized shapes of what can be found in nature. Triaxial cores appear to be a better fit to observations in statistical studies although axisymmetric shapes are not ruled out (Tassis 2007). The *splitting effect* might not be visible in the same manner if we have a triaxial oblate spheroid instead of a disk-like geometry. The abundance of N_2H^+ will continue to probe the regions above and bellow the high-density region, but for an oblate spheroid the path of integration also gets smaller as we move along the short axis. Hence, for an oblate spheroid the higher abundance of N_2H^+ around the high-density region might be counterbalanced by the shorter path of integration. However, a scenario in which an oblate spheroid observed edge-on will split in 3 parallel elongated structures when seen in N_2H^+ can also be realized. In such a scenario, the middle structure will be seen due to the fact that N_2H^+ also probes the regions in front of and behind the depleted region. A dip might then be caused due to lower abundance and smaller integration path, and finally two elongated structures above and bellow the middle one will be seen, simply due to higher N_2H^+ abundance. In any case, the occurrence or not of the *splitting effect* for an oblate spheroid depends on its intrinsic aspect ratio and the interplay between N_2H^+ abundance and integration path.

What is more, the *splitting effect* will not be visible for cores in earlier evolutionary stages. For a disk-like core with central density $\sim 10^4$cm^{-3} only the innermost regions of the core will be visible in N_2H^+ since its effective density is of that order. Nonetheless, in case the *splitting effect* is observed in a manner similar to that presented in this paper, we can safely conclude that the intrinsic 3D shape of the core resembles a disk. Likewise, if a core appears filamentary in dust emission, the central density is of the order of $\sim 10^6$cm^{-3}, and is seen as two separate elliptical objects or as a broad continuous structure in a N_2H^+ column density map, we can conclude that its true shape is a cylinder. Finally, if the core is seen as a circularly symmetric object we can apply the face on method to determine the true shape of the core. We intend to return to the problem of triaxial cores with supplementary 3D simulations, including magnetic fields, and with a post-processing analysis of our result with a radiative transfer code in a future publication.

For projection angles such that our simulated cylindrical and disk-like core models are seen as ellipses or round objects the effect of depletion is not severe. As a result, both cores would appear centrally peaked in N_2H^+ emission, with $\Delta > 1$. In fact, at low resolution the N_2H^+ column density maps of the two cores would be qualitatively identical to their respective total column density maps. This is in agreement with the early survey of N_2H^+ emission from Lee et al. (2001) which had a large beam size (52").

Whether a molecule is a good geometry-tracer does not simply depend on which gas density better traces. It rather depends on its abundance distribution. The majority of molecules mentioned in § 3.2 have an abundance that peaks at a density of approximately a few times 10^4 cm^{-3} to

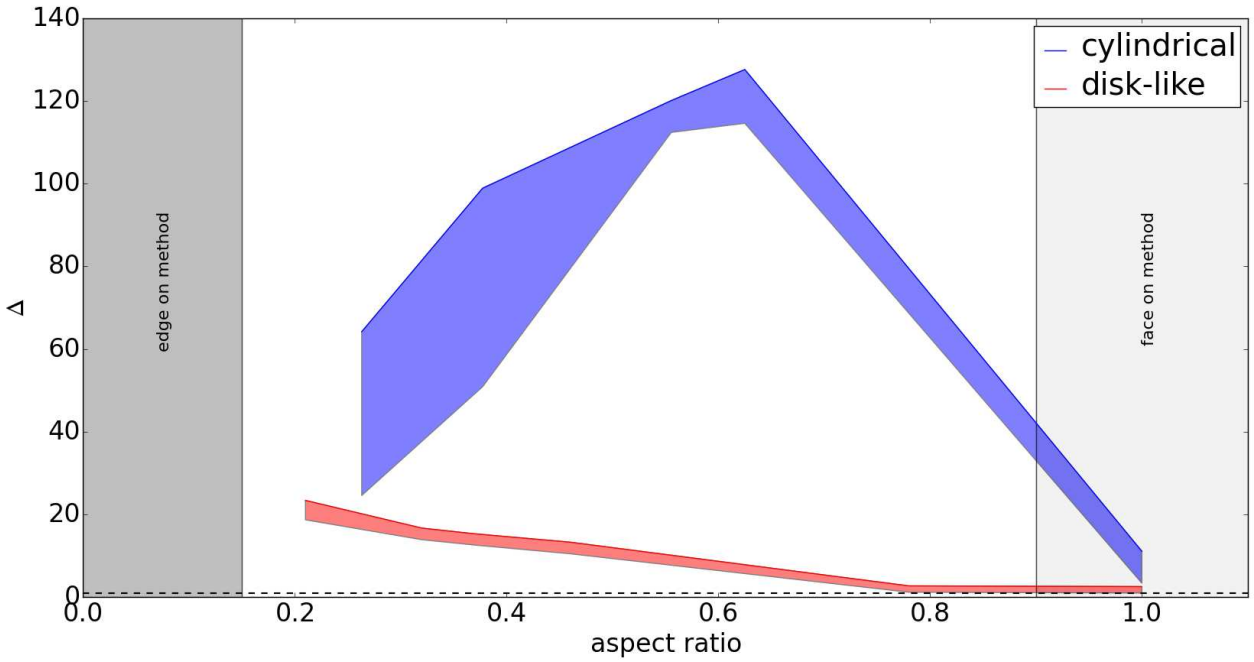

Figure 14. The parameter Δ of CN as a function of the aspect ratio for disk-like and cylindrical models (red and blue shaded regions respectively) for different resolutions. The horizontal dotted line is at $\Delta = 1$. Results are obtained considering $n_{\rm eff}$. For disk-like models $\Delta_{\rm CN}$ is close to unity, especially for aspect ratios ≥ 0.6 whereas for cylindrical models the value of the parameter Δ is much greater than 1 for all aspect ratios.

10^5 cm^{-3}. Their abundance then starts to decline for higher densities. In contrast, the abundance profile of CN has a plateau at slightly higher densities, although it too depletes at densities of the order of 10^6 cm^{-3}. If our cylindrical and disk-like cores are seen edge-on then N_2H^+ and NH_3 are proven good geometry traces because they exhibit the "right amount" of depletion. If, for the same projection angle, the cores were observed in CO then they would both appear as depletion holes with no qualitative differences amongst them.

For a random projection angle we derive the aspect ratio by dividing the major and the minor axis of the ellipse defined by the contour that marks 50% of the maximum of the total column density. This is the same contour we use to define the parameter Δ. We have confirmed that if we estimate the aspect ratio with a method based on the first and second moment of the flux density (e.g. Tassis et al. 2009) our results are not affected. However, for self-consistency, we recommend to define the aspect ratio and the parameter Δ in the same manner.

Our method can be summarized in the following steps:

• From dust continuum observations determine the aspect ratio of the core by defining a contour that marks 50% of the maximum of the total column density and dividing the two principal axes. The geometry-probing molecule that should be used is determined by the aspect ratio of the projected object.

• For aspect ratios ≤ 0.15 the geometry probing molecule will be N_2H^+ (and/or NH_3).

(i) If the core appears as two parallel filamentary structures in the N_2H^+ (NH_3) column density map then its true shape is that of a disk.

(ii) If it is seen as a continuous, broader than in dust emission, structure then it is cylindrical-like.

• When the aspect ratio of the core is in the range $0.15 \sim 0.9$ compute the parameter Δ for CN as defined in § 3.1.

(i) If the value of the parameter Δ is $\gg 1$ then the core is cylindrical-like.

(ii) If Δ is close to unity then the geometry of the core is disk-like.

• For well resolved, centrally peaked, circular objects with polar symmetry that can be face-on projections of disk-like or filamentary cores or projections of spherical cores calculate the parameters Δ_{σ^2} and Δ for OH (and/or CO, H_2CO) as defined in § 3.1.

(i) When both Δ_{σ^2} and Δ are close to unity the intrinsic shape of the core is disk-like.

(ii) If Δ is close to unity but $\Delta_{\sigma^2} \ll 1$ then the core is spherical.

(iii) If both Δ and $\Delta_{\sigma^2} \ll 1$ then the true shape of the core is cylindrical-like.

ACKNOWLEDGEMENTS

We thank G.V. Panopoulou, T. Mouschovias, V. Pavlidou, P. Goldsmith and N. Kylafis for useful suggestions and discussions. We also thank the anonymous referee for useful comments that helped improve this paper. The software

used in this work was in part developed by the DOE NNSA-ASC OASCR Flash Center at the University of Chicago. 3D plots were created using Mayavi2 (Ramachandran & Varoquaux 2012). For post processing our results we partly used yt analysis toolkit (Turk et al. 2011). K.T. and A.T. acknowledge support by FP7 through Marie Curie Career Integration Grant PCIG- GA-2011-293531 "SFOnset". A.T. and K.T. would like to acknowledge partial support from the EU FP7 Grant PIRSES-GA-2012-31578 "EuroCal". K.W.'s work was carried out at the Jet Propulsion Laboratory, California Institute of Technology, under a contract with the National Aeronautics and Space Administration. K.W. acknowledges support from the NASA Origins of Solar System Program. Usage of the Metropolis HPC Facility at the CCQCN of the University of Crete, supported by the European Union Seventh Framework Programme (FP7-REGPOT-2012-2013-1) under grant agreement no. 316165, is also acknowledged.

REFERENCES

Aikawa, Y., Ohashi, N., Inutsuka, S.-i., Herbst, E., & Takakuwa, S. 2001, ApJ, 552, 639
Aikawa, Y., Ohashi, N., & Herbst, E. 2003, ApJ, 593, 906
Arzoumanian, D., André, P., Didelon, P., et al. 2011, A&A, 529, L6
Ballesteros-Paredes, J., Klessen, R. S., & Vázquez-Semadeni, E. 2003, ApJ, 592, 188
Basu, S., & Ciolek, G. E. 2004, ApJL, 607, L39
Bergin, E. A., Alves, J., Huard, T., & Lada, C. J. 2002, ApJL, 570, L101
Boss, A. P., & Hartmann, L. W. 2001,ApJ, 562, 842
Ciolek, G. E., & Basu, S. 2006, ApJ, 652, 442
Curry, C. L. 2002, ApJ, 576, 849
Dapp, W. B., & Basu, S. 2009, MNRAS, 395, 1092
Dubey, A., Fisher, R., Graziani, C., et al. 2008, Numerical Modeling of Space Plasma Flows, 385, 145
Evans, N. J., II 1999, ARA&A, 37, 311
Fernández-López, M., Arce, H. G., Looney, L., et al. 2014, ApJL, 790, L19
Fryxell, B., Olson, K., Ricker, P., et al. 2000, ApJS, 131, 273
Gammie, C. F., Lin, Y.-T., Stone, J. M., & Ostriker, E. C. 2003, ApJ, 592, 203
Goldsmith, P. F., & Li, D. 2005, ApJ, 622, 938
Goodwin, S. P., Ward-Thompson, D., & Whitworth, A. P. 2002, MNRAS, 330, 769
Jones, C. E., & Basu, S. 2002, ApJ, 569, 280
Jones, C. E., Basu, S., & Dubinski, J. 2001, ApJ, 551, 387
Kainulainen, J., Hacar, A., Alves, J., et al. 2015, arXiv:1507.03742
Keto, E., Caselli, P., & Rawlings, J. 2015, MNRAS, 446, 3731
Könyves , V., André, P., Schneider, N., et al. 2013, Astronomische Nachrichten, 334, 908
Lee, C. W., Myers, P. C., & Tafalla, M. 2001, ApJS, 136, 703
Lee, K. I., Fernández-López, M., Storm, S., et al. 2014, ApJ, 797, 76
Li, P. S., Norman, M. L., Mac Low, M.-M., & Heitsch, F. 2004, ApJ, 605, 800
Li, D., & Goldsmith, P. F. 2012, ApJ, 756, 12
Lomax, O., Whitworth, A. P., & Cartwright, A. 2013, MNRAS, 436, 2680
Marchwinski, R. C., Pavel, M. D., & Clemens, D. P. 2012, ApJ, 755, 130
McElroy, D., Walsh, C., Markwick, A. J., et al. 2013, A&A, 550, AA36
Myers, P. C., Fuller, G. A., Goodman, A. A., & Benson, P. J. 1991, ApJ, 376, 561
Nielbock, M., Launhardt, R., Steinacker, J., et al. 2012, A&A, 547, A11
Pagani, L., Bacmann, A., Cabrit, S., & Vastel, C. 2007, A&A, 467, 179
Pagani, L., Bacmann, A., Cabrit, S., & Vastel, C. 2007, Molecules in Space and Laboratory, 32
Poidevin, F., Ade, P. A. R., Angile, F. E., et al. 2014, ApJ, 791, 43
Ramachandran, P., & Varoquaux, G. 2012, Astrophysics Source Code Library, 1205.008
Ryden, B. S. 1996, Bulletin of the American Astronomical Society, 28, 886
Sadavoy, S. I., Di Francesco, J., Bontemps, S., et al. 2010, ApJ, 710, 1247
Shirley, Y. L. 2015, PASP, 127, 299
Steinacker, J., Bacmann, A., Henning, T., Klessen, R., & Stickel, M. 2005, A&A, 434, 167
Storm, S., Mundy, L. G., Fernández-López, M., et al. 2014, ApJ, 794, 165
Sugitani, K., Nakamura, F., Watanabe, M., et al. 2011, ApJ, 734, 63
Tafalla, M., Myers, P. C., Caselli, P., Walmsley, C. M., & Comito, C. 2002, ApJ, 569, 815
Tassis, K. 2007, MNRAS, 379, L50
Tassis, K., Dowell, C. D., Hildebrand, R. H., Kirby, L., & Vaillancourt, J. E. 2009, MNRAS, 399, 1681
Tassis, K., Willacy, K., Yorke, H. W., & Turner, N. J. 2012, ApJ, 754, 6 & Vaillancourt, J. E. 2009, MNRAS, 399, 1681
Tassis, K., Willacy, K., Yorke, H. W., & Turner, N. J. 2012, ApJ, 753, 29
Tritsis, A., Panopoulou, G. V., Mouschovias, T. C., Tassis, K., & Pavlidou, V. 2015, MNRAS, 451, 4384
Turk, M. J., Smith, B. D., Oishi, J. S., et al. 2011, ApJS, 192, 9

Chapter 6

Bridging the gap between theory and observations

In order to improve and better benchmark our method for probing the intrinsic shape of cores we also have to properly account for radiative transfer effects. To this end, we have developed a state-of-the-art line radiative transfer code, called PyRaTE. PyRaTE (Python Radiative Transfer Emission) is a non-LTE code and has two main advantages over the majority of existing radiative transfer codes. Firstly, the population densities are computed with variations in all physical parameters (i.e. density, molecular abundance, temperature and velocity) taken into account. Secondly, we have developed easy-to-use interfaces for importing data from simulations and exporting the results in formats directly comparable to observations as well as a number of auxiliary modules to facilitate this comparison. With PyRaTE we will not only be able to improve our method, but since cores with different intrinsic 3D shapes are expected to have distinct velocity fields, we will also be able to incorporate the additional information from the spectral line profiles in our analysis.

Mon. Not. R. Astron. Soc. **000**, 000–000 (0000) Printed 12 May 2017 (MN LATEX style file v2.2)

Python Radiative Transfer Emission code (PyRaTE): non-LTE spectral lines simulations

A. Tritsis[1,2], H.Yorke[3,4], K. Tassis[1,2]
[1] *Department of Physics and ITCP ⋆, University of Crete, PO Box 2208, 71003 Heraklion, Greece*
[2] *IESL, Foundation for Research and Technology-Hellas, PO Box 1527, 71110 Heraklion, Crete, Greece*
[3] *Jet Propulsion Laboratory, California Institute of Technology, Pasadena, CA 91109, USA*
[4] *SOFIA Science Center, NASA Ames Research Center, 94035 Moffett Field, USA*

12 May 2017

ABSTRACT

We describe PyRaTE, a new, freely available, non-local thermodynamic equilibrium (non-LTE) line radiative transfer code developed specifically for post-processing astrochemical simulations. Population densities are estimated using the escape probability method. When computing the escape probability, the optical depth is calculated towards all directions with density, molecular abundance, temperature and velocity variations all taken into account. A very easy-to-use interface, capable of importing data from simulations outputs performed with all major astrophysical codes, is also developed. The code is written in Python using an embarrassingly parallel strategy and can handle all geometries and projection angles.

Key words: Physical data and processes: Radiative transfer – ISM: clouds – ISM: molecules – methods: numerical

1 INTRODUCTION

Recent advancements in computer technologies, have allowed for simulations of multiphysics astrophysical problems to flourish. Numerical codes and methods are becoming increasingly sophisticated and accurate (Krumholz et al. 2007; Mocz et al. 2014a; Mocz et al.2014b; Schaal et al. 2015; Hopkins 2015; Hopkins & Raives 2016). Astrochemical simulations in which the chemical and dynamical evolution of astrophysical objects are coupled, follow in the same direction (Tassis et al. 2012a; Tassis et al. 2012b; Clark et al. 2013; Motoyama et al. 2015; Walch et al. 2015; Tritsis et al. 2016; Seifried & Walch 2016).

Observational astrophysics is also advancing rapidly. New, very high angular and spectral resolution data obtained with telescopes such as ALMA can reveal features of astrophysical objects in unprecedented detail. Furthermore, such observations offer a unique opportunity to distinguish between different theoretical models. To do so, a connection between theoretical results and observations is essential. Since observationally our full range of knowledge about astrophysical objects is obtained through the study of electromagnetic radiation, a direct comparison requires post-processing simulation outputs with radiative transfer (RT) codes.

Post-processing astrochemical simulations with line radiative transfer codes is not a trivial task. Local thermodynamic equilibrium (LTE) is not attained in many astrophysical problems and the population densities of the species under consideration have to be computed in non-local thermodynamic equilibrium (non-LTE). The majority of the existing radiative transfer codes (Keto 1990; Keto et al. 2004; Hogerheijde & van der Tak 2000; van der Tak et al. 2007; Brinch & Hogerheijde 2010; Dullemond 2012) do compute the population densities in non-LTE. However, the validity of certain approximations and assumptions, as for example is homogeneity and the calculation of optical depth from average quantities, may not always be appropriate. Furthermore, restrictions in the number of dimensions existing RT codes can handle and the fact that the interfaces are not always particularly practical can cause confusion and limit the number of choices a user has.

In this paper we describe the PyRaTE (Python Radiative Transfer Emission) code. PyRaTE is a user-friendly, embarrassingly parallel, modular, non-LTE radiative transfer code, fully written in Python[1]. It makes use of the yt analysis toolkit (Turk et al. 2011) which can handle simu-

⋆ Institute for Theoretical and Computational Physics, formerly Institute for Plasma Physics

[1] `https://www.python.org/`

lation outputs performed with all major codes[2] as well as generic adaptive mesh refinement (AMR) and array data. As a result, exporting data from astrochemical simulations requires no effort. Moreover, PyRaTE can handle all geometries and all projection angles. In its current version, the code is focused on star formation and molecular cloud related problems. However, it can be easily modified so that it can be used for any astrophysical problem.

In section § 2 we describe the formalism of radiative transfer used, the numerical methods, we compare our results with those from RADEX (van der Tak et al. 2007) and with analytical solutions, and we outline the parallelism strategy we follow and the design of the code. In § 3 we use numerical simulations presented in a previous study to demonstrate the code's capabilities. A summary of this work and future goals are given in § 4.

2 CODE DESIGN

2.1 Basic formalism

Integration of the non-relativistic, time-independent equation of radiation transfer between two grid points i and $i+1$ yields:

$$I_{i+1} = \frac{(e^{-\tau^C_{i+1}} - p)I_i + pS^L_i + qS^L_{i+1} + S^k}{1+q} \tag{1}$$

(Yorke 1986) where the contributions of line and dust continuum emission, denoted with the superscripts L and C respectively, are considered separately. In Equation 1 I is the radiative intensity, S^L is the source function for line emission and τ^C is the optical depth for continuum emission. The quantities q, p and S^k are given by:

$$q = \frac{\tau^L_{i+1}}{1 + e^{-\tau^L_{i+1}}} \tag{2}$$

$$p = q(e^{-\tau^L_{i+1} - \tau^C_{i+1}}) \tag{3}$$

$$S^k = e^{-\tau^C_{i+1}} \int_i^{i+1} \kappa^C S^C e^{\int_i^s \kappa^C(s')ds'} ds \tag{4}$$

where S^C is the source function for dust continuum emission and τ^L_{i+1} is the optical depth of the line:

$$\tau^L_{i+1} = \int_i^{i+1} \kappa^L(s) ds \tag{5}$$

In Equations 4 and 5 s is the length along the line-of-sight (LOS), κ^C is the extinction coefficient for continuum emission, computed from Mie theory, and κ^L is the line extinction coefficient:

$$\kappa^L = n_l B_{lu} \frac{h\nu_0}{4\pi} \big[1 - \frac{n_u g_l}{n_l g_u}\big] \varphi(\nu) \tag{6}$$

(Mihalas 1978). In the latter equation, g is the statistical weight, B is the Einstein B coefficient, ν_0 is the rest frequency of the line, h is the Planck constant, n is the population density of the upper and lower level (denoted with the subscripts u and l) and $\varphi(\nu)$ is the normalized profile function such that $\int \varphi(\nu) d\nu = 1$. As a result, I can be computed by calculating the quantities that appear in Equations 2 through 6, inserting them in Equation 1 and performing the ray-tracing.

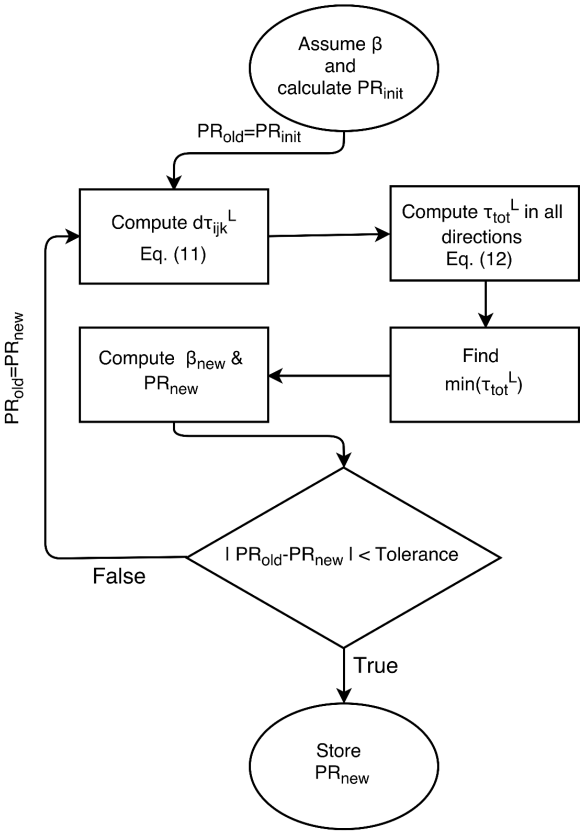

Figure 1. Flow chart of the algorithm used to compute the population ratio (PR) at each grid point. The same procedure is followed for all grid points.

2.2 Dust model

We use a three component dust grain model consisting of amorphous carbon grains, silicate grains and dirty ice (i.e. water, ammonia and carbon particles) coated silicate grains. Our grain model is that of Preibisch et al. (1993) which is appropriate for dense molecular cloud conditions. However, the amount of dust has been reduced to be compatible with the calculations performed by Pollack et al.(1985). The sublimation temperature of each component is $\sim$ 2000, 1500 and 125 K respectively. All components are assumed to be spherical with sizes $\sim$ 10 nm for the carbon, $\sim$ 50 nm for the silicate and $\sim$ 60 nm for the dirty ice coated silicate grains.

The data for the efficiency factor for extinction Q^{ext} and the albedo α ($\alpha = Q^{sca}/Q^{ext}$, where Q^{sca} is the efficiency factor for scattering) are stored in the code in tabulated form. Based on the desired frequency, linear interpolation is applied through the data for each of the dust components. The extinction coefficient for dust emission is then computed

[2] For a full list of the codes that yt and thus PyRaTE can handle see `http://yt-project.org/docs/dev/examining/loading_data.html`

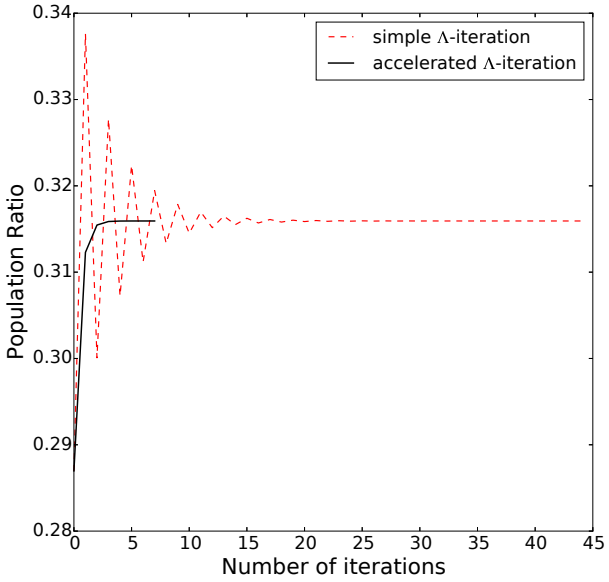

Figure 2. The black solid line shows the performance of the accelerated Λ-iteration algorithm currently in use for calculating the population ratio. The red dashed line show results using a simple Λ-iteration. The current algorithm converges in just a few iterations.

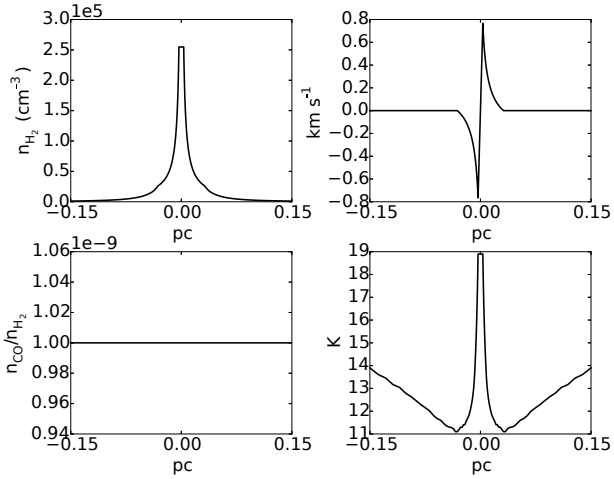

Figure 3. Parameters of the spherical model adopted from RADEX's test problem web page to investigate the validity of the algorithm developed here to compute the population ratio. In the upper left panel we plot the density, in the upper right the velocity, in lower left the molecular abundance and in the lower right the temperature.

as:

$$\kappa^C = \sum_{d=1}^{3} n_d Q_d^{ext} \pi r_d^2 \tag{7}$$

where n_d is the number density of each grain component which is in turn determined from the temperature and density of each grid point. The source function for continuum emission is computed as the sum of the thermal emission, weighted over the albedo, and the contribution from scattering. For the interpolation we use a standard SCIPY routine[3]. Higher order interpolation through the data can also be used by changing a keyword in the interpolating function. Finally, by adjusting this dust grain model, PyRATE can be modified to suit a variety of astrophysical problems.

2.3 Computing the population ratio (non-LTE)

We consider a simple two level system. Then, the rate of change of the population density in the upper level will be the sum of the excitation (absorption and collisional excitation) and de-excitation (induced emission, spontaneous emission and collisional de-excitation) processes:

$$\frac{dn_u}{dt} = -n_u B_{ul} u_\nu + n_l B_{lu} u_\nu - n_u A_{ul} + n_l n_{H_2} C_{lu} - n_u n_{H_2} C_{ul} \tag{8}$$

In Equation 8, u_ν is the radiative energy density, C_{ul} and C_{lu} are respectively the de-excitation and excitation coefficients due to collisions, n_{H_2} is the number density of the H_2 molecule which is the dominant collisional partner, and A_{ul} is the Einstein A coefficient for spontaneous emission. In order to compute the first two terms on the right hand side of Equation 8 a priori knowledge of the radiation field is required. As a result, the entire problem has to be solved iteratively, a computationally very demanding task. An alternative solution to the problem is to approximate u_ν as $S_\nu^L(1-\beta)$ where β is the probability of a photon escaping the cloud. Following the same reasoning, the radiation field due to external photons penetrating the cloud will be, $S_\nu\beta$.

If we now further assume statistical equilibrium $\frac{dn_u}{dt} = 0$, divide Equation 8 with n_l and rearrange we can write the population ratio as:

$$\frac{n_u}{n_l} = \frac{\frac{g_u}{g_l} e^{-E/K_B T_{i'j'k'}}}{1 + \frac{A_{ul}}{n^{H_2}_{i'j'k'} C_{ul}} \beta_{i'j'k'}} \tag{9}$$

where K_B is the Boltzmann constant, $T_{i'j'k'}$ and $n^{H_2}_{i'j'k'}$ are respectively the temperature and density at a grid point $(i'j'k')$ and E is the energy of the transition. To obtain Equation 9 we also made use of the fact that the collisional excitation and de-excitation coefficients are related as:

$$C_{lu} = C_{ul} \frac{g_u}{g_l} e^{-E/K_B T} \tag{10}$$

In order to determine the population densities we also have to compute the escape probability at every grid point. To do so, we use an accelerated Λ-iteration described in the following steps:

(i) First, we assume an initial value for the escape probability and calculate an initial population ratio for grid point $(i'j'k')$ from Equation 9.

(ii) Based on that initial guess for the population ratio, the infinitesimal optical depth of the line is computed at all grid points as:

$$d\tau^L_{ijk} = \frac{c^3}{8\pi\nu_0^3} \frac{A_{ul} n^{molec}_{ijk}}{\Delta v^{th}_{ijk}} \left(\frac{g_u}{g_l} n_l - n_u\right) ds \tag{11}$$

[3] `http://docs.scipy.org/doc/scipy/reference/interpolate.html`

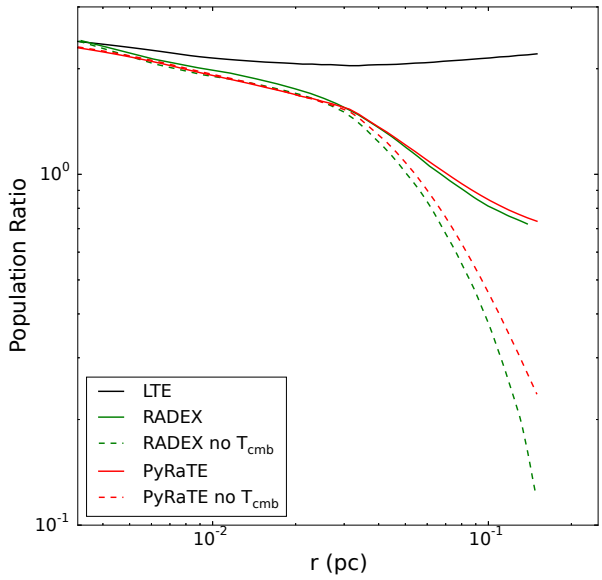

Figure 4. Comparison of the population ratio obtained with PyRaTE (solid red and dashed red lines) and RADEX (solid and dash-dotted green lines). Results obtained with the two codes are similar. As a reference, the populations computed in the LTE approximation are overplotted with a solid black line.

(van der Tak et al. 2007). In Equation 11, c is the speed of light, n_{ijk}^{molec} is the number density of the molecule at grid point (i, j, k) and Δv_{th} is the thermal width of the line.

(iii) Next, the total optical depth is computed as the sum of the infinitesimal optical depth of the grid points for which their absolute velocity difference with grid point $(i'j'k')$ is smaller than the thermal width.

(iv) The algorithm then searches the direction for which the optical depth of the line is minimum. For example, the minimum optical depth for a 3D cartesian grid is computed from six sums as:

$$\tau^L_{i'j'k'} = \min\Bigg(\sum_{i=i'+1}^{A} d\tau^L_{ijk}[\mid v_{i'j'k'} - v_{ij'k'} \mid < \Delta v^{th}_{ij'k'}], \sum_{i=i'-1}^{0} d\tau^L_{ijk}[\mid v_{i'j'k'} - v_{ij'k'} \mid < \Delta v^{th}_{ij'k'}], \sum_{j=j'+1}^{B} d\tau^L_{ijk}[\mid v_{i'j'k'} - v_{i'jk'} \mid < \Delta v^{th}_{i'jk'}], \sum_{j=j'-1}^{0} d\tau^L_{ijk}[\mid v_{i'j'k'} - v_{i'jk'} \mid < \Delta v^{th}_{i'jk'}], \sum_{k=k'+1}^{C} d\tau^L_{ijk}[\mid v_{i'j'k'} - v_{i'j'k} \mid < \Delta v^{th}_{i'j'k}], \sum_{k=k'-1}^{0} d\tau^L_{ijk}[\mid v_{i'j'k'} - v_{i'j'k} \mid < \Delta v^{th}_{i'j'k}] \Bigg) \quad (12)$$

where A, B and C are the sizes of the grid in the i, j and k directions, respectively.

(v) With that optical depth, a new escape probability and population ratio are computed.

(vi) If the absolute difference of the previously and newly computed population ratios is smaller than some tolerance, then the value is stored in computer memory. If this condition is not satisfied steps (ii) through (vi) are repeated until the population ratio converges to a value.

A flow chart of the algorithm that summarizes these steps is shown in Figure 1. With this procedure, density, temperature, velocity and molecular abundance variations are all taken into account. For a multilevel species, the full system of equations arising from statistical equilibrium has to be solved. A workaround can be to use the sum of collisional rates in the denominator of equation 9, and is what PyRaTE does at the moment. The proper treatment of the system of equations, following the same methodology described above, is soon to be added to the code. After the population densities have been computed, the line source function is calculated as:

$$S^L = \frac{2h\nu^3}{c^2} \frac{1}{\frac{n_l g_u}{n_u g_l} - 1} \quad (13)$$

The described procedure is a simple Λ-iteration. To increase the computational speed we implement an accelerated scheme. In each successive iteration, the new population ratio is the mean of the two previously computed values instead of just the previously computed value. Furthermore, since the escape probability is not expected to vary much between adjacent grid points, the result for one grid point is used as the initial guess for the neighbouring cell. Since for species with low critical densities the above procedure is redundant, the algorithm first checks if the second term in the denominator of Equation 9 is much less than unity. If so, the population ratio is computed from the Boltzmann distribution. In Figure 2 we show an example where the population ratio for a grid point is calculated using simple (red dashed line) and accelerated (black solid line) Λ-iterations. In the latter case the algorithm converges within a few iterations. For an 1D isothermal spherical collapse model with 304 grid points, a tolerance of 10^{-7} and an optically thick ^{12}CO molecule the algorithm converges in ~ 0.9 seconds in one central processing unit (CPU).

2.4 Benchmarking

In order to test the validity of the algorithm developed we compare our results with those of RADEX (van der Tak et al. 2007). To do so, we adopt the set-up of a test-problem of RADEX[4], the parameters of which are shown in Figure 3. In this model, the abundance of HCO^+ is low ($\sim 10^{-9}$), so that the emission is optically thin, and the radial profiles of the physical parameters were created based on the model by Shu (1977). Results of the population ratio obtained from both codes, with and without considering the contribution from the cosmic background radiation field, are shown in

[4] `https://www.strw.leidenuniv.nl/astrochem/radtrans/`

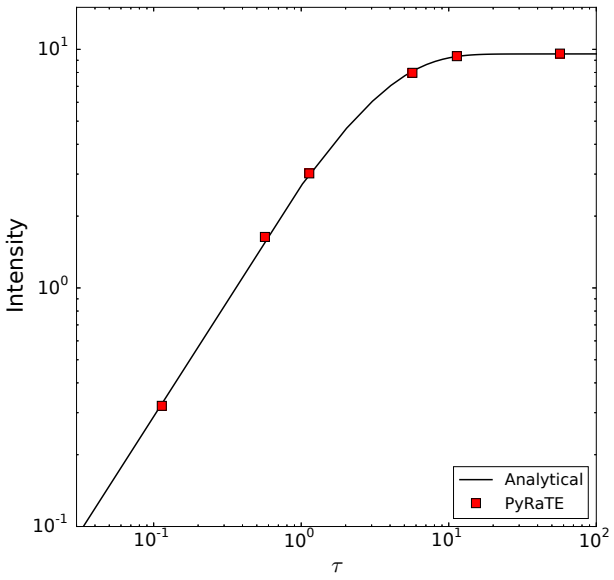

Figure 5. The intensity at the centre of the line as a function of the "mean" optical depth, as this is defined in Kylafis (1983). With the solid black lines we plot the results from the analytical solution and with the red squares the results from the code. The intensity is plotted in units of $h\nu^3/c^2$.

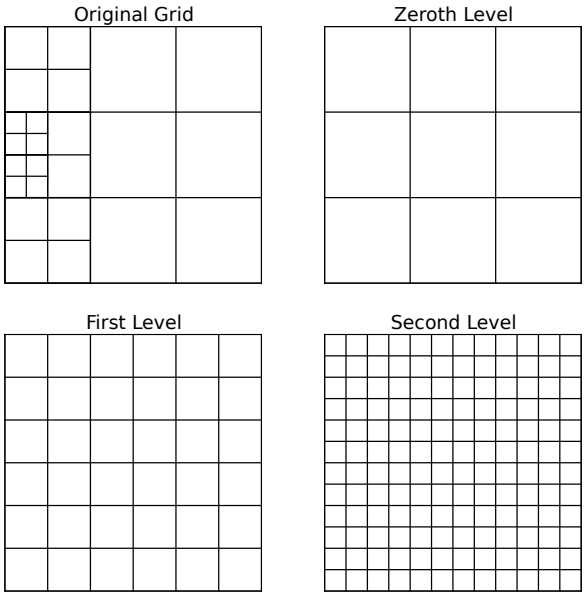

Figure 6. Treatment of AMR simulation outputs. Depending on the desired resolution, from the original AMR grid, a new uniform grid is created. When the resolution of the maximum level of refinement is selected, new grid points are created with values equal to the one of the grid point of the parent level.

Figure 4 and are very similar. The minimum value of the escape probability computed with PyRaTE during the Λ-iterations for all grid points was ~ 0.97, i.e. very close to unity. Thus, our algorithm correctly reproduces the fact that the emission is optically thin.

To further test the developed algorithms we compare results from PyRaTE against the analytical solutions derived in Kylafis (1983) for an one dimensional problem. In this problem, the velocity field is of the form $\vec{v} = (v_0/L)z\hat{k}$ and the temperature, abundance and density are uniform everywhere. In Figure 5 we show the intensity at the centre of the line as this is calculated from the analytical expressions (solid black line) and numerically (red squares) as a function of the "mean" optical depth defined in Kylafis (1983). Results from the code are in perfect agreement with the analytical method.

2.5 Loading data and constructing the grid

Data from astrochemical simulations and from files containing molecular data[5] are initially loaded into the code and stored in computer memory in tabulated form. These include the mass density, the abundance of the molecule under consideration, the Einstein coefficients, collisional excitation/de-excitation coefficients, the dimensions of the grid and velocities in all directions. Magnetic fields for Zeeman splitting measurements will also be included in a future version.

[5] Molecular data are taken from the Leiden Atomic and Molecular Database (Schöier et al. 2005) `http://home.strw.leidenuniv.nl/~moldata/`

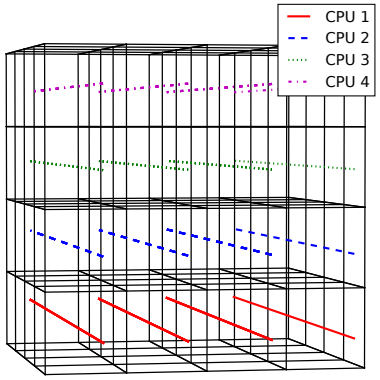

Figure 7. Strategy followed to parallelize the algorithms in our code. During ray tracing each processor is responsible only for a set of rays (coloured lines) passing through the computational region.

2.6 Parallelization

When loading data we assume spherical symmetry for 1D simulation outputs, plane and axial symmetries for 2D simulation outputs in cylindrical geometry and no symmetries for 3D simulations. These symmetries are accounted for in our calculations. However, the module responsible for exporting simulation data can be easily modified such that the desired symmetries and velocity conventions are followed.

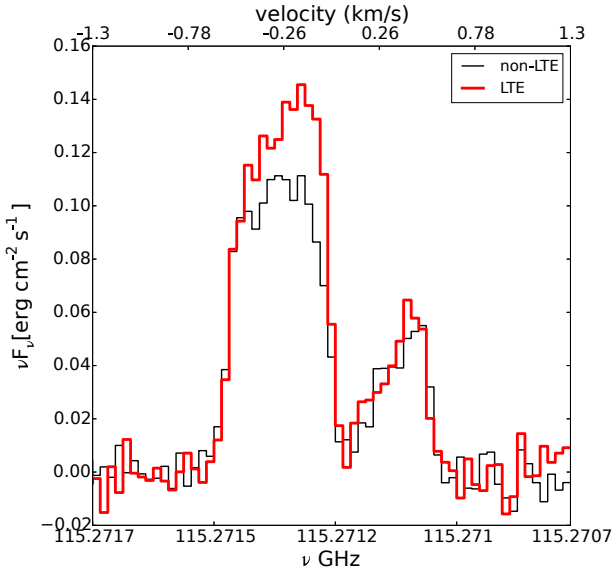

Figure 8. ^{12}CO (J = 1 - 0) emission line from a ray passing through the centre of a simulated spherical core under the LTE approximation (bold red line) and with non-LTE (black line). Gaussian noise with a signal-to-noise ratio of ~ 5 was added to the lines. The code correctly reproduces the expected inverse P-Cygni line profile.

Where necessary, volume rendering is performed simultaneously with ray tracing. Throughout the code, we use cgs units. Velocities with a minus sign represent motions towards the observer and vice versa. All other conventions followed in the code (e.g. conversion of frequencies to velocities) are consistent with the ones followed in radio astronomy.

Simulation outputs performed both in adaptive mesh refinement (AMR) and in uniform grids are supported. However, AMR grids are re-sampled into uniform grids based on the resolution of a refinement level. In the upper left panel of Figure 6 we show an example of an AMR grid with two levels of refinement. In the upper right, lower left and lower right panels we show the resulting grids constructed from the original grid, based on the zeroth, first and second level of refinement respectively. The values of additional grid points created in the lower panels of Figure 6 have the same values as the ones in the parent level. This treatment has the advantage of simplifying the algorithms and making them easy to read and modify. However, adding more grid points can substantially increase the computational time, especially for AMR simulations with many levels of refinement. In a future version we plan to upgrade the treatment of AMR grids.

In order to reduce computational time we have parallelized the majority of the code's modules using an embarrassingly parallel strategy. In Figure 7 we show an example of a 3D grid in which ray tracing is performed on four CPUs. Each CPU is responsible only for a set of rays (coloured lines in Figure 7). Similarly, in the modules computing the population ratios, the grid is split over the number of available processors and is then reconstructed. Given this strategy the code is linearly scalable. PyRaTE uses the package MPI4PY [6] which provides functions and bindings for the Message Passing Interface (MPI) and which can be easily installed alongside YT.

2.7 Auxiliary modules

A number of modules are available for pre-processing the simulation data and post-processing the results after ray-tracing is performed. The user has the option to add micro-turbulent broadening:

$$\Delta v_{tot} = \sqrt{\Delta v_{turb}^2 + \Delta v_{th}^2} \tag{14}$$

where Δv_{th} is the thermal linewidth and Δv_{turb} may be a constant number for all grid points or random numbers drawn from a flat or a Gaussian distribution. Additional modules also exists for debugging purposes and for creating simple models so there is no need for a priori astrochemical simulations.

To facilitate comparison with observations the user has a number of options. Gaussian noise can be added to spectral lines, based on a user-defined signal-to-noise ratio (SNR) and emission maps can be convolved with Gaussian filters based on some desired distance and telescope's beam size. Spectral lines can be plotted in antenna temperature, mJy or in cgs units. Furthermore, frequencies can be binned to match the spectral resolution of observations. The resulting output format of PyRaTE is equivalent to a position-position-velocity (PPV) cube from observations which can also be saved in FITS format for further analysis. Options for creating integrated emission maps are also available.

3 TEST CASES

The numerical simulations used to demonstrate PyRaTE's capabilities were performed with the astrophysical code FLASH4.0.1 (Fryxell et al. 2000, Dubey et al. 2008) and were described in detail in Tritsis et al. (2016). Here we give a brief overview of these calculations. In Tritsis et al. (2016) we employed hydrodynamic simulations combined with a non-equilibrium chemical modelling consisting of 214 gas-phase and 82 dust grain species. We considered three intrinsic geometries; spherical, cylindrical/filamentary and disk-like. The initial number density was 10^3 cm^{-3} and the temperature was constant and equal to 10 K.

In Figure 8 we show a ^{12}CO (J = 1 - 0) emission line from a LOS threading the middle of our spherical core. With the red line we plot our results assuming LTE and the black line non-LTE calculations. Random, gaussian noise was added to the line with a signal-to-noise ratio (SNR) of ~ 5. PyRaTE correctly reproduces the inverse P-Cygni line profile characteristic of infall motions (Evans 1999). The emission line is doubled peaked with the blue component being stronger due to absorption along the LOS. Furthermore, the line profile changes depending on whether LTE is assumed. Since in non-LTE we expect that the upper level will be less populated than in LTE, the source function of the line, and thus the intensity, will decrease. This feature is also clearly seen in Figure 8, especially for the blue shifted

[6] `https://pypi.python.org/pypi/mpi4py`

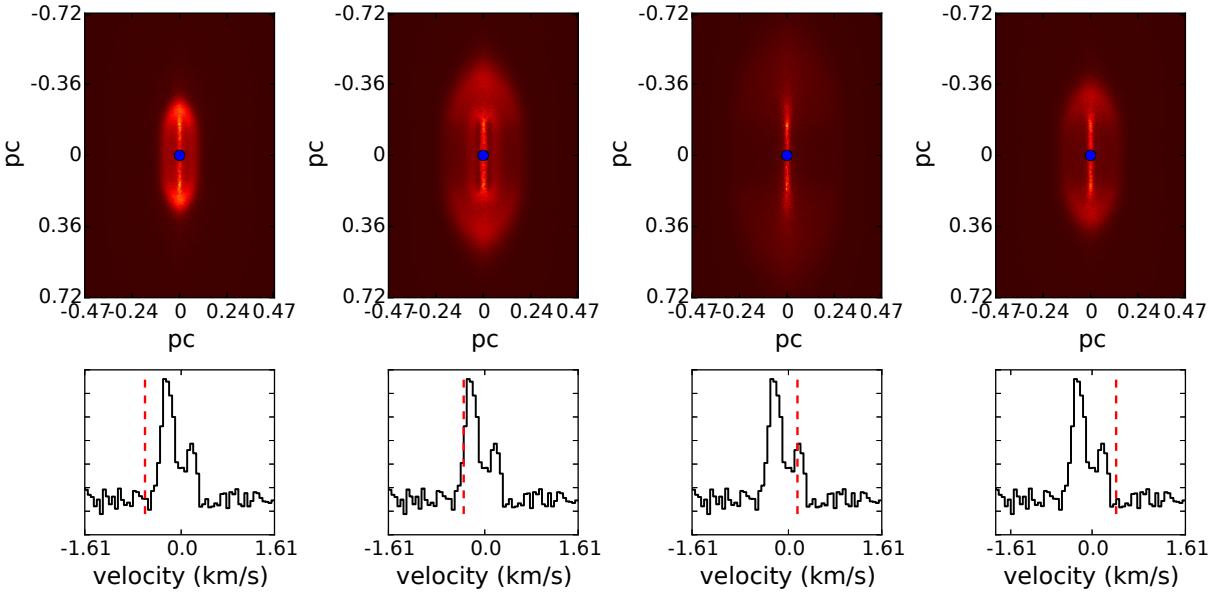

Figure 9. An isothermal cylinder collapsing as seen in four velocity slices (upper row). The lower row shows the spectrum from a LOS passing through the centre of the map (blue points in upper row) while the red line traces the velocity of each slice map.

component of the line. Furthermore, from Figure 8 it can be seen that the line profile changes depending on whether LTE is assumed. That is due to the velocity profile. The velocity differences between the centre of the core and the outer parts are larger than the thermal width of the line. Consequently, the total optical depth decreases, the escape probability increases and CO is only subthermally excited. However, if we were to "observe" the two lines, taking resolution restrictions into account, both profiles could probably be fitted by two Gaussian functions.

In Figure 9 we show four velocity slices from the collapse of a simulated isothermal cylindrical core model as seen in N_2H^+. The core is observed such that its axis of symmetry is perpendicular to the LOS (edge-on). In the upper panel we plot the emission map in each velocity slice and in the lower panel a spectral line (black line) threading the centre of the map (blue points in the upper panels). The red line in the lower panel traces the velocity shown in the upper panel.

4 SUMMARY

Radiative transfer is essential when comparing results from astrochemical simulations with radio observations. To this end, we have developed an easy-to-use non-LTE line radiative transfer code. The code can be used to post-process results from astrochemical simulations performed with all major astrophysical codes and can handle all geometries and projection angles. The population densities are computed using the escape probability method with variations in density, molecular abundance, temperature and velocities taken into account.

Compared to existing radiative transfer codes the populations densities in PyRATE are *not* computed from average quantities and velocity variations are taken into account. It's simple interfaces both for importing and exporting data and the fact that it is written in Python make the code easy-to-use, flexible and capable of producing publication quality figures effortlessly.

In a future version we plan to include a full treatment of the Stokes parameters in our code. Thus, simulations of the polarization of spectral line emission will also became possible. The algorithms for ray-tracing and for computing the population densities will continue to be developed both in terms of performance and accuracy. We think that PyRATE can be proven an important tool in the effort of connecting theory with observations.

ACKNOWLEDGEMENTS

We thank N. Kylafis for useful comments and discussions. The software used in this work was in part developed by the DOE NNSA-ASC OASCR Flash Center at the University of Chicago. For post processing our results we partly used yt analysis toolkit (Turk et al. 2011). K.T. and A.T. acknowledge support by FP7 through Marie Curie Career Integration Grant PCIG- GA-2011-293531 "SFOnset". A.T. and K.T. would like to acknowledge partial support from the EU FP7 Grant PIRSES-GA-2012-31578 "EuroCal". Usage of the Metropolis HPC Facility at the CCQCN of the University of Crete, supported by the European Union Seventh Framework Programme (FP7-REGPOT-2012-2013-1) under grant agreement no. 316165, is also acknowledged.

REFERENCES

Brinch, C., & Hogerheijde, M. R. 2010, A&A, 523, A25

Clark, P. C., Glover, S. C. O., Ragan, S. E., Shetty, R., & Klessen, R. S. 2013, ApJL, 768, L34
Dubey, A., Fisher, R., Graziani, C., et al. 2008, Numerical Modeling of Space Plasma Flows, 385, 145
Dullemond, C. P. 2012, Astrophysics Source Code Library, ascl:1202.015
Evans, N. J., II 1999, Annu. Rev. Astron. Astrophy, 37, 311
Fryxell, B., Olson, K., Ricker, P., et al. 2000, ApJS, 131, 273
Goldsmith, P. F., & Li, D. 2005, ApJ, 622, 938
Hogerheijde, M. R., & van der Tak, F. F. S. 2000, A&A, 362, 697
Hopkins, P. F. 2015, MNRAS, 450, 53
Hopkins, P. F., & Raives, M. J. 2016, MNRAS, 455, 51
Keto, E. R. 1990, ApJ, 355, 190
Keto, E., Rybicki, G. B., Bergin, E. A., & Plume, R. 2004, ApJ, 613, 355
Krumholz, M. R., Klein, R. I., McKee, C. F., & Bolstad, J. 2007, ApJ, 667, 626
Kylafis, N. D. 1983, ApJ, 267, 137
Mihalas, D. 1978, San Francisco, W. H. Freeman and Co., 1978. 650 p.,
Mocz, P., Vogelsberger, M., Sijacki, D., Pakmor, R., & Hernquist, L. 2014a, MNRAS, 437, 397
Mocz, P., Vogelsberger, M., & Hernquist, L. 2014b, MNRAS, 442, 43
Motoyama, K., Morata, O., Shang, H., Krasnopolsky, R., & Hasegawa, T. 2015, ApJ, 808, 46
Pollack, J. B., McKay, C. P., & Christofferson, B. M. 1985, Icarus, 64, 471
Preibisch, T., Ossenkopf, V., Yorke, H. W., & Henning, T. 1993, A&A, 279, 577
Schaal, K., Bauer, A., Chandrashekar, P., et al. 2015, MNRAS, 453, 4278
Schöier, F. L., van der Tak, F. F. S., van Dishoeck, E. F., & Black, J. H. 2005, A&A, 432, 369
Seifried, D., & Walch, S. 2016, MNRAS, 459, L11
Shirley, Y. L. 2015, PASP, 127, 299
Shu, F. H. 1977, ApJ, 214, 488
Tassis, K., Willacy, K., Yorke, H. W., & Turner, N. J. 2012a, ApJ, 753, 29
Tassis, K., Willacy, K., Yorke, H. W., & Turner, N. J. 2012b, ApJ, 754, 6
Tritsis, A., Tassis, K., & Willacy, K. 2016, MNRAS, 458, 789
Turk, M. J., Smith, B. D., Oishi, J. S., et al. 2011, ApJS, 192, 9
van der Tak, F. F. S., Black, J. H., Schöier, F. L., Jansen, D. J., & van Dishoeck, E. F. 2007, A&A, 468, 627
Walch, S., Girichidis, P., Naab, T., et al. 2015, MNRAS, 454, 238
Yorke, H. W. 1986, NATO Advanced Science Institutes (ASI) Series C, 188, 141

Chapter 7

Concluding remarks

The recent observations from Herschel space observatory have reshaped our knowledge about the morphology of molecular clouds. Furthemore, observations of the magnetic field from Planck and HAWC+ have provided and will continue to provide new insights about the role of the magnetic field in their evolution. A successful theory of star formation should not only to be able to explain this vast amount of new observational data but also provide new predictions.

Here, we have developed the theoretical framework behind the formation of elongated structures seen in the low-density parts of molecular clouds. We have found that they are created due to compressible fast magnetosonic waves. Our theory has not only been able to successfully explain the observed properties of these structures but has also provided new predictions to be tested observationally. We have tested one such prediction, namely that in the presence of boundaries these waves can be trapped, thus resulting in normal modes. We have analysed existing observations of an isolated interstellar cloud and we have indeed found normal modes, a result that has allowed us to reconstruct its 3D structure. Another a prediction that can be tested with future interferometric observations with ALMA is the excitation of sausage MHD waves which can be detected through velocity variations along the long axis of these elongations. Finally, our theory can provides the means to study the spectrum of Alfvén waves in the Galaxy.

Furthermore, we have developed a method to probe the 3-dimensional shape of prestellar cores on an object-to-object basis. The 3D shape of cores encodes important information regarding the physical processes that dominate the formation of stars while different theories predict different shapes. Thus, we think that this method can be proven an important tool in the effort of distinguishing between opposing star formation theories. In future work we plan to extend our dynamical models of collapsing cores and post-process our numerical simulations with the line radiative transfer code we developed. Then, comparison of observed and synthetic molecular column density maps and spectra can aid to permanently settle the long-debated subject of the shape of prestellar cores.

Our results of the 3-dimensional structure of clouds in all physical scales are further strong indications that their evolution is magnetic dominated (Mouschovias & Ciolek 1999).

References

[1] Aikawa, Y., Ohashi, N., & Herbst, E. 2003, The Astrophysical Journal, 593, 906

[2] Alves, J., Lombardi, M., & Lada, C. J. 2007, Astronomy & Astrophysics, 462, L17

[3] Alves de Oliveira, C., Schneider, N., Merín, B., et al. 2014, Astronomy & Astrophysics, 568, A98

[4] Andersson, B.-G., & Wannier, P. G. 1993, The Astrophysical Journal, 402, 585

[5] André, P., Men'shchikov, A., Bontemps, S., et al. 2010, Astronomy & Astrophysics, 518, L102

[6] Arons, J., & Max, C. E. 1975, The Astrophysical Journal Letters, 196, L77

[7] Babcock, H. W., & Cowling, T. G. 1953, Monthly Notices of the Royal Astronomical Society, 113, 357

[8] Bailey, N. D., & Basu, S. 2013, The Astrophysical Journal, 766, 27

[9] Basu, S., & Mouschovias, T. C. 1994, The Astrophysical Journal, 432, 720

[10] Basu, S., & Ciolek, G. E. 2004, The Astrophysical Journal Letters, 607, L39

[11] Boulanger, F., Bronfman, L., Dame, T. M., & Thaddeus, P. 1998, Astronomy & Astrophysics, 332, 273

[12] Bronfman, L., Casassus, S., May, J., & Nyman, L.-Å. 2000, Astronomy & Astrophysics, 358, 521

[13] Caselli, P., Walmsley, C. M., Terzieva, R., & Herbst, E. 1998, The Astrophysical Journal, 499, 234

[14] Chapman, N. L., Davidson, J. A., Goldsmith, P. F., et al. 2013, The Astrophysical Journal, 770, 151

[15] Chen, X., Launhardt, R., & Henning, T. 2007, The Astrophysical Journal, 669, 1058

[16] Ciolek, G. E., & Mouschovias, T. C. 1993, The Astrophysical Journal, 418, 774

[17] Ciolek, G. E., & Basu, S. 2006, The Astrophysical Journal, 652, 442

[18] Cox, N. L. J., Arzoumanian, D., André, P., et al. 2016, Astronomy & Astrophysics, 590, A110

[19] Crutcher, R. M., Wandelt, B., Heiles, C., Falgarone, E., & Troland, T. H. 2010, The Astrophysical Journal, 725, 466

[20] Draine, B. T. 2011, Physics of the Interstellar and Intergalactic Medium by Bruce T. Draine. Princeton University Press, 2011. ISBN: 978-0-691-12214-4

[21] Gao, Y., & Solomon, P. M. 2004, The Astrophysical Journal, 606, 271

[22] Goicoechea, J. R., Pety, J., Gerin, M., Hily-Blant, P., & Le Bourlot, J. 2009, Astronomy & Astrophysics, 498, 771

[23] Goldsmith, P. F., & Arquilla, R. 1985, Protostars and Planets II, 137

[24] Goldsmith, P. F., Heyer, M., Narayanan, G., et al. 2008, The Astrophysical Journal, 680, 428-445

[25] Goodman, A. A., Benson, P. J., Fuller, G. A., & Myers, P. C. 1993, The Astrophysical Journal, 406, 528

[26] Goodman, A. A., Barranco, J. A., Wilner, D. J., & Heyer, M. H. 1998, Astrophysical Letters and Communications, 37, 109

[27] Hennemann, M., Motte, F., Schneider, N., et al. 2012, Astronomy & Astrophysics, 543, L3

[28] Heyer, M., Goldsmith, P. F., Yıldız, U. A., et al. 2016, Monthly Notices of the Royal Astronomical Society, 461, 3918

[29] Johnstone, D., Wilson, C. D., Moriarty-Schieven, G., et al. 2000, The Astrophysical Journal, 545, 327

[30] Juvela, M., Ristorcelli, I., Pagani, L., et al. 2012, Astronomy & Astrophysics, 541, A12

[31] Koch, P. M., Tang, Y. W., Ho, P. T. P., et al. 2015, EAS Publications Series, 75, 159

[32] Könyves, V., André, P., Men'shchikov, A., et al. 2015, Astronomy & Astrophysics, 584, A91

[33] Krumholz, M. R., & Tan, J. C. 2007, The Astrophysical Journal, 654, 304

[34] Krumholz, M. R. 2014, Physics Reports, 539, 49

[35] Kunz, M. W., & Mouschovias, T. C. 2009, Monthly Notices of the Royal Astronomical Society, 399, L94

[36] Li, D., & Goldsmith, P. F. 2012, The Astrophysical Journal, 756, 12

[37] Li, H.-b., Fang, M., Henning, T., & Kainulainen, J. 2013, Monthly Notices of the Royal Astronomical Society, 436, 3707

[38] Malinen, J., Montier, L., Montillaud, J., et al. 2016, Monthly Notices of the Royal Astronomical Society, 460, 1934

[39] McKee, C. F., & Williams, J. P. 1997, The Astrophysical Journal, 476, 144

[40] Mellon, R. R., & Li, Z.-Y. 2008, The Astrophysical Journal, 681, 1356-1376

[41] Men'shchikov, A., André, P., Didelon, P., et al. 2010, Astronomy & Astrophysics, 518, L103

[42] Miville-Deschênes, M.-A., Martin, P. G., Abergel, A., et al. 2010, Astronomy & Astrophysics, 518, L104

[43] Mooney, T. J., & Solomon, P. M. 1988, The Astrophysical Journal Letters, 334, L51

[44] Motte, F., Andre, P., & Neri, R. 1998, Astronomy & Astrophysics, 336, 150

[45] Mouschovias, T. C. 1975, Ph.D. Thesis,

[46] Mouschovias, T. C., & Spitzer, L., Jr. 1976, The Astrophysical Journal, 210, 326

[47] Mouschovias, T. C., & Paleologou, E. V. 1979, The Astrophysical Journal, 230, 204

[48] Mouschovias, T. C., & Paleologou, E. V. 1980, The Astrophysical Journal, 237, 877

[49] Mouschovias, T. C. 1987, NATO ASIC Proc. 210: Physical Processes in Interstellar Clouds, 453

[50] Mouschovias, T. C. 1991, The Astrophysical Journal, 373, 169

[51] Mouschovias, T. C., & Ciolek, G. E. 1999, NATO Advanced Science Institutes (ASI) Series C, 540, 305

[52] Murray, N., & Rahman, M. 2010, The Astrophysical Journal, 709, 424

[53] Myers, P. C. 2009, The Astrophysical Journal, 700, 1609

[54] Myers, P. C. 2017, The Astrophysical Journal, 838, 10

[55] Nutter, D., & Ward-Thompson, D. 2007, Monthly Notices of the Royal Astronomical Society, 374, 1413

[56] Ostriker, E. C., Stone, J. M., & Gammie, C. F. 2001, The Astrophysical Journal, 546, 980

[57] Padoan, P., Juvela, M., Goodman, A. A., & Nordlund, Å. 2001, The Astrophysical Journal, 553, 227

[58] Palmeirim, P., André, P., Kirk, J., et al. 2013, Astronomy & Astrophysics, 550, A38

[59] Panopoulou, G. V., Psaradaki, I., & Tassis, K. 2016, Monthly Notices of the Royal Astronomical Society, 462, 1517

[60] Pinto, R. F., Brun, A. S., Jouve, L., & Grappin, R. 2011, The Astrophysical Journal, 737, 72

[61] Planck Collaboration, Aghanim, N., Alves, M. I. R., et al. 2016a, Astronomy & Astrophysics, 596, A105

[62] Planck Collaboration, Adam, R., Ade, P. A. R., et al. 2016b, Astronomy & Astrophysics, 586, A135

[63] Planck Collaboration, Ade, P. A. R., Aghanim, N., et al. 2016c, Astronomy & Astrophysics, 586, A138

[64] Sadavoy, S. I., Di Francesco, J., Bontemps, S., et al. 2010, The Astrophysical Journal, 710, 1247

[65] Salpeter, E. E. 1955, The Astrophysical Journal, 121, 161

[66] Soler, J. D., & Hennebelle, P. 2017, arXiv:1705.00477

[67] Spitzer, L., Jr. 1968, Nebulae and Interstellar Matter, 1

[68] Steinacker, J., Bacmann, A., Henning, T., Klessen, R., & Stickel, M. 2005, Astronomy & Astrophysics, 434, 167

[69] Tassis, K., & Mouschovias, T. C. 2007, The Astrophysical Journal, 660, 370

[70] Tassis, K., Willacy, K., Yorke, H. W., & Turner, N. J. 2012, The Astrophysical Journal, 754, 6

[71] Testi, L., & Sargent, A. I. 1998, The Astrophysical Journal Letters, 508, L91

[72] van der Werf, P. P., & Goss, W. M. 1989, Astronomy & Astrophysics, 224, 209

[73] van Dishoeck, E. F., & Blake, G. A. 1998, Annual Review of Astron and Astrophys, 36, 317

[74] Wade, G. A., Maíz Apellániz, J., Martins, F., et al. 2012, Monthly Notices of the Royal Astronomical Society, 425, 1278

[75] Wannier, P. G., Lichten, S. M., & Morris, M. 1983, The Astrophysical Journal, 268, 727

[76] Woltjer, L. 1967, Radio Astronomy and the Galactic System, 31, 479